

**Some pages of this thesis may have been removed for copyright restrictions.**

If you have discovered material in Aston Research Explorer which is unlawful e.g. breaches copyright, (either yours or that of a third party) or any other law, including but not limited to those relating to patent, trademark, confidentiality, data protection, obscenity, defamation, libel, then please read our [Takedown policy](#) and contact the service immediately (openaccess@aston.ac.uk)

# **New Synchronous Machine Rotor Design for Easy Insertion of Excitation Coils Based on Surrogate Optimisation**

Ph.D. Thesis

Nan Yang

Doctor of Philosophy

Aston University

December 2017

©Nan Yang, 2017

Nan Yang asserts his moral right to be identified as the author of this thesis

This copy of the thesis has been supplied on condition that anyone who consults it is understood to recognize that its copyright belongs to its author and that no quotation from the thesis and no information derived from it may be published without appropriate permission or acknowledgement.

# Aston University

## New Synchronous Machine Rotor Design for Easy Insertion of Excitation Coils Based on Surrogate Optimisation

Nan Yang, Doctor of Philosophy, 2017

### **Thesis Summary**

The thesis reviews the development of traditional synchronous machine design and point out one problem with the manufacture of wound rotor synchronous machines. Install and repair process of the rotor windings can be considered labor-costly and time-consuming in synchronous machine design. The conclusion indicates a new winding method would be helpful for not only the new machines but also for rewound machines.

A new rotor design for the easy insertion and repair of the rotor windings is then introduced. This new asymmetrical rotor shows good potentials for reducing the maintenance and repair costs of synchronous machines, making it suitable for manufacturers within the mass production markets such as gen-sets, steam turbines, wind power generators. Simulation results from 2-D finite element analysis and experimental results from testing a 27.5 kVA prototype machine have verified the performance of the new rotor. The results show that the asymmetrical machine's electromagnetic performance is worse than traditional design and need to be optimised.

The shape of the rotor is then optimised based on novel surrogate method in order to achieve the lowest power loss under the maximum power output. This method combines surrogate optimisation with finite element method. It significantly reduces the time cost of the optimization process and can be applied with very complicated geometry design of the rotor. The performance of the new rotor is examined in 2-D finite element software and validated by experiments. After optimisation, the efficiency of the new rotor can reach the same level of the traditional rotor in electromagnetic performance in addition to its easy insertion and repair feature.

# Acknowledgement

First and foremost, I would like to present my sincerest gratitude to my principal supervisor, Prof. Wenping Cao for his guidance and support to my work. His critical thinking and academic view in the field of electrical machine design inspires me to pursue my own PhD career. His patience and confidence encourage me to go through my entire PhD career. Thank you for your support.

Particular thanks go to my secondary supervisor Dr Zhengyu Lin for his kind encouragement and suggestions to my PhD project.

The work would not have been possible without technical support and research idea from Prof. Xueguan Song, Dr Zheng Tan and Dr Zheng Liu. I would also like to thank Prof. Guofeng Li, and Prof. John Morrow who gave me much help and advice in my experiment of machines.

I would like to acknowledge Alalibo, Belema, Bukhari, Syed Abid Ali Shah for your kind support to my academic writing. Many friends and colleagues made my life in power group enjoyable and motivated, these friends, to name but a few are Dr Zhengzhao He, Guan hao Du, Ning Xin, Fulong Li, Changle Wang, and Shubo Hu. Special gratitude goes to my friends; Dr Zhile Yang, Dr Bowen Zhou Dr Cheng Zhang, who have worked in the EPIC group at Queen's University Belfast.

Finally, I could never have completed a doctorate without the support of my parents, Yuhong Yang and Ping Wang. I won't be in this position without your encouragement and support.

# Contents

Acknowledgement .....	3
Contents .....	4
List of Figures .....	8
List of Symbols .....	13
List of Publications .....	15
Chapter 1 Introduction .....	16
1.1 Background .....	16
1.2 Motivation and objectives .....	19
1.3 Methodology .....	20
1.4 Thesis Overview .....	20
1.5 Contribution to knowledge.....	21
Chapter 2 Synchronous machines.....	23
2.1 Development of synchronous machines .....	23
2.1.1 Introduction.....	23
2.1.2 Development of synchronous machines.....	24
2.2 Overview and topology of synchronous machines .....	25
2.2.1 Introduction.....	25
2.2.2 Types of synchronous machines .....	26

2.2.3 Analytical design of the synchronous machine.....	31
2.2.4 Modern analysis of synchronous machine .....	40
2.2.5 Maintenance of synchronous machine .....	56
2.2.6 Stator vs Rotor winding .....	58
Chapter 3 Asymmetrical rotor design .....	61
3.1 Aims and objectives .....	61
3.2 Comparison of two proposed rotors.....	62
3.3. Experimental tests and analysis of results.....	71
3.4 Summary .....	78
Chapter 4 Machine design investigation.....	79
4.1 No-load operation .....	79
4.2 Saliency calculation .....	83
4.3 Full-load operation.....	84
4.4 Stator design investigation.....	85
4.5 High-order harmonic reduction.....	86
4.6 Simplified analytical analysis of asymmetrical rotor.....	90
Chapter 5 Surrogate optimisation .....	93
5.1 Introduction.....	93
5.2 Surrogate modelling.....	95

5.2.1 Design of experiment .....	97
5.2.2 Construction of surrogate models .....	101
5.3 Surrogate optimisation .....	105
5.4 Heuristic search method.....	107
5.4.1 PSO .....	107
5.4.2 Genetic algorithm.....	109
5.5 Summary .....	110
Chapter 6 Simulation results and analysis .....	111
6.1 Aims and objectives .....	111
6.2 Preliminary test on two rotors .....	112
6.3 4-D parameterization .....	127
Chapter 7 Validation of experiment.....	134
7.1 Test equipment.....	134
7.2 Specifications of the original machine.....	134
7.3 Test procedure.....	134
7.3.1 Test limitations.....	135
7.3.2 Direct measurement .....	137
7.3.3 Indirect measurement.....	139
7.4 Harmonic analysis.....	147

7.5 Determination of efficiency .....	149
7.5.1 Determination from direct measurement (self-deceleration test).....	149
7.5.2 Determination from indirect measurement .....	150
7.6 Summary .....	154
Chapter 8 Conclusion.....	156
8.1 Conclusions.....	156
8.2 Future work.....	159
Reference .....	161
Appendices.....	171

# List of Figures

Fig. 1. Low-carbon electricity's share of energy generation in UK.....	17
Fig. 2. Renewable electricity generation [3].....	17
Fig. 3. Schematic of 10-MW HTS synchronous generator [10]. ....	27
Fig. 4. Structure of salient-rotor pole.....	28
Fig. 5. The topology of 4-pole cylindrical rotor for synchronous machines [12]. ....	29
Fig. 6. Rotor designs with magnet-based flux barriers [17].....	30
Fig. 7. Exploded view of the claw-pole machine [22]. ....	31
Fig. 8. Existing asymmetrical rotor designs.....	31
Fig. 9. Multi-turn coils. ....	35
Fig. 10. Existing stator slot designs. ....	36
Fig. 11. Optimisation flowchart [30].....	43
Fig. 12. Definition of a flux tube and the corresponding reluctance [34]. ....	43
Fig. 13. Passive 3-D reluctance element [35]. ....	44
Fig. 14. The topology of the traditional salient rotor for synchronous machines [39]....	45
Fig. 15. Flux path in rotor layer regions [40].....	46
Fig. 16. Geometry definition of stator slots [44].....	47
Fig. 17. B-H hysteresis curve of a ferromagnetic material [48].....	51
Fig. 18. Eddy current on pieces [50].....	52
Fig. 19. Loss table.....	52
Fig. 20. Brush exciter [55]. ....	55

Fig. 21. Brushless exciter [56].	55
Fig. 22. The arrangement of the stator winding (distributed).	58
Fig. 23. The arrangement of the rotor winding (concentric).	60
Fig. 24. A three-dimensional diagram of the proposed machine.	61
Fig. 25. Installation of the rotor coils.	62
Fig. 26. Flux distribution of the machines at no load. (a) Asymmetrical rotor. (b) Symmetrical rotor.	63
Fig. 27. No-load air-gap flux density. (a) Asymmetrical. (b) Symmetrical.	64
Fig. 28. FFT analysis of the no-load air-gap flux density.	65
Fig. 29. No-load EMF voltages.	65
Fig. 30. No-load characteristics.	66
Fig. 31. Flux distribution of the machine at full load.	67
Fig. 32. Induced phase voltages of the machines at full load.	68
Fig. 33. Pull-out torques.	69
Fig. 34. Phasor diagram	69
Fig. 35. Simulated low-slip test results.	70
Fig. 36. Photographs of the prototyped synchronous machine.	73
Fig. 37. Comparison of the constant speed-variable excitation test between the two machines.	73
Fig. 38. FEA and measured results of the output voltage.	74
Fig. 39. Comparison of constant excitation-variable speed test between the two machines.	75

Fig. 40. Comparison of the two machines during sustained three-phase short-circuit test. .....	75
Fig. 41. Comparison of the two machines at varying inductive loads. ....	76
Fig. 42. Comparison of the two machines at different resistive loads. ....	78
Fig. 43. Flux distribution of the 3 proposed rotor shapes. ....	80
Fig. 44. No-load air-gap flux density and FFT analysis.....	81
Fig. 45. No-load voltage comparison of three proposed machines.....	82
Fig. 46. No-load characteristic of the four machines. ....	83
Fig. 47. Low-slip test simulation results for machines. ....	84
Fig. 48. Comparison of the maximum torque between the three proposed machines. ...	85
Fig. 49. Waves of induced EMFs for different winding arrangements. ....	85
Fig. 50. Inverse cosine function pole shoe of a rotor. ....	87
Fig. 51. Centre-offset arc pole shoe. ....	87
Fig. 52. Effect of ratio on air-gap flux density. ....	88
Fig. 53. FFT analysis of air-gap flux density. ....	88
Fig. 54. The parametrisation of plan A. ....	90
Fig. 55. Different surrogate models may be constructed with the same data [97]. ....	95
Fig. 56. Predicted uncertain area using probability density function $\theta$ in the predicted function ( $f_p$ ) [98]. ....	96
Fig. 57. The procedure of the surrogate modelling method. ....	97
Fig. 58. Factorial designs for three design variables (n=3):.....	99
Fig. 59. The procedure of the surrogate modelling method [115]. ....	105

Fig. 60. The procedure of the PSO method [138].	109
Fig. 61. Optimisation plans.	112
Fig. 62. Problem definition A of design plan 1.	113
Fig. 63. FEA simulation: no-load flux distribution.	114
Fig. 64. Three-phase induced voltages.	114
Fig. 65. FEA full-load flux distribution.	115
Fig. 66. Estimated torque production.	115
Fig. 67. Surrogate models: (a) torque distribution and (b) loss distribution.	116
Fig. 68. Twenty sample surrogate models: (a) torque distribution and (b) loss distribution.	118
Fig. 69. Three-phase induced voltages of 2/3 short-pitch rotor.	119
Fig. 70. Flux distribution and harmonic analysis.	119
Fig. 71. Surrogate models of short-pitch configuration:	120
Fig. 72. Asymmetrical rotor designs. (a) Original design. (b) Constraints.	121
Fig. 73. Definition of input parameters.	121
Fig. 74. Harmonic spectrum for evaluating power quality.	122
Fig. 75. Efficiency contour for D-R combination.	123
Fig. 76. Harmonic contour for D-R combination.	123
Fig. 77. Efficiency distribution for the D-R combination.	124
Fig. 78. Seventeenth harmonic distribution for D-R combination.	125
Fig. 79. Comparison of the no-load EMF voltages.	125
Fig. 80. Comparison of FFT results.	126

Fig. 81. No-load characteristics. ....	126
Fig. 82. Comparison of load tests. ....	127
Fig. 83. Problem definition B of design plan 1. ....	128
Fig. 84. Problem definition C of design plan 2. ....	129
Fig. 85. Comparison of no-load flux densities of two plans. ....	129
Fig. 86. Comparison of induced EMF of two plans. ....	130
Fig. 87. Comparison of no-load characteristics. ....	131
Fig. 88. Comparison of induced torque angle of two plans. ....	132
Fig. 89. Torque signal. ....	138
Fig. 90. Torque and speed signals measured by an oscilloscope. ....	139
Fig. 91. Comparison of the results of the constant speed-variable excitation test. ....	140
Fig. 92. Simulated low-slip test results (FEA results).....	146
Fig. 93. Low-slip test results (experimental results). ....	147
Fig. 94. FFT analysis of symmetrical rotor no-load voltage waveform calculated by power analyser. ....	148
Fig. 95. FFT analysis of asymmetrical rotor no-load voltage waveform calculated by power analyser. ....	148
Fig. 96. Loss-voltage curve.....	151
Fig. 97. Photographs of the Cummins PI-144F.....	174

# List of Symbols

Symbol	Name	Explanation
$P_T$	Total losses	Difference between the input power and the output power
$P_k$	Constant losses	Sum of the iron losses and the friction and windage losses
$P_{fe}$	Iron losses	Losses in active iron and additional no-load losses in other metal parts
$P_{fw}$	Friction and windage losses	Losses due to friction and total losses due to aerodynamic friction in all parts of the machine
$P_e$	Excitation circuit losses	Sum of the excitation winding losses, the exciter losses and, for synchronous machines, electrical brush loss
$P_f$	Excitation winding losses	The excitation (field) winding losses are equal to the product of the exciting current $I_e$ and the excitation voltage $U_e$
$P_{Ed}$	Exciter losses	<p>Brushless exciter:</p> $P_{Ed} = P_{shaft} - P_{fw} + P_{1E} - P_{converter}$ <p><math>P_{shaft}</math> : power absorbed by the exciter at its shaft</p> <p><math>P_{converter}</math> : the useful power that the exciter provides at the rotating power converter terminals</p> <p>Static excitation system:</p> $P_{Ed} = P_{ps} + P_{ea} - P_f - P_{1E}$ <p><math>P_{ps}</math> : the electrical power drawn from its power source</p> <p><math>P_{ea}</math> : power absorbed by separate auxiliary supplies</p>

$P_{1E}$	Separately supplied excitation power	Brushless exciter: The exciter excitation power. It covers a part of the exciter losses $P_{Ed}$ while a larger part of $P_e$ is supplied via the shaft;
		Static excitation system: equal to the excitation circuit losses,
$P_b$	Brush losses	Electrical brush loss (including contact loss) of separately excited synchronous machines
$P_L$	Load losses	Winding losses in the armature windings of synchronous machines
$P_{LL}$	Additional load losses	Losses produced by the load current in active iron and other metal parts other than conductors; eddy current losses in winding conductors caused by load current-dependent flux pulsations and additional brush losses caused by commutation
$P_{sc}$	Short-circuit losses	Current-dependent losses in a synchronous machine when the armature winding is short-circuited
$\theta_c$	Primary coolant inlet temperature	
$\theta_w$	Winding temperature	

# List of Publications

The following peer-reviewed conference and journal papers have been published based on this research:

- 1) N. Yang, W. Cao, Z. Liu, J. Morrow, “Design of an asymmetrical rotor for easy assembly and repair of field windings in synchronous machines,” *The Journal of Engineering*, pp. 1-6, 2017.
- 2) N. Yang, W. Cao, Z. Lin, G. Li, X.Song, “Design of an asymmetrical rotor for easy assembly and repair of field windings in synchronous machines,” *IEEE Industrial electronics* , pp. 1-6, 2017 (submitted).
- 3) N. Yang, W. Cao, Z. Liu, Z. Tan, Y. Zhang, S. Yu, J. Morrow, “Novel asymmetrical rotor design for easy assembly and repair of rotor windings in synchronous generators,” *IEEE Magnetics Conference (INTERMAG)*, Beijing, pp. 1-1, 2015.
- 4) N. Yang, W. Cao and Y. Hu, “New machine design for easy insertion of excitation coils in synchronous generators,” *2015 IEEE International Electric Machines & Drives Conference (IEMDC)*, Coeur d'Alene, ID, 2015, pp. 756-762.
- 5) N. Yang, W. Cao, Z. Tan, X. Song, T. Littler and J. Morrow, “Asymmetrical rotor design for a synchronous machine based on surrogate optimisation algorithm,” *8th IET International Conference on Power Electronics, Machines and Drives* , Glasgow, pp. 1-6, 2016.

# Chapter 1 Introduction

---

This thesis focuses on the application of a new optimisation method for a new rotor design for easy assembly and repair of rotor winding in a wound-rotor synchronous machine. The aim of the optimisation aims to reduce loss caused by its unique asymmetrical rotor shape and improve its output power. This chapter provides a brief overview of the research background and objectives while discussing the methodologies required for this project.

## 1.1 Background

Rapid population growth and industrialisation in the 21<sup>st</sup> century have generated a rapid boost in electricity demand and corresponding CO<sub>2</sub> emissions [1]. Since the signing of the Paris Agreement in 2016, a set of CO<sub>2</sub> reduction policies has been proposed for environmental protection around the world. As a result, global CO<sub>2</sub> emission growth has plateaued over the past 3 years. In developed countries such as the UK, CO<sub>2</sub> emissions have fallen to their lowest level since the 19<sup>th</sup> century [2].

An analysis of the success in reducing CO<sub>2</sub> emissions in the UK suggests that a revolution in energy structure and the development of microgeneration are the major reasons.

With respect to energy structure, the share of low-carbon electricity generation has increased significantly, as shown in Fig. 1. The detailed energy analysis shown in Fig. 2 further indicates the following changes in energy structure.

Coal, which was one of the major energy sources in 2014, has decreased to represent only approximately 2% of total energy consumption. Coal's share of energy generation has

been replaced by gas and renewable energy. More focused research on renewable energy shows that wind is still the largest renewable energy source. This increase reflects a growing requirement for large-capacity onshore wind and solar energy. On the other hand, bioenergy's share of energy has remained stable. If onshore (27%) and offshore wind power (18%) are calculated separately, these two sources constitute the largest share of energy generation (45%).



Fig. 1. Low-carbon electricity's share of energy generation in UK.



Fig. 2. Renewable electricity generation [3].

Another reason for the UK's low-carbon economy is the generalisation of microgeneration systems. Renewable energy is widely accepted by private users as a home-supply option rather than as a backup source to the grid. This home-based stand-alone electrical system is usually small in scale, and energy is consumed where it is generated. Therefore, such systems are more efficient, as transmission and distribution losses are negligible. Some

commercially available microgeneration systems include the following.

Photovoltaics use solar energy to generate electricity using photovoltaic cells; that electricity is then transferred to an electrical system through a power converter. Therefore, no CO<sub>2</sub> emissions are generated in this process. Given the price of solar cells and their large physical footprint, the cost of domestic solar power systems is quite considerable. To date, the promotion of household solar power systems has relied heavily on government subsidies.

Biomass refers to the use of burning organic material to generate electricity or heat. Many types of fuel can be used for small-scale household applications, such as wood and recycled waste. This system is not ideal for urban users, as the transfer and storage of biomass fuel are quite costly. The use of an electrical machine is inevitable in this process for the conversion of thermal energy to electricity.

Wind and small hydro systems are relatively less commonly applied in the household environment. Similar to large power plants, these small systems also require the conversion of wind turbine/hydro-turbine energy. Therefore, these systems rely heavily on natural energy sources and can be applied only in certain locations.

To conclude, reducing CO<sub>2</sub> emissions relies heavily on the promotion of renewable energy and the corresponding energy generators. Currently, however, generators are more often used in stand-alone systems. As they are grid-free, these systems should be able to operate under stable operating conditions and at small-medium power ratings for a considerably long time. Therefore, the installation and maintenance of generators play a more important role than their power rating and efficiency.

## **1.2 Motivation and objectives**

Wound-rotor generators have been widely used for many years. These generators are the primary source of electricity in the world. However, because it is necessary to install and repair rotor windings, the use of wound-rotor generators is considered expensive in terms of labour and time.

This project focuses on the rotor design and optimisation of synchronous machines to achieve maximum power output with minimum power loss. The objectives of the research are as follows:

- (1) To design a salient rotor geometry for easy insertion and repair of the rotor windings to simplify the manufacturing process
- (2) To provide a detailed analysis of the influence of the rotor structure on machine performance
- (3) To apply a new method for optimising synchronous machine performance and compare the results of the new method with those of the traditional finite element method
- (4) To validate the results of a simulation using a laboratory test bench

Achieving these objectives requires improvements in the efficiency of a synchronous machine with a new rotor geometry. A suitable optimisation approach and corresponding algorithm are established and applied. The optimisation results are then modified based on the results obtained for a commercially available synchronous machine and compared

to the traditional rotor of the original design.

## 1.3 Methodology

The thesis focuses on the repair and maintenance of rotor windings in a wound-rotor synchronous machine to achieve maximum power output and minimum loss. The following methodologies are used to simulate the machine and validate the test results:

- The geometry of the salient rotor shape is designed using *Autodesk AutoCAD*.
- The performance of the synchronous machine is analysed using *Infolytica MagNet* (2-dimensional finite element software/2DFE software).
- The design of the new rotor is optimised by a surrogate optimisation algorithm involving the evaluation of different geometry parameters. The corresponding data are collected and processed in *MATLAB*.
- The original and optimised rotor is manufactured and tested on the same test bench to validate the results of the optimisation

## 1.4 Thesis Overview

This thesis presents a new rotor design for the easy insertion and removal of rotor windings.

Five chapters are included in the thesis, and the thesis can be summarised follows:

Chapter 2 reviews the development of synchronous machines, covering topology, traditional design methods, modern design methods, and the maintenance and repair process of synchronous machines (particularly on rotor windings).

Chapter 3 analyses the performance of a new asymmetrical rotor design for easy assembly and repair of field windings in synchronous machines. A new rotor geometry is adopted

to simplify the manufacture and maintenance of installed rotor windings. The asymmetrical rotor design is simulated by 2-D finite element analysis (FEA) and verified by experimental tests on a 27.5 kVA prototype machine.

Chapter 4 proposes a new method of optimisation using a surrogate model of a wound-rotor synchronous machine with the assistance of finite element results. An appropriate search algorithm is chosen for the optimisation as well.

Chapter 5 validates the results of the simulation and compares the performance of the optimised rotor with that of a traditional rotor.

Chapter 6 presents the main conclusions of the study, suggests future work and highlight the main contribution to knowledge.

## **1.5 Contribution to knowledge**

This work introduces a new asymmetrical rotor geometry of wound-rotor synchronous machines to simplify the installation and uninstallation processes of rotor windings. The electromagnetic performance of this new rotor is analysed by 2DFE software and confirmed by experimental tests. The critical curvature of the rotor geometry is analysed by varying changing parameters and is optimised through a new surrogate optimisation method.

This work demonstrates that the new rotor design can improves the installation process of the rotor coils by not separating the rotor poles. Therefore, the mechanical integrity of the rotor pole is maintained; and the ageing problem is solved. The new design also improves the maintenance cost of the power system and increases the cost efficiency.

This work also provides a new optimisation process in the rotor design of wound-rotor synchronous machines. The combination of surrogate optimisation and finite element methods can reduce the time cost of the traditional search optimisation method and address the design of the rotor's complex geometry.

# Chapter 2 Synchronous machines

---

## 2.1 Development of synchronous machines

This chapter gives a brief literature review on the development of synchronous machines, including their topology, design, analysis method and maintenance process.

### 2.1.1 Introduction

Synchronous machines are traditional electrical machines whose history dates back to the 19<sup>th</sup> century. These machines are still considered the most common type of machine for electric power generation although their ubiquity has been severely challenged in recent decades. The power rating of machines became larger over the last century due to the rapid growth of power requirements. Until recent years, the power rating of the largest synchronous machine, which was built and operated at a nuclear power plant in Finland, was 2000 MW per unit [4].

The basic operating principle of a synchronous machine is relatively simple: If a stationary magnetic field is fixed to a rotating shaft, the corresponding rotating magnetic field will induce an electromagnetic force on the stator windings. The word “synchronous” indicates that the frequency of the induced voltage is matched for the rotor.

Synchronous machines can be divided into permanent magnet synchronous machines (PMSMs) and wound-rotor synchronous machines (WRSMs) based on the source of their magnetic field. The magnetic field of the former is fixed by choice of magnetic materials (such as a neodymium magnet). The introduction of a permanent magnet provides very

high-power density. However, the magnetic field is fixed, and field weakening becomes a difficult technical issue.

Wound-rotor synchronous machines (WRSMs), on the other hand, use an electromagnet instead of a natural magnet. The magnetic field can thus be varied by changing the DC current of the excitation source. However, the efficiency of WRSMs is limited by the low power density of the electromagnet if the power rating of the machine is less than 10MW.

### **2.1.2 Development of synchronous machines**

A stationary field pole surrounded by a rotating armature type of generator (known as an external-pole generator) was first introduced in the 1800s. The reverse type (i.e., internal-pole generator) was soon recognized as a more suitable topology due to the invention of the three-phase alternative current system [5]. Haselwander built the first stationary, ring-shaped, three-phase salient pole synchronous generator in 1887, which produced approximately 2.8 KW of power at 960 rpm, corresponding to a frequency of 32 Hz.

The power rating of early synchronous machines was limited by the insulation materials and cooling systems used [6]. Modern high-solids and solvent-free resin insulation technology was not developed until the 1970 energy crisis. Similar advancements in cooling systems were made as well. Air cooling dominated the cooling system of synchronous machines until 1937 when the first hydrogen-cooled machines went into service [7]. Various direct and indirect cooling systems were invented only over the past 50 years, such as gas-cooling, oil-cooling, and water-cooling systems.

The limitations caused by the insulation technology were significantly improved during

the 1990s. A new Class F insulation system developed by Westinghouse Electric Company met most functional requirements. The system was then verified by industrial trials and has been used in several turbine generators since 1991[7]. Other insulation technologies developed for special operating conditions have also been introduced. One example is the rotor winding insulation system developed by Nanjing Turbine & Electric Machinery Group Co, which consists of Nomex 411 paper impregnated with adhesive varnish. This technology is specially designed for humid absorption and can be cleaned easily [8].

Another technology milestone in synchronous technology lies in synchronous machine analysis. Finite element software was initially introduced to design and analyse the synchronous machines in an aerospace project carried out at Parsons Lab [9]. This computer-assisted FE method, involving computational fluid dynamics, electromagnetic and thermal finite element analysis, became very popular in the following decades.

## **2.2 Overview and topology of synchronous machines**

### **2.2.1 Introduction**

In general, any electromechanical energy converter that transfers energy by synchronising induction can be classified as a synchronous machine. However, PMSMs are more likely to be treated as individual devices because their magnetic fields are constant. In the following part of this thesis, the discussion of synchronous machines is limited to electro-excited synchronous machines.

Synchronous machines usually operate in parallel in power plant that transfers energy to consumers. Such machines can be categorised into two types based on their operational

speed.

High-speed synchronous machines are usually of medium size, with their prime mover driven by fossil or nuclear energy sources. Low-speed synchronous machines, on the other hand, are very large and driven slowly by hydro-turbines that employ water power for a generation. Certain low-power synchronous machines operate individually for stand-alone networks, usually as a backup source with diesel engines or gas turbines as the prime mover.

Synchronous machines can also sink power and operate as a synchronous motor. However, such machines usually operate as variable-power factor compensators for the grid instead of acting as a drive due to their relatively low power density compared with that of PMSMs. As a variable-power factor compensator, these machines can operate as capacitors or inductors depending on their excitation conditions.

### **2.2.2 Types of synchronous machines**

According to the arrangement of the field and armature windings, an electron-excited synchronous machine can be classified as a rotating-field or rotating-armature machine.

According to the shape of the field, a rotating-field synchronous machine can be further classified as a cylindrical rotor or salient rotor.

#### **A. Rotating-armature topology**

Rotating-armature synchronous machines place the field windings on the stator and armature windings on the rotor, as shown in Fig. 3. Therefore, the magnetic field is stationary, and energy must be transferred to the load via slip rings and brushes. This brush

system limits the power rating of this topology and creates an insulation problem. Such devices are mainly used in very low-power machines or used as exciters in high-power machines.

However, due to the application of super-conductivity and the requirement for a cryogenic refrigerator, certain applications are trying to incorporate the rotating-armature type of machine into wind turbines [10] [11]. A stationary field permits the cooling devices to operate at constant environment (no vibration). It makes the cooling process easier and allows for a larger number of poles. Results show that rotating-armature machines provide a significant improvement in electromagnetic performance but inevitably increase the mechanical complexity and friction losses due to the brushes.



Fig. 3. Schematic of 10-MW HTS synchronous generator [10].

## **B. Rotating-field topology**

In contrast to that of a rotating-armature machine, the magnetic field of a rotating-field machine is on the rotor. The armature windings are located on the stator. The field

windings are supplied by a slip-ring/brush system or brushless exciter. Rotating-field topology is the most common topology due to its ability to provide large amounts of power. There are two types of rotating-field synchronous machines: cylindrical-rotor and salient-rotor machines.

In Fig. 4, the salient-pole rotor has a salient-pole body outside the rotor yoke. Field windings are wrapped around the pole bodies and protected by a pole surface against centrifugal forces. This type of rotor usually has multiple poles; therefore, it can operate at low speed. However, salient-rotor machines are usually in small and medium power ratings for the following reasons:

- a) Extra windage losses due to the salient-pole structure and the corresponding noise; and
- b) Weak mechanical strength when operating at high speed.

The salient pole has an unequal air gap around its periphery. Therefore, the operating characteristic of this type of machine is significantly influenced by the design of the pole shape, as analysed in later chapters.

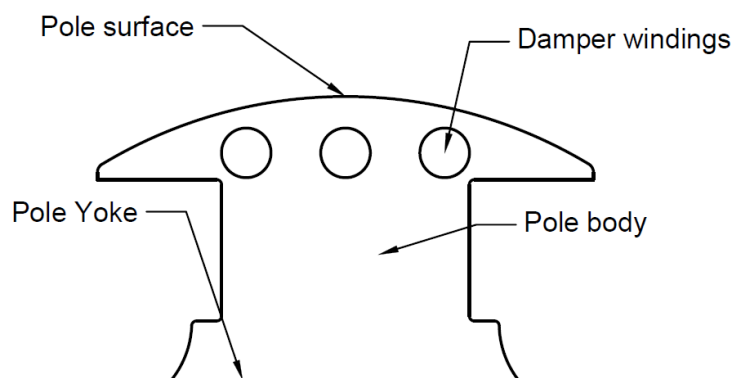


Fig. 4. Structure of salient-rotor pole

A cylindrical-rotor construction is widely used in high-speed applications, such as in steam turbines. The non-salient structure of this design provides solid physical support for

the excitation windings. Due to the large centrifugal forces caused by the high-speed operation, the diameter of the cylindrical rotor is constrained. Therefore, these rotors are the usually smaller in diameter and longer axial length when compared to salient rotors. A typical 4-pole cylindrical rotor is shown in Fig. 5 [12].

A cylindrical rotor is usually designed as a 2-pole or 4-pole machine. A major problem associated with multiple-pole cylindrical-rotor designs is the limited space available for stator slots [13,14]. Therefore, commercial multi-pole cylindrical rotors are rare. Two theoretical analyses of multi-pole cylindrical rotors were performed in [15,16]. The air-gap distance around the periphery of a cylindrical rotor is uniform, which is a unique feature in rotor designs, as discussed in a later section.

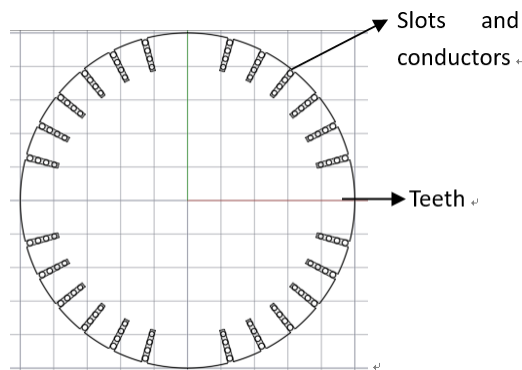


Fig. 5. The topology of 4-pole cylindrical rotor for synchronous machines [12].

Special types of rotors for synchronous machines are herein discussed. One interesting aspect of rotor design is the use of magnets and flux barriers in the rotor. Two examples are shown in Fig. 6.



Fig. 6. Rotor designs with magnet-based flux barriers [17].

(a) Design 1. (b) Design 2.

As the magnetic flux flow through the least reluctance path, the insertion of the magnet will guide the flux to follow its magnetized directions. On the contrary, flux barrier will stop the flux to follow its direction. Therefore, by changing the placement of magnet and flux barrier, this technology will change the electromagnetic performance of the machine. This technology can be applied to various types of machines, such as synchronous reluctance machines [17-19], wound-rotor synchronous machines [20], and stator wound-field synchronous machines [21]. However, adding the flux barriers and magnets increases the complexity and manufacturing cost of the rotor. Therefore, this technology is not widely adopted by industry.

Another interesting topology is the claw-pole alternators [22]. As shown in Fig. 7, the field coils can be clicked into position between the two rotor poles. This topology provides an interesting idea since the winding is separately designed and installed. However, this topology is quite complex electromagnetically, and the rotor is asymmetrical in the axial direction; thus, a 3-D FEA tool must be used to determine the device's saturation level and leakage flux. This type of machine features high design and manufacture costs.



Fig. 7. Exploded view of the claw-pole machine [22].

With respect to rotor-pole geometry, asymmetrical rotors have been reported in the literature [23]- [27]. These rotor designs are characterized by an unequal number of poles between the stator and rotor [25] or an unbalanced rotor slot geometry [26].

Two asymmetrical rotor geometries are shown in Fig. 8. Both designs use an asymmetrical rotor geometry designed for reluctance machines, which are not widely used in industry.

This thesis adopts an asymmetrical rotor design and modifies the shape of the rotor to simplify the assembly of the rotor winding.



(a)



(b)

Fig. 8. Existing asymmetrical rotor designs.

(a) Design 1 [24]. (b) Design 2 [27].

### 2.2.3 Analytical design of the synchronous machine

Traditional analytical design methods for synchronous machines are discussed in the

following subsections. A list of all symbols used in this section is shown in Table.23 in appendices.

## A. Dimensions and length

The gross dimensions of a synchronous machine are achieved based on its design objectives, such as power rating, power factor, and speed of rotation. A general equation is as follows:

$$\begin{aligned}
 S &= 3V_{ph} I_{ph} \times 10^{-3} \text{ KVA} \\
 &= 3(4.44 f \Phi N_{ph} K_w) I_{ph} \times 10^{-3} \text{ KVA} \\
 &= 3(4.44 \frac{pn_s}{2} \Phi N_{ph} K_w) I_{ph} \times 10^{-3} \text{ KVA}
 \end{aligned} \tag{1}$$

In this case, if the magnetic loading and electric loading are defined by

$$\begin{aligned}
 \text{Magnetic loading} &: B_{av} \pi DL / p \\
 \text{Electric loading} &: 3 I_{ph} 2 N_{ph} / \pi D
 \end{aligned} \tag{2}$$

the equation can be deduced as follows:

$$\begin{aligned}
 S &= 3(2.22 pn_s \frac{B_{av} \pi DL}{p} N_{ph} K_w) \frac{q \pi D}{2 N_{ph} \times 3} \times 10^{-3} \text{ KVA} \\
 &= 1.11 n_s B_{av} \pi^2 D^2 L K_w q \times 10^{-3} \text{ KVA} \\
 &= (1.11 B_{av} q K_w \times 10^{-3}) D^2 L n_s
 \end{aligned} \tag{3}$$

As indicated by this equation (3), the volume of the machine is directly influenced by the specific loading applied. Due to the limitations of the following factors, the magnetic loading is often restricted to 0.7-1.1 T:

- Iron loss: A high air-gap flux density leads to high saturation, which increases the iron loss and decreases efficiency.
- Insulation: A high air-gap flux density requires a high excitation level. This demand will increase the size of the machine due to the stronger requirement of

insulation materials.

- **Stability:** A low air-gap flux density requires a high number of turns under the same voltage. This will influence the leakage flux density, jeopardising its power rating as well as stability.

Similarly, electric loading is constrained to a specific range. However, the constraint depends on the insulating and conducting materials rather than a specific range of values, as observed for magnetic loading:

- **Copper loss:** High electric loading produces high copper loss and heat generation, which reduces thermal performance and the corresponding efficiency.
- **Voltage:** High electric loading requires more space for copper; reducing the amount of space for insulation causes problems with both thermal and electric insulation.
- **Stability:** An increase in electric loading produces a higher armature reaction, reducing the voltage regulation and the lower limit of steady-state stability, and a small amount of power is generated.

Therefore, both forms of loading can be considered to be constant, and the entire equation can be modified as follows:

$$S = C_0 D^2 L n_s \quad (4)$$

where D and L are determined based on the following general design rules:

For round poles,

$$L / \tau_p = L / \frac{\pi D}{p} = 0.6 \sim 0.7 \quad (5)$$

For rectangular poles,

$$L / \tau_p = L / \frac{\pi D}{p} = 0.8 \sim 3 \quad (6)$$

## **B. Air-gap distance**

The function of the air gap is to establish a mechanical separation between the stator and rotor. However, because air is not an ideal material for flux transfer, the length of the air gap should be minimal distance. However, an extremely small air-gap distance can reduce the stability, synchronous power, cooling, and magnetic force acting on the machine. A general principle for choosing the air-gap distance is expressed as follows in terms of the pole pitch:

For a salient-pole synchronous machine,  $L_g = (0.012 \text{ to } 0.016) * \text{pole pitch}$

For a cylindrical-pole synchronous machine,  $L_g = (0.02 \text{ to } 0.026) * \text{pole pitch}$

## **C. Stator design**

Stator design can be divided into two parts: stator winding design and stator slot design.

Stator winding design focuses on the arrangement of a high-conductivity coil (aluminium or copper) to achieve a low resistance in all coils. A major decision is whether to include a single- or double-layer design or a short-pitch or full-pitch design.

Stator slot design involves the following steps:

- Deciding the number of slots
- Determining the winding connection
- Designing the stator slot dimensions

### Number of slots

The number of slots is determined by a constant referred to as the slot per pole per phase.

A high value for this constant would lead to lower leakage reluctance, better cooling, and less tooth ripple. However, a high constant would also render the tooth structure mechanically weak, causing higher design costs and the high flux density in the teeth.

Therefore, a general principle for a machine is that the stator slot pitch should be at least 3.5 cm at low voltage, 5.5 cm at the medium voltage and 7.5 cm at high voltage, while the slot loading should be less than 1500 amps/slot

Thus, the slot per pole per phase should be 3 to 4 for a salient-pole synchronous machine and 7 to 9 for a cylindrical-pole synchronous machine.

### Connection of windings

Only two types of windings are applied in stator winding connections: single-turn bar coils and bar coils. Generally, multi-turn coils perform better in small- and medium-scale synchronous machines.

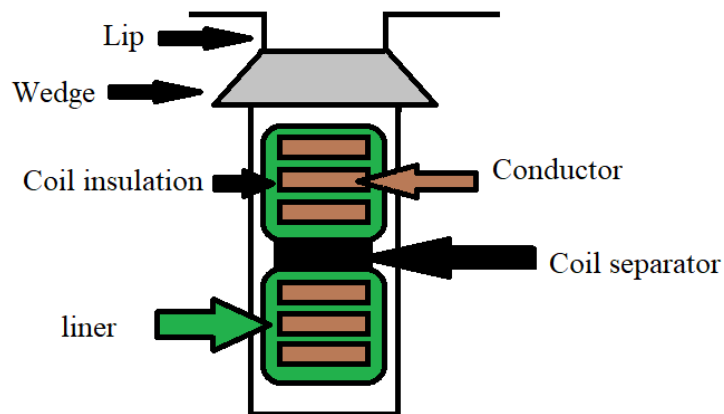


Fig. 9. Multi-turn coils.

Single-bar coils are only applied in large machines with a stator current greater than 1500

amps. A typical multi-turn coil with a double-layer connection in the stator slot is shown in Fig. 9.

Clearly, due to the use of a wedge and insulating material, not all spaces can be filled with conductors. The ratio of the conductor area to the total slot area is defined as the slot filling factor, which should be constrained to a reasonable value (0.4-0.6).

### Stator slot dimensions

In a traditional design, the slot dimensions are determined by checking the flux density of the stator lamination, ensuring that the value does not exceed 1.8 to 2 T. However, because the inner diameter of a salient-pole machine is usually large, and the flux density distribution is not always uniform along the depth of teeth, the flux density at the center of the teeth and the end of the teeth should be calculated according to the main flux and the corresponding geometrical length. Some common type of slot shapes includes a semi-closed slot, semi-open slot, and open-slot as shown in Fig.10. Semi-close slots are widely used for machines with small-medium power rating machines (<10KW). Open-slot is more frequently adopted in large alternators.

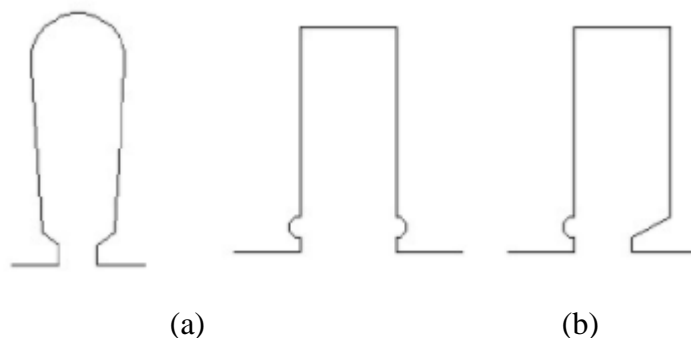


Fig. 10. Existing stator slot designs.  
(a) semi-close round-bottom. (b) semi-close flat-bottom slot. (c) open slot.

## D. Rotor design

The rotor pole is determined by 3 parameters: length, width and height.

The length of the rotor is usually designed to be 95-97% of the stator core length.

The width of the rotor is determined by the following equation:

$$w_p = \frac{A_p}{l_p} = \frac{\frac{\phi_p}{B_p}}{0.93 \sim 0.95 l_{core}} = \frac{1.1 \sim 1.15 \phi}{1.4 \sim 1.6 \text{ wb/m}} \quad (7)$$

where  $w_p$  is the width of the pole,  $l_p$  is the length of the pole,  $l_{core}$  is the length of the stator core,  $\Phi$  is the main flux, and  $\Phi_p$  is the flux in the pole body.

Because the surface area of the coil is used to dissipate heat, the height of the coil is determined by the permissible loss ratio. The heat loss generated by the field coil is calculated as follows:

$$P_{coil} = I_f^2 R_f = I_f^2 \times \zeta l_{mt} \times \frac{T_f}{a_f} = I_f^2 \times \zeta l_{mt} \times \frac{T_f^2}{s_f d_f h_f} \quad (8)$$

where  $P_{coil}$  is the heat generated by the field current,  $i_f$  is the field current,  $R_f$  is the resistance of the field windings,  $l_{mt}$  is the main length of the field,  $\zeta$  is the resistive conductivity of the winding,  $T_f$  is the number of turns in the field coils, and  $A_f$  is the area of the surface conductors.

Because the loss should be constrained by a factor representing the permitted loss per unit area, it can be calculated as follows:

$$P_{loss} = q_f a_f = q_f \times 2l_{mt} h_p \quad (9)$$

Therefore,

$$\begin{aligned}
\therefore P_{coil} &= P_{loss} \\
\therefore I_f^2 \times \zeta l_{mt} \times \frac{T_f^2}{s_f d_f h_f} &= q_f \times 2l_{mt} h_f \\
\therefore A_f^2 \times \zeta &= q_f \times 2h_f^2 s_f d_f \\
\therefore h_f^2 &= \frac{A_f^2 \times \zeta}{q_f s_f d_f} \\
\therefore h_f &= A_f \sqrt{\frac{\zeta}{q_f s_f d_f}}
\end{aligned} \tag{10}$$

where  $A_f$  is the m.m.f of the excitation field.

## E. Loss and efficiency estimation

The loss of a synchronous machine should be considered to be the sum of the different losses introduced in 1.2.4.5. However, in traditional machine design, to simplify the calculation, only stator iron loss, stator copper loss, rotor iron loss, excitation loss, mechanical loss and additional loss are considered.

### Stator iron loss

If the total weight of the stator teeth and stator core is defined by  $G_{teeth}$  and  $G_{core}$ , the stator iron loss is calculated as follows:

$$\begin{aligned}
P_{Fe} &= K_{teeth} P_{teeth} G_{teeth} + K_{core} P_{core} G_{core} \\
&= K_{teeth} (p_{teeth} \times B_{teeth}^2) G_{teeth} + K_{core} (p_{core} \times B_{core}^2) G_{core}
\end{aligned} \tag{11}$$

where  $B_{teeth}$  is the average flux density in the stator teeth,  $B_{core}$  is the average flux density in the stator core, and  $K_{teeth}$  and  $K_{core}$  are empirical coefficients. When  $P_N/\cos\phi < 100$  kVgA,  $K_{teeth}=2$ , and  $K_{core}=1.5$ ; otherwise,  $K_{teeth}=1.7$  and  $K_{core}=1.3$ .

### Rotor iron loss

Rotor iron loss is given by the following equation:

$$P_{rotor} = 2p\alpha_p \tau l_m p_{bm} \quad (12)$$

where  $p$  is the pole number,  $\alpha_p$  is the pole-arc ratio,  $l_m$  is the mean length of the machine,  $\tau$  is the pole pitch, and  $p_{bm}$  is a constant representing rotor iron loss per unit area is given by

$$P_{bm} = K_{bm} \left( \frac{Z_1 n_N}{10000} \right)^{\frac{3}{2}} (B_0 t_s)^2 \quad (13)$$

where  $K_{bm}$  is a constant related to the material and the length of the lamination,  $Z_1$  is the slot number,  $n_N$  is the rated speed,  $B_0$  is the maximum value of the teeth flux density, and  $t_s$  is the stator teeth pitch (slot pitch).

### Stator copper loss

Rotor copper loss is calculated as follows:

$$P_{Cus} = m I_N^2 R_a(x) \quad (14)$$

Where  $R_a(x)$  is a constant depending on the insulation class.

### Rotor copper loss

Rotor copper loss consists of the copper loss of the excitation windings and brush and is therefore given by

$$P_{Cuf} = \frac{I_{fN}^2 R_{f(x)} + 0.6 I_{fN}}{\eta_f} \quad (15)$$

$I_{fN}$  is the rated field current;  $R_{f(x)}$  is the same constant, depending on the insulation class, as defined for the stator copper loss; and  $\eta_f$  is the efficiency of the excitation system, usually determined by empirical assumption.

### Mechanical loss

The mechanical loss is estimated as follows:

$$P_{\text{mec}} = 0.8 \times 2p \left( \frac{v}{40} \right)^3 \sqrt{\frac{l_m}{190}} \times 10^3 \quad (16)$$

where  $p$  is the pole number,  $v$  is the rated line speed of the rotor, and  $l_m$  is the mean length of the machine.

### **Additional loss**

Additional loss is estimated as follows:

$$P_{\text{ad}} = K \frac{P_N}{\cos \varphi} \quad (17)$$

$$\text{where } K = \begin{cases} 0.015 & P_N < 75\text{kW} \\ 0.012 & 75\text{kW} \leq P_N < 200\text{kW} \\ 0.010 & P_N \geq 200\text{kW} \end{cases}$$

where  $P_N$  is the rated power and  $\cos \varphi$  is the power factor.

### **Summary**

Using traditional design method is an inaccurate analytical method for determining the main characteristics of a machine. The method provides basic parameters such as the diameter and length of the stator/rotor. However, the calculation of the magnetic field is based entirely on simplified Maxwell equations. The power loss calculation is based on the corresponding constant determined by expert experience and experimental tests. Therefore, the overall design is rather simple but inaccurate. This design method is more often applied in modern machine design as an auxiliary tool or as the first step of the design process.

## **2.2.4 Modern analysis of synchronous machine**

Analytical methods are useful for designing the basic geometry of synchronous machines

and provide good estimates of electromagnetic conditions. However, as previously mentioned, the analyses are based solely on simplified empirical equations, and the results are not accurate. Generally, numerical methods are used instead of analytical methods in modern electromagnetic design for simulating their electromagnetic performance. These methods include both magnetic equivalent circuit methods and finite element methods.

### **Finite element method(FEA)**

Analytical methods establish a problem in terms of discrete variables. In this type of method, it is assumed that a function of several variables can be expressed as a product of functions, each of which depends on only one variable.

$$\varphi(x_1, x_2, x_3, \dots, x_n) = \varphi_1(x_1)\varphi_2(x_2)\dots\varphi_n(x_n) \quad (18)$$

Each unknown function is expressed in the form of a series to represent a general solution for the corresponding differential equations. Common series expansion may include trigonometric functions, Bessel functions, power series and polynomials such as Legendre, Chebychev, and other polynomials. For example, the function expansion for  $\varphi(x_1)$  could be written as

$$\varphi_1(x_1) = \sum A_n \sin(n\pi x_1) \quad (19)$$

Analytical methods are biased towards analytical solutions of the wave equations. As a result, the methods mentioned above can only be applied to devices with a regular shape and homogeneous dielectric.

Finite element methods are based on the basic approach adopted by analytical methods. However, instead of expansion functions over an entire domain, these methods use subdomain functions such as

$$\varphi_1(x_1) = \sum_m a_m \varphi_{1_m}(x_1) \quad (20)$$

$\varphi_{1m}$  are referred to as subdomain expansion functions and are defined over a portion of the domain of  $x$ . These functions could be a pulse, piecewise linear, or piecewise sinusoid function.

The process of separating a function into different subdomains is described as discretization; this process is generally accompanied by the corresponding discretization of a device's shape in the form of cells or elements (commonly triangle shape) to ensure that the dielectric is homogenous over each cell. Inside each subdomain, the same expansion is adopted. The governing equation is solved separately for each of the homogeneous regions [28]. This method is called the finite element method because the design space is divided into a limited number of spaces.

The finite element method has been applied to electrical machines since the 1970 and is generally considered the most accurate method for analysis [29,30]. The discretisation of the problem space into several elements allows for detailed magnetic characteristics, including saturation, to be analysed [31].

However, the computational effort and time and economic costs required for the method are high. The method is accepted as a tool for analysing the performance of a machine in detail rather than as a method directly applied to primary design. Although this problem can be solved with the assistance of a search algorithm, the time and economic costs of the numerical method are still considerable because the model must be updated at each step of the optimisation procedure.

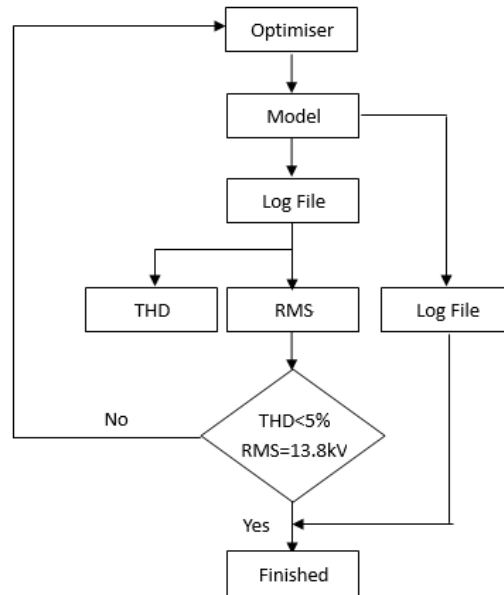


Fig. 11. Optimisation flowchart [30].

Fig. 11 shows a typical optimisation process aimed at finding the design that meets specific requirements (i.e.,  $THD < 5\%$  when the RMS voltage reaches 13.8 KV). The model used lies outside the optimizer and must be updated iteratively with the new settings.

### Magnetic-equivalent circuit method

The magnetic-equivalent circuit (MEC) method is another method for analysing electrical machines that were developed in the late 1980s [32] and widely used in the 20<sup>th</sup> century [33-34]. In this method, the reluctance of each part of a model is assumed to be the combination of individual flux tubes, as shown in Fig. 12.



Fig. 12. Definition of a flux tube and the corresponding reluctance [34].

The tubes are organized in certain ways to form an element (similar to the subdomain

concept in the finite element method, as shown in Fig. 13), and the magnetic characteristics (for example, permeability) are assumed to be unified inside each element. Therefore, a machine is described as a lumped magnetic circuit with certain parameters (also known as a reluctance network).



Fig. 13. Passive 3-D reluctance element [35].

However, although the discretization into elements is similar to that performed in FEA, the calculation in the MEC method is still based on analytical implementations of the virtual work method (VWM), including using spatial derivatives of air-gap reluctances [31, 32, 35], discrete evaluation of energies at two positions [33, 36], or electrical-equivalent circuit formulas based on flux linkages and currents [37].

This method provides a compromise solution between FEA and analytical methods: it involves a relatively lower computational cost than that associated with FEA and relatively higher accuracy than that associated with analytical methods. However, this method is rarely applied commercially due to the difficulty of generating an automatic reluctance network.

## A. Rotor design

Traditional rotor design focuses on changing the rotor geometry to establish a trade-off between competing for optimisation objectives (such as volume vs efficiency or mass vs efficiency) [38]. A conventional salient rotor is regular in shape; therefore, its geometry can be determined by several parameters, as shown in Fig. 14.



Fig. 14. The topology of the traditional salient rotor for synchronous machines [39]. Based on the design objectives, a synchronous machine model is usually a multi-input-multi-output (MIMO) system. It is clearly difficult to obtain an analytical model of this MIMO system. A few studies have attempted to use simplified assumptions to investigate the design analytically [41-43]. Nevertheless, because the equations become complex, it is very difficult to determine the relationships between the model objects and their corresponding variables.

In addition, this analytical model is based on several assumptions. Although these assumptions simplify the calculation, they are unique to regular rotor designs and cannot be generalized when the rotor shape becomes complex.



Fig. 15. Flux path in rotor layer regions [40].

An example of those assumptions is shown in Fig. 15. In this rotor-pole layer, the determination of the quasi-reluctance requires the flux path to be assumed. Therefore, the flux paths are constrained such that the flux density and path trajectory coincide. Therefore, this rotor can only be analysed in this geometry (although the parameters may be varied). It is extremely difficult to predict the flux path for irregular rotor boundaries.

## **B. Stator design**

Stator design is also highly important in synchronous machine design. As shown in Fig. 16, the stator slot can also be defined by several parameters and optimised similarly to a rotor.

However, because stator windings are essential for receiving electrical energy, the winding arrangement is also very important in stator design. Generally, the requirements of stator windings are as follows:

- a) receive a sinusoidal waveform of the symmetrical electromotive force (EMF) with an acceptable magnitude; and
- b) generate a rotating magnetomotive force when a 3-phase current passes through the

device.



Fig. 16. Geometry definition of stator slots [44].

In general, stator windings (or armature windings) can be classified as follows:

- 1) Single-layer/double-layer
- 2) Full-pitch/short-pitch
- 3) Concentrated/distributed

### **Layers**

The concept of a layer is defined by counting the number of coil sides inside a single slot.

If only one coil side is in the stator slot, the structure is called a single-layer winding; otherwise, it is called a double-layer winding. Double-layer windings perform better than single-layer windings in the following respects:

- 1) The windings are easy to manufacture and less expensive.
- 2) Fewer coils are required.
- 3) The windings provide the freedom to apply fractional slot windings.

Although double-layer windings carry the potential risk of internal slot short-circuiting, this risk can be offset by proper insulation. Therefore, double-layer windings are still widely adopted in commercial stator designs.

Single-layer windings are generally considered in fault-tolerant machine design, as the coils remain nonoverlapping, and phase-to-phase shorts are eliminated with one coil side per slot [45,46].

### **Full-pitch versus short-pitch**

If two sides of a coil are 180 electrical degrees apart, the coil is defined as a full-pitch coil. An angle of 180 electrical degrees indicates that the EMF generated by two sides of the coil are opposite and equal to each other. Therefore, if the sides are connected in series, the coil will generate an EMF with double the magnitude. On the other hand, if the angle is not equal to 180 degrees, the two coil sides will have EMFs with the same magnitude and an unequal phase angle. Therefore, the entire coil will have an EMF with a magnitude slightly different from that of full-pitch windings. This coil is called a short-pitch or long-pitch coil depending on whether the electrical angle is less or greater than 180 electrical degrees, respectively. The difference between short-/long-pitch and full-pitch windings is defined by a constant called the pitch factor. Furthermore, because a phase winding is composed of many coils, the angle difference between two coils is defined by a constant called the distribution factor. These constants are calculated as follows to form a winding factor used for analysis:

$$k_{pm} = \cos\left(\frac{m\xi}{2}\right)$$

$$k_{dm} = \frac{\sin\left(\frac{mn\delta}{2}\right)}{n \sin\left(\frac{m\delta}{2}\right)} \quad (21)$$

where  $k_p$  is the pitch factor,  $k_d$  is the distribution factor,  $m$  is the order of harmonics,  $\xi$  is

the pitch angle,  $\delta$  is the distribution angle,  $n$  is the number of coils per phase [47].

### C. Loss Analysis

Generally, only two types of losses are considered in the design of a synchronous machine:

electrical losses and mechanical losses. The former can be split into 5 components:

- Stator conductor losses
- Rotor conductor losses
- Core losses
- Exciter losses/ Excitation circuit losses (corresponding to brush or brushless)
- Additional losses

Mechanical losses are described as friction and windage losses and are measured separately. Details about the other losses are described in the following subsections.

#### Conductor losses

The current flowing through any conductor with internal resistance will generate losses.

These losses will contribute to the Joule heating of the conductor and release heat to the environment. The magnitude of the losses can be expressed by the following equation:

$$P = 3 \times I^2 \times R \quad (22)$$

where  $I$  is the current and  $R$  is the resistance in ohms. The resistance can be calculated as follows:

$$R = \rho \frac{l}{A} \quad (23)$$

where  $\rho$  is the electrical conductivity, which corresponds to the materials properties of the conductor;  $A$  is the cross-sectional area of the conductor in  $m^2$ , and  $l$  is the active length

of the conductor in metres.

Common conductors include copper, aluminium, carbon, and silver. Copper alloys, which combine several materials, are the most common materials for electrical machines. Therefore, copper alloys are qualified by the International Annealed Copper Standard, which classifies alloys based on their conductivity.

Both the stator and rotor of synchronous machines feature conductors. Therefore, conductors are part of both components of a synchronous machine. However, due to the excitation of the rotor, rotor losses are greater than excitation circuit losses alone.

### **Core losses**

Core losses, iron losses or magnetic losses occur in the core of a machine due to changes in magnetic field. For ferromagnetic materials, these losses can be further classified as hysteresis losses or eddy current losses.

### **Hysteresis losses**

Hysteresis loss is caused by the alternating magnetic field during operation. Due to the alternating rotation of the magnetic field, the materials are magnetized and de-magnetized within a short period (usually several milliseconds). After magnetization, the material cannot recover its original state unless it is demagnetized. This characteristic is described in Fig. 17 [48].

When an entire hysteresis loop of a hard-magnetic material is completed, an amount of energy proportional to the area of the loop is lost. This energy, which occurs as heat, is expended, reversing the magnetization zones and stressing the atomic lattice of the

specimen.



Fig. 17. B-H hysteresis curve of a ferromagnetic material [48].

### **Eddy current losses**

Eddy currents are induced electrical currents that flow in a circular path. These currents borrow their name from “eddies” that are formed when a liquid or gas flows in a circular path around obstacles under special conditions. In a synchronous machine, eddy currents are induced by the alternating current in the stator coils and generated along the rotor axis, as shown in Fig. 18.

Eddy-current losses can be minimized by using laminated materials, as in transformers, by using powders dispersed in an insulator or by using non-conducting materials. Hysteresis losses, on the other hand, can only be minimized by selecting a material with a narrow hysteresis loop. Therefore, it is difficult to predict hysteresis losses accurately. An empirical method for estimating iron loss is based on amplifying the corresponding simulation results by a factor called the “loss correction factor” or “build factor”. These

factors are typically equal to or greater than 2, which means that the error can reach 100% or more [49].



Fig. 18. Eddy current on pieces [50].

Traditional analysis software calculates the flux densities at different locations in a structure and simply determines the loss according to the loss table provided by the manufacturer, as shown in Fig. 19. In the loss table, the loss is regarded as a function of flux densities at the appropriate frequency [51].

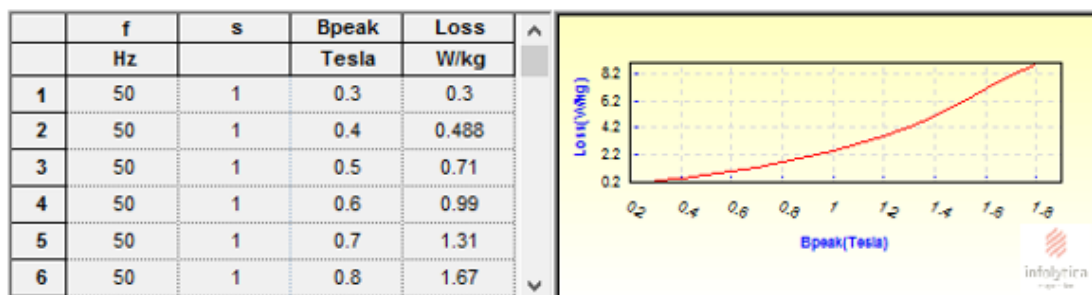


Fig. 19. Loss table.

More advanced Epstein frame loss measurements are adopted in FEA software with the assistance of the Steinmetz equation to isolate eddy current loss. Therefore, each loss can be determined individually.

The Steinmetz equation used to compute loss values at any  $B_{peak}$  and frequency gives the

iron loss P in W/kg as follows:

$$P = K_h f^\alpha B^\beta + K_e (sfB)^2 \quad (23)$$

where the first term corresponds to the hysteresis and anomalous loss (also called Steinmetz loss) and the second term is the eddy-current loss.

For each new material, the best fit of the Steinmetz equation to the entered grid data values is automatically updated. The R-squared value, which indicates how closely the loss obtained from the Steinmetz equation corresponds to the data grid values, is recalculated automatically after any change is made to  $K_h$ ,  $K_e$ ,  $\alpha$ ,  $\beta$  or the data grid values.

### **Friction and windage losses**

Friction and windage losses capture the multiple losses caused by mechanical friction and air turbulence. These losses can be separated into different components, such as bearing friction losses, cooling fan windage losses and windage losses caused by air movement in the air gap [52,53,54].

Bearing losses are dependent on factors such as bearing type, bearing diameter, rotor speed, load and lubrication and can be analytically examined according to the following equation:

$$P_b = 0.5\omega_m k_b F D_b \quad (24)$$

where  $\omega_m$  is the speed of the rotor,  $k_b$  is the bearing constant, F is the force on the bearing (generally considered the weight of the rotor), and  $D_b$  is the bearing inner diameter.

Unlike friction loss, windage loss is highly nonlinear with respect to speed; the corresponding analytical equations are as follows:

$$P_w = 0.03125\omega_m^3 \pi k_t k_r \rho_{air} D_r^4 l_r \quad (25)$$

where  $\omega_m$  is the speed of the rotor,  $k_t$  is the torque constant,  $k_r$  is the roughness constant,

$\rho_b$  is the volume density of air,  $D_r$  is the diameter of the rotor, and  $l_r$  is the length of the rotor.

Friction and windage losses are not technically proportional to speed. However, for a fixed low-speed operation, the losses can be assumed to be constant with respect to the synchronous speed. Therefore, these losses are usually estimated by an empirical formula or computational fluid dynamics and confirmed by experiment.

### **Exciter losses/brush losses**

As previously stated, the rotor of a synchronous machine must be energized to establish the excitation magnetic field. Two types of excitation methods are widely applied in synchronous machines: brush or brushless excitation.

Brush excitation is the traditional method for synchronous machines. The method involves a set of brushes and a slip ring, as shown in Fig. 20.

An external or internal excitation source is connected to the brushes, which are commonly made of electro-graphitic carbon or graphite. Electricity is then conducted through contact between the brush and slip ring and transferred to the excitation windings on the rotor.

The contact between the brush and slip ring introduces many problems, including maintenance issues due to the carbon particles, sparking and brush loss.



Fig. 20. Brush exciter [55].



Fig. 21. Brushless exciter [56].

A brushless exciter is a small AC generator coupled to the rotor of the machine, with its field winding on the main stator and armature winding on the main rotor. Therefore, AC power is generated with the rotation of the main rotor and transferred to rectifiers on the main rotor. The rectifiers then provide direct current to the field windings of the main rotor. Therefore, the use of a brush and slip ring is eliminated, and no brush losses are generated, as shown in Fig. 21. However, that arrangement produces exciter losses, which need to be measured individually.

## **2.2.5 Maintenance of synchronous machine**

Machine maintenance and repair are very important for the industry. When a machine operates abnormally or is completely dysfunctional, a decision must be made on whether to replace it or repair it. Based on economic considerations, repair is a common selection. Therefore, the maintenance costs of a machine should be reduced, and the maintenance procedure should be simple.

As documented in [57]- [58], synchronous machine failure can be categorized into the following types:

1. Stator core defects
2. Winding insulation defects
3. Stator ending winding faults
4. Cooling faults
5. Rotor winding faults
6. Rotor body defects
7. Bearing failure

Failures 1, 4, 6, and 7 are mechanical failures that can only be repaired by replacing broken parts. Failures 2, 3, and 5 can be considered winding failures, whose repair involves winding replacement. Winding failure has been considered the most dangerous threat to large synchronous machines.

These failures can occur in turn-to-turn, coil-to-coil, phase-to-phase, phase-to-ground, and winding-to-iron machines. One turn-to-turn fault induces over-heating, causing the insulation to deteriorate and break down. This fault leads to other faults in the windings,

contributing to machine shutdown and potentially causing the power grid to fail. Therefore, winding failures are not isolated, and repair usually requires all windings to be examined. In general, condition monitoring can be used to predict faults in advance. However, the problem can only be solved by replacing the windings of the machine. Stator winding replacement is relatively easy due to the slot structure. However, rotor winding replacement is a different story.

The rotor windings of synchronous machines are generally strip-on-edge windings (in large machines) and multi-layer wire windings in medium-sized and small machines.

For the former, because the insulation is attached outside the copper, the windings can be addressed separately. If the conductors are in good condition, the coils can be dismantled from the poles, and the insulation surrounding them can be incinerated in a burnout oven. New insulation can be bound to the conductors with a thermosetting resin.

Because the insulation is already bound to the wires, the only solution is to place the entire rotor inside a burnout oven. The rotor coils can only be removed from their laminated pole after burnout. The condition of the pole lamination and damper windings must be checked, and repairs should be completed before installing new windings.

A general requirement for maintenance is to dismantle the windings from the rotor-pole lamination. This dismantling requires the rotor-pole shoe (as shown in Fig.5) to be removed prior to the removal of rotor windings. Therefore, the integrity of the rotor must be damaged in this case regardless of how the original winding was installed. This procedure generates a set of electrical as well as mechanical problems that can generally deteriorate the performance of the machine.

Therefore, the following question is proposed: Is it possible to remove the rotor windings without damaging the integrity of the rotor?

### 2.2.6 Stator vs Rotor winding

A wide range of applications, such as thermal/hydropower plants (steam turbines), wind farms (wind turbines) and isolated power generation (diesel-generator sets) [59-61], use wound rotor synchronous machines(WRSM). In those applications, WRSMs are often operated at constant synchronous speed. However, in wind farms, WRSMs are operating at various wind speeds. The induced power of those WRSMs is converted to normal 3-phase 50HZ power through power converters before connected to the grid.



Fig. 22. The arrangement of the stator winding (distributed).

Stator winding and rotor windings are both required on WRSMs. For the former, stator coils are pre-manufactured distributed windings as shown in Fig.22. They are arranged into the pre-designed slots on the stator covered with insulation papers. Therefore, the stator winding process is relatively easy.

For the latter, since the rotor pole is usually designed larger than the pole arm as shown in Fig. 5. The direct install of rotor windings is impossible. Two possible solutions can be

applied in this case.

Firstly, rotor coils are wrapped around pole bodies using labour forces or rotating machines as shown in Fig.23. Then they are covered with insulation and bounded as distributed windings. Manual winding is time-consuming and inefficient, and the cost of using a winding machine increases with rotor size. To conclude, a general winding method would facilitate the winding installation process.

Secondly, the pole shoe of the rotor can be separated apart. Pre-designed distributed windings are arranged into the pole arms before the pole shoe is fixed on the rotor. However, this method breaks the integrity of the rotor and cause the corresponding mechanical weakness.

Synchronous machines are also prone to winding failures (on both stator and rotor), which may account for half of all machine failures in the field [62]. When machine breakdown occurs, a decision should be made on whether to replace or repair the machine, usually based on an economic analysis. If a rewinding becomes necessary, the rotor (with broken windings) will be placed inside an oven to be burned out. The windings would then become easier to strip. However, the burnout process is dangerous, as heat may damage the core. Tests show that this damage may result in either a reduction in efficiency or overheating of the new winding [63].

If the rotor coils can be pre-produced and inserted into the rotor, similarly to a stator winding, the winding machine can be made smaller, and manufacture costs can be significantly reduced.



Fig. 23. The arrangement of the rotor winding (concentric).

This work addresses the manufacturing issues associated with rotor field windings by modifying the rotor structure to facilitate the assembly of the rotor coils. Various rotor designs are introduced in the following section.

# Chapter 3 Asymmetrical rotor design

---

## 3.1 Aims and objectives

Inspired by the existing asymmetrical rotor design, a new rotor should be designed with features that allows the rotor windings to be installed onto the pole arm without removal of the pole shoe. A 3-D diagram of such a newly proposed rotor is presented in Fig.24.

It is clear based on this topology, that pre-manufactured field coils with insulation and covering can be installed onto the rotor pole from the teeth. Then, they can be slid through the round edges of the rotor and fixed by a non-magnetic shield to offset the centrifugal forces as shown in Fig.24.

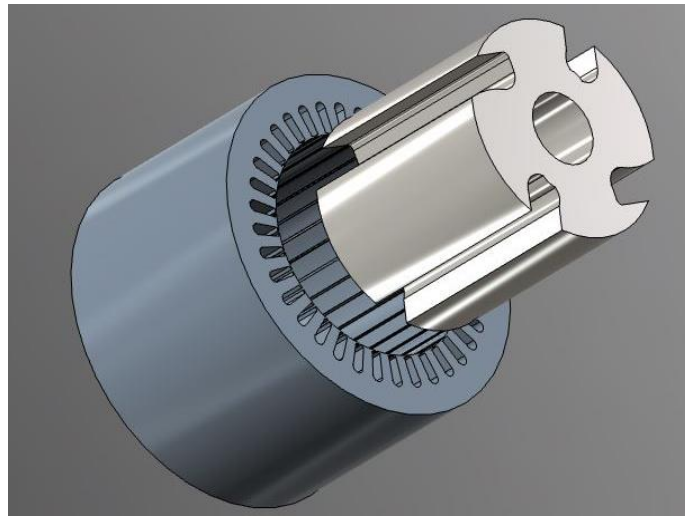


Fig. 24. A three-dimensional diagram of the proposed machine.

For this rotor topology, the segmentation of the rotor poles is no longer necessary which ensures that the integrity of the rotor is maintained. By the direct insertion and removal of the non-magnetic shields, rotor winding and unwinding procedures will be simplified.



Fig. 25. Installation of the rotor coils.

As shown in Fig.25, the rotor windings for this asymmetrical machine are specially designed to be wider than the pole arm, but the difference is controlled to less than 5% of the pole arm width. The empty space is filled with more insulation and bonding materials. The asymmetrical shape of the rotor reveals that the rotor has two parts: a part with teeth (teeth part) and a part without teeth (non-teeth part). Therefore, the machine is designed to operate in unidirectional conditions since the electromagnetic and mechanical performances are different. This kind of machine is suitable for applications such as steam turbines, generator sets and wind turbines, which are the target of this work.

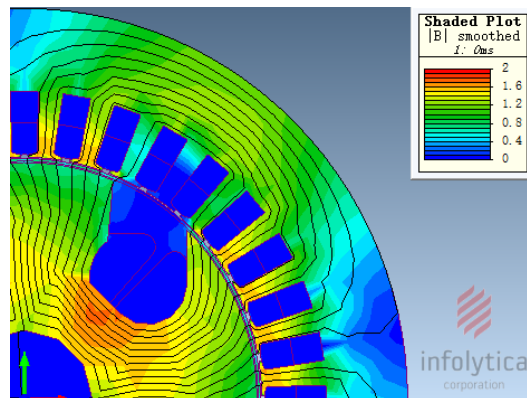
### **3.2 Comparison of two proposed rotors**

Two 2DFE models are produced by Magnet software to evaluate the effectiveness of the proposed designs. The same stator is featured by these two models with different rotors (one symmetrical and one asymmetrical). The machine's stator is derived from a standard 27.5-kVA alternator, while its salient rotor is used as a benchmark against the new design. Specifications of the two generators are shown in Table. 1.

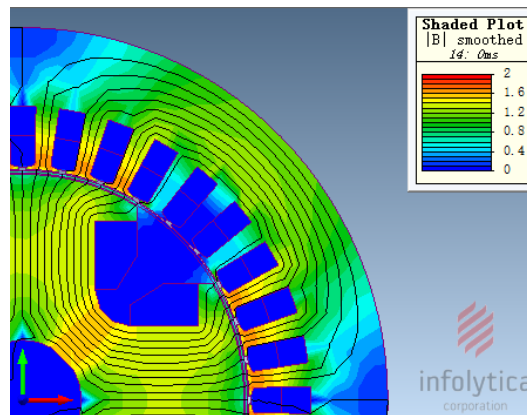
Table.1 Specifications of the two generators

Item	Value	Item	Value
Rated Power	27.5 kVA	Rated Speed	1500 rpm
Rated Voltage	380 V	Rated Frequency	50 Hz
Rated Power Factor	0.8	Stack Length	200 mm
Stator Slot Number	36	Pole Numbers	4
Stator OD	310 mm	Stator ID	192 mm
Rotor OD	188 mm	Stator Winding Arrangement	Double-Layer Star

### 3.2.1. No-load operation



a

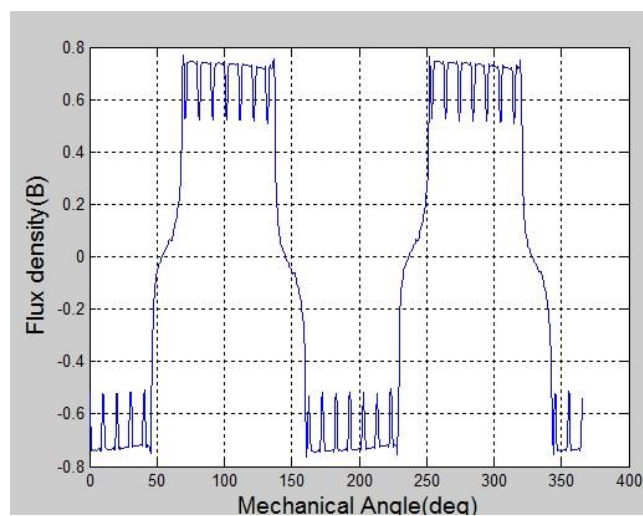


b

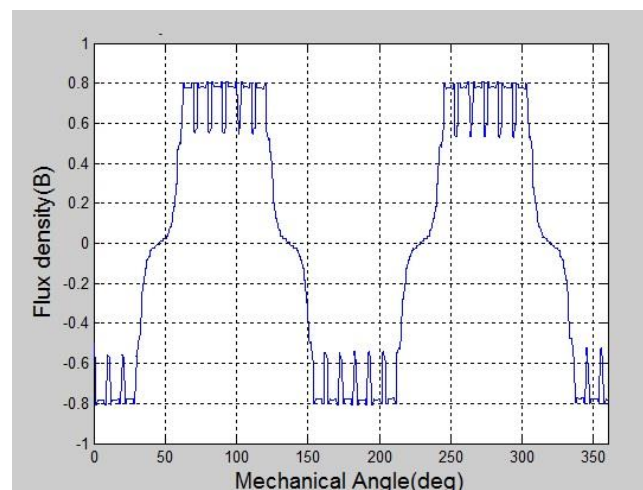
Fig. 26. Flux distribution of the machines at no load. (a) Asymmetrical rotor. (b) Symmetrical rotor.

The studies of the two proposed machines based on their flux-distribution, air-gap flux densities, harmonic level, induced EMF under no-load operation condition are obtained and illustrated in Figs.26-30, respectively.

It is clear that the absence of the rotor teeth reduces the corresponding flux path on the non-teeth side, shifting the flux direction of asymmetrical rotor towards the teeth side of the rotor. This flux distortion leads to clear saturation on the teeth side of the rotor, making the rotor easy to saturate. Easy saturation feature of the asymmetrical rotor is confirmed by no-load test results shown in Fig.30. This feature is also reflected in the air-gap flux density as well as induced EMF as shown in Figs. 27-30.



(a)



(b)

Fig. 27. No-load air-gap flux density. (a) Asymmetrical. (b) Symmetrical.

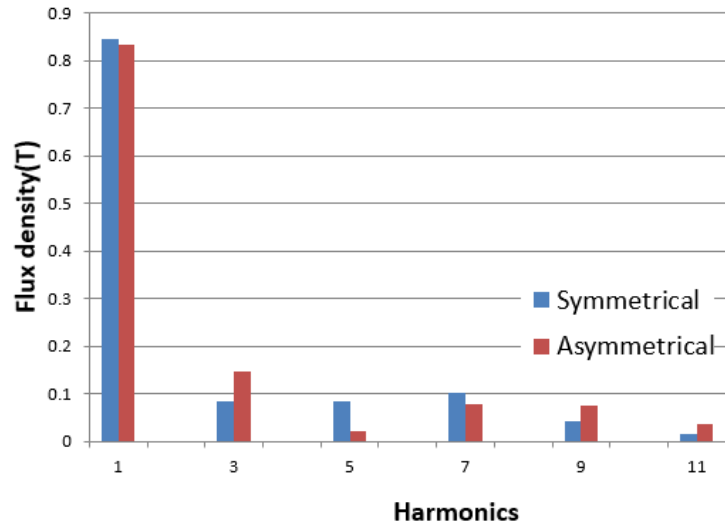


Fig. 28. FFT analysis of the no-load air-gap flux density.

In general, this flux distortion does not produce too many differences in terms of induced phase EMF and air-gap flux density. However, the air-gap flux density of the asymmetrical design is still larger than the symmetrical rotors in the non-teeth side. The results of FFT analysis shows that this air-gap flux density difference creates a higher 3<sup>rd</sup> harmonic but decreases the higher order harmonics. Since 3<sup>rd</sup> harmonic is not a problem in a balanced 3-phase system, it would not be a big issue in this machine design.

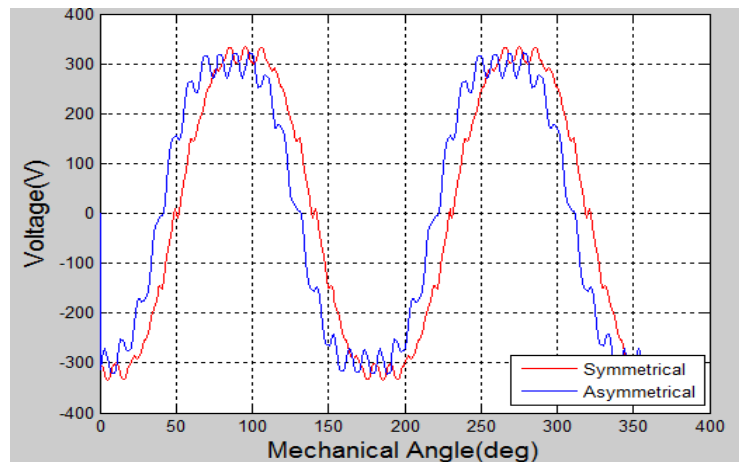


Fig. 29. No-load EMF voltages.

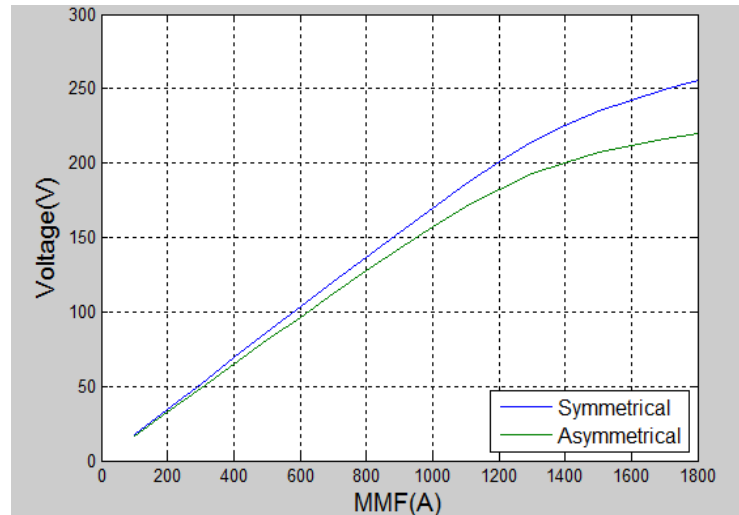


Fig. 30. No-load characteristics.

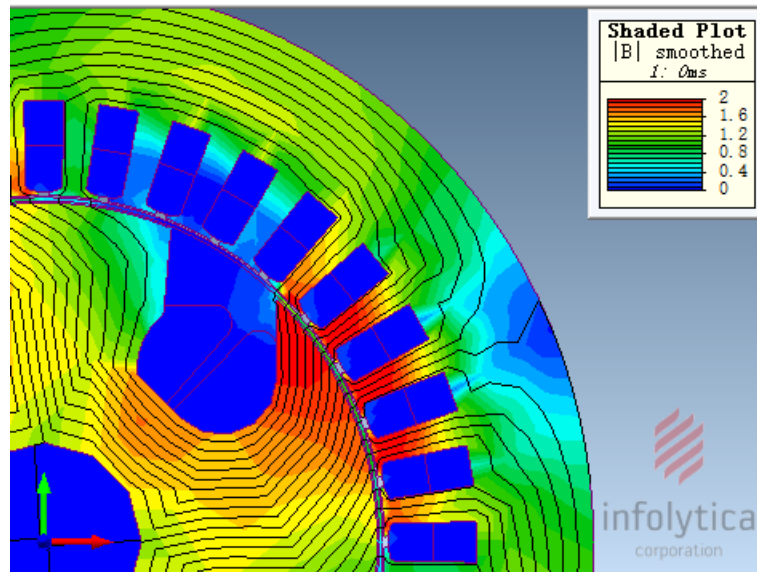
An FFT analysis on the induced EMF is shown in Table.2 confirms its effect on the Total harmonic distortion in induced EMF. However, since the THD is still higher than its symmetrical counterpart, it should still be examined carefully.

Table. 2 FFT analysis of the no-load EMF

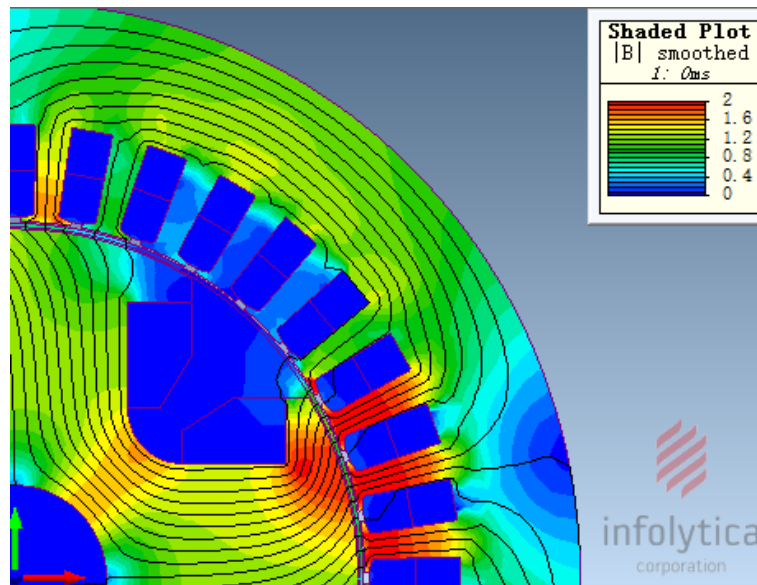
Harmonics	Symmetrical rotor (V rms)	Asymmetrical rotor (V rms)
1	245.47	239.26
3	17.11	26.56
5	3.28	0.822
7	1.95	1.438
9	0.043	0.0234
11	0.162	0.772
THD	7.14%	11.13%

### 3.2.2. Full-load operation

The performance of the proposed machines under the full-load condition is investigated using the flux-distribution and torque production scenarios.



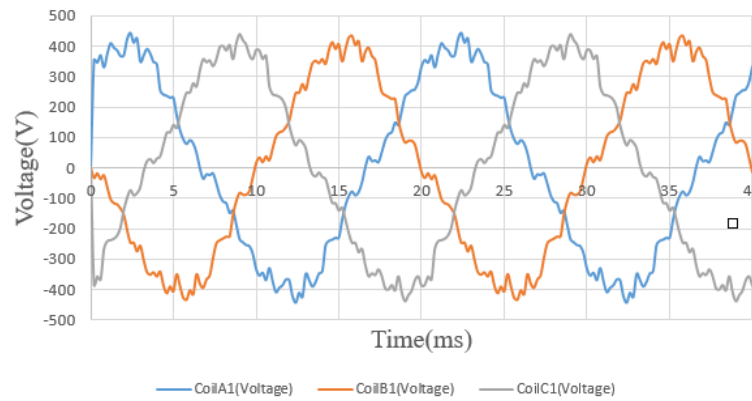
a



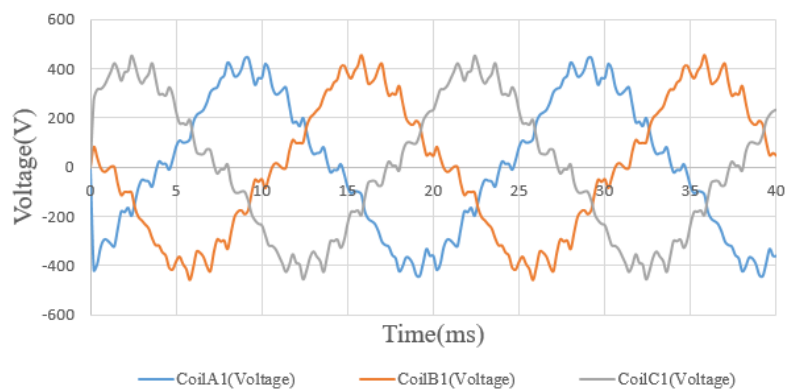
b

Fig. 31. Flux distribution of the machine at full load.  
*(a) Asymmetrical. (b) Symmetrical.*

Due to the torque requirement, flux distortion is much clearer in the full-load flux distributions shown in Figs. 31-33. This leads to a serious saturation in the teeth side of the rotor, especially on the edges.



a



b

Fig. 32. Induced phase voltages of the machines at full load.  
**(a) Asymmetrical. (b) Symmetrical.**

Both maximum torque and maximum torque angle are different between the two designs. However, the maximum torque angle shift is more significant. This confirms the main flux shift shown in the no-load flux distribution, suggesting that the stator and rotor field orientations have moved. This unique feature should be adjusted in the operations. It is clear that most of the non-teeth side are not utilised efficiently. Therefore, there is room for optimisation in the asymmetrical rotor design.

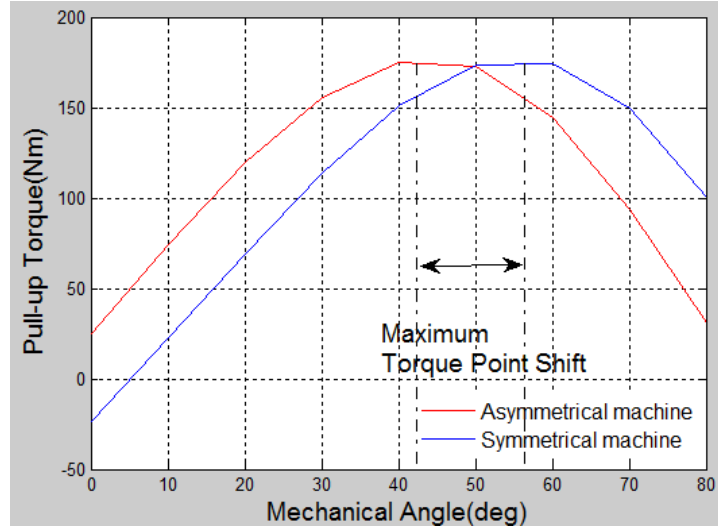


Fig. 33. Pull-out torques.

### 3.2.3. Saliency calculation

As stated in the last section, the torque of the machine has been changed due to the asymmetrical rotor geometry. In theory, it links to the saliency of the rotor. As earlier shown, the flux distribution has been shifted; which leads to the change in synchronous reactance in both direct and quadrature axis.

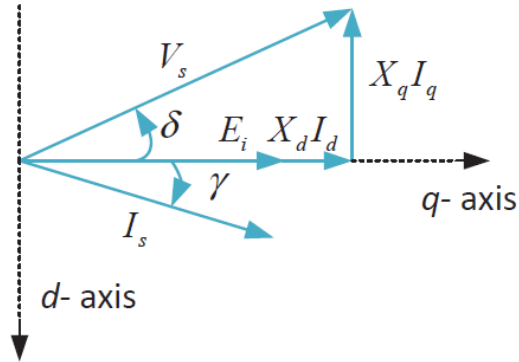


Fig. 34. Phasor diagram

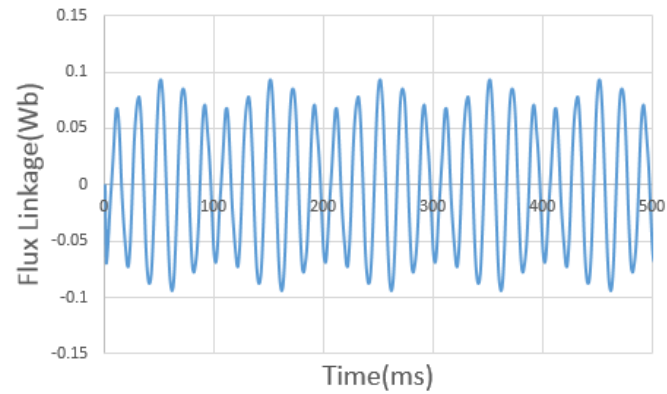
Based on the equations reported in [65], the output torque at any speed can be derived as follows:

$$T = X_{ad} I_f I_s \cos \gamma - \frac{1}{2} (X_d - X_q) I_s^2 \sin 2\gamma \quad (26)$$

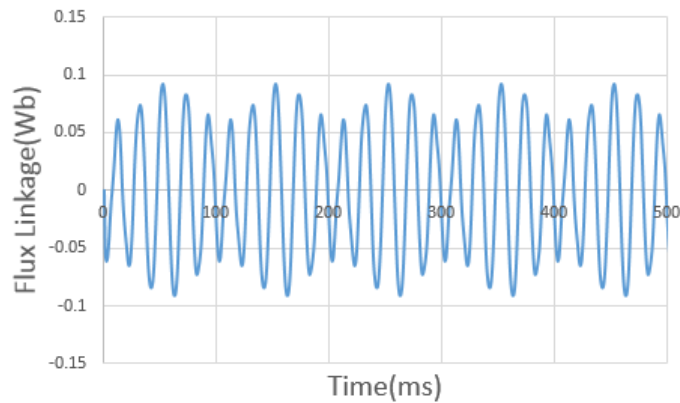
$X_d$ ,  $X_{ad}$  = per unit direct axis synchronous and magnetizing reactance at one per unit speed

$X_q$  = per unit quadrature axis reactance at one per unit speed.

With  $V_s$  defined as the stator voltage and  $I_s$  as the phase current, the first component of the equation can be considered as the stator-rotor field interaction. The second part is the reluctance torque caused by the saliency of the rotor. A phasor diagram of the salient-pole wound-rotor synchronous machine is shown in Fig. 34.



a



b

Fig. 35. Simulated low-slip test results.

*(a) Asymmetrical. (b) Symmetrical.*

Therefore, the direct-axis reactance and quadrant-axis reactance are measured by a low-slip test following the standard method [64]. The rotor is driven by a prime mover to rotate

at 1483.3 rpm (0.01 slip), while the field winding is open-circuited. The stator is fed with a 50-Hz, 4-A alternating current. Since the stator and rotor magnetic fields are asynchronous, their flux linkage is varied, reflecting the flux linkage when they are in different alignments. The test results are presented in Table.3.

Table. 3 D-Q axis reactance of the two rotors

Item	Asymmetrical rotor	Symmetrical rotor
$\Psi_d(\text{Wb})$	384	397
$\Psi_q(\text{Wb})$	153.7	158.6
$X_d(\Omega)$	1500	1500
$X_q(\Omega)$	97.4%	97.5%

Due to the transformation of the rotor geometry, the saliency of the rotor is altered. This change in saliency affects the torque output of the alternator.

### 3.2.4. Power loss and efficiency

The loss and efficiency of the two rotors are calculated using Infolytica Magnet software and shown in Table.4. This shows that asymmetrical machine has a slightly lower efficiency compared to the symmetrical machine due to the iron loss caused by saturation.

Their copper loss is the same due to the same stator configuration and supply.

Table. 4 Loss and efficiency of two synchronous generators

Item	Asymmetrical rotor	Symmetrical rotor
Iron loss (W)	384	397
Torque (Nm)	153.7	158.6
Speed (rpm)	1500	1500
Efficiency	97.4%	97.5%

## 3.3. Experimental tests and analysis of results

The two machines are finalised and prototyped as shown in Fig.36 to validate their performance through experiments. The stator of the machine is a duplicate of a standard Cummins BCI-184F machine. Two rotors are manufactured for

comparison. The details of the machine rotors are provided in Table 3.

Double-layer star connected distributed windings with a surface area of  $144\text{mm}^2$  are applied on each layer of the stator. The symmetrical rotor windings use 76 turns of the copper coil with  $2.3\text{ mm}^2$ ; whereas due to the manufacture requirements, 200 turns of hand-wound  $1.55\text{mm}^2$  copper wires are used on the asymmetrical rotor. Clearly, rated current is different in the two machines; therefore, MMFs have been used during analysis instead of currents.



(a)



(b)

Fig. 36. Photographs of the prototyped synchronous machine.  
**(a) Stator. (b) Asymmetrical and symmetrical rotors.**

### 3.3.1 Constant speed-variable excitation test

Constant speed-variable excitation test is aimed to test the machine's no-load characteristic and analyse its saturation level. This experiment is carried out by coupling the test machine to a prime mover (in this case, DC motor with the drive). The rotating speed of the rotor is controlled at synchronous speed (1500 rpm). Terminal voltage is measured by a power analyser at the terminal of the stator while the stator terminal is under open-circuit condition. Three-Phase AC supply is converted to DC excitation by the rectifier and measured through ammeters at the terminals.

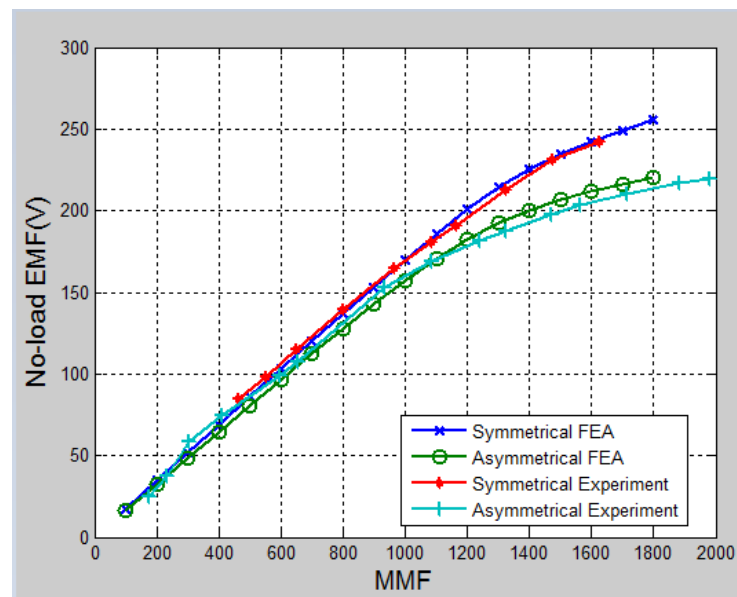


Fig. 37. Comparison of the constant speed-variable excitation test between the two machines.

Following BSI standard BS EN 60034-4:2008, the excitation is changed in steps from rated value to zero using evenly distributed points. Armature voltage (in RMS) at the terminal versus the excitation current (in per unit) at the rated speed is plotted in Fig. 37. The discrepancy between the simulation and experimental test results confirms the FEA

simulation, which indicates that asymmetrical rotor geometry makes it easier for the machine to saturate. There are slight differences between the two results due to the end-winding effect of 2DFE analysis.

### 3.3.2. Constant excitation-variable speed test

This test is to measure the performance of the two proposed machines under various rotating speeds. The armature phase voltage is plotted against speed in Figs. 38-39. The performance of the two was almost identical during this experiment.

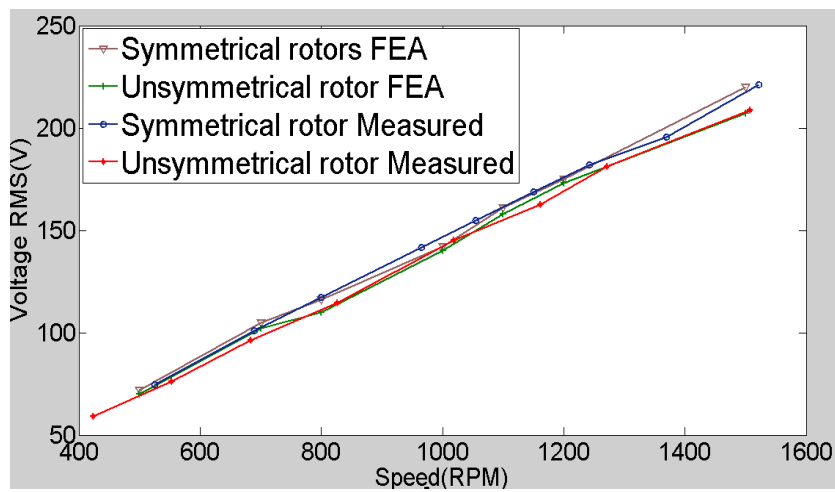


Fig. 38. FEA and measured results of the output voltage.

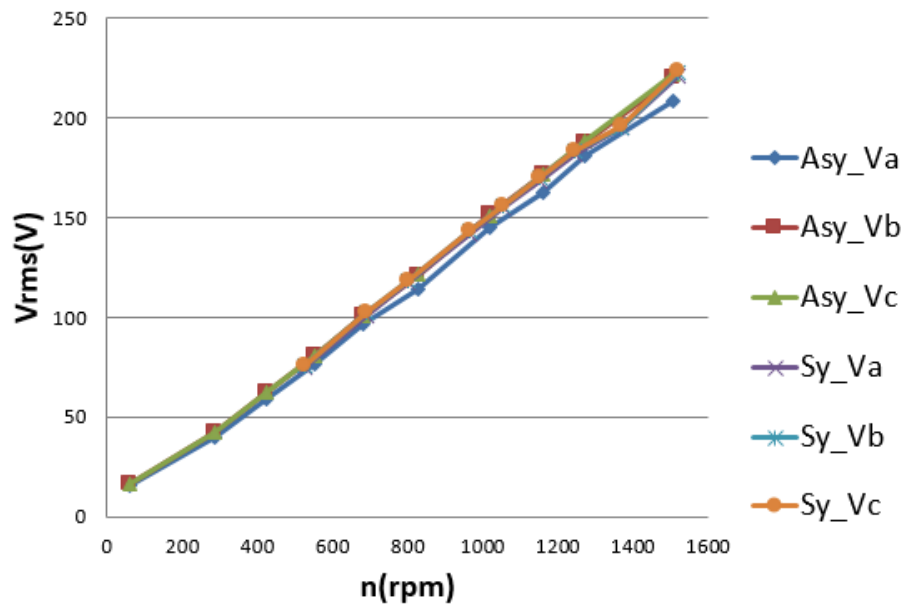


Fig. 39. Comparison of constant excitation-variable speed test between the two machines.

### 3.3.3. Sustained three-phase short-circuit test

The sustained three-phase short-circuit test followed the same pattern as the constant-speed variable excitation tests. However, the measurement of short-circuit current is carried out between short-circuited terminals by ammeters. The armature current versus the excitation current at the rated speed is shown in Fig. 40.

The asymmetrical machine gives a lower short-circuit current compared to a symmetrical machine. This feature should be carefully examined in the fault detection.

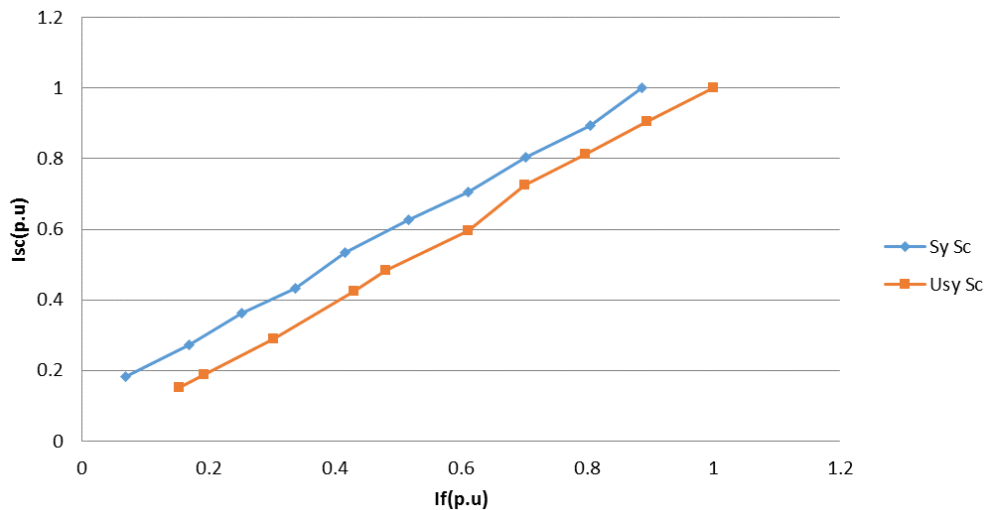


Fig. 40. Comparison of the two machines during sustained three-phase short-circuit test.

### 3.3.4. Inductive load test

Synchronous machine response to inductive load is very important in power system stability because they are the most common type of loads in grids. An inductive load test is carried out with the test machines providing power to inductive load banks. The power generated by the tested machines and their corresponding terminal voltages are measured by a power analyser; while excitation current is recorded by an ammeter. Voltage, current

and power are recorded and presented in Fig. 41.

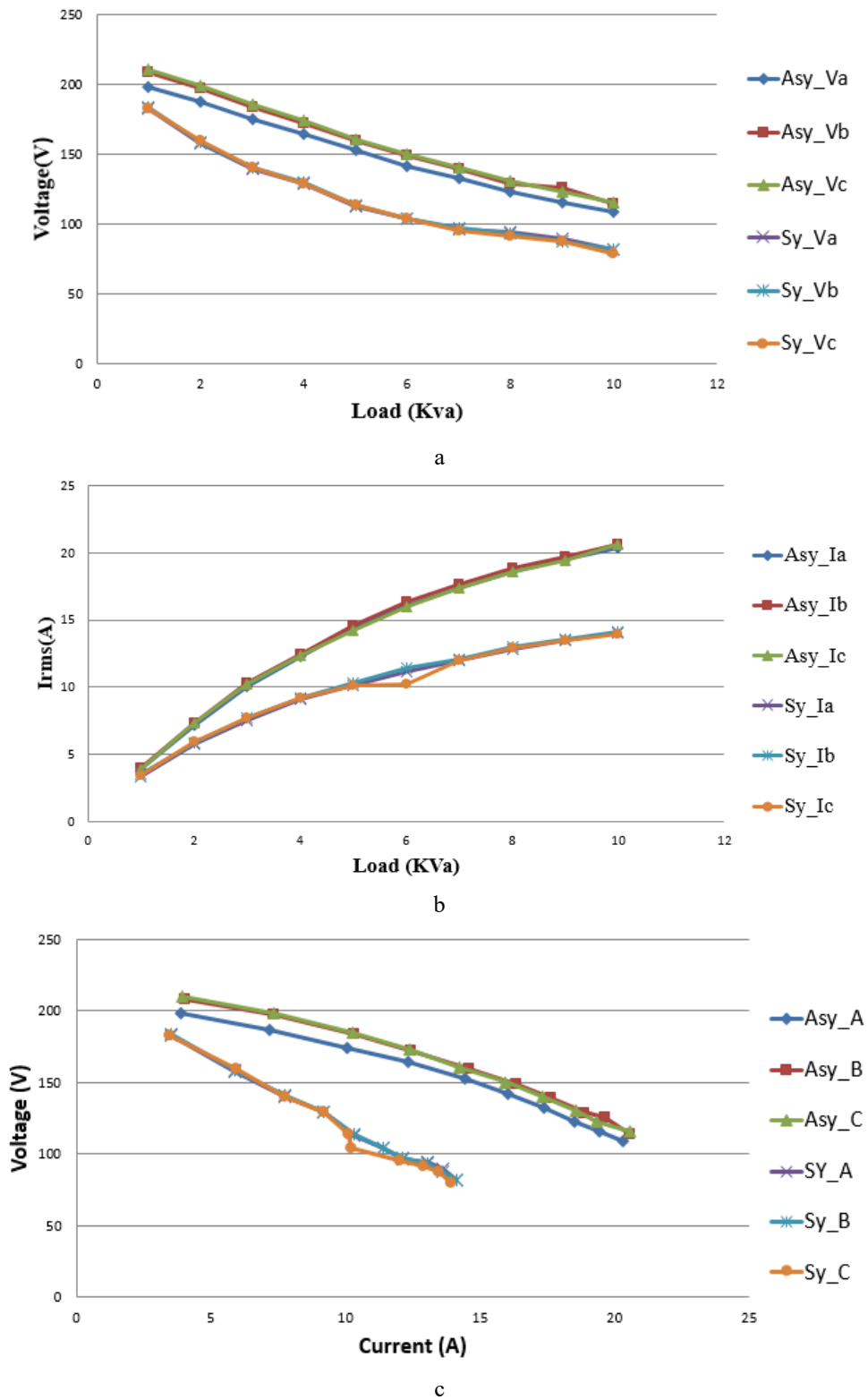


Fig. 41. Comparison of the two machines at varying inductive loads.

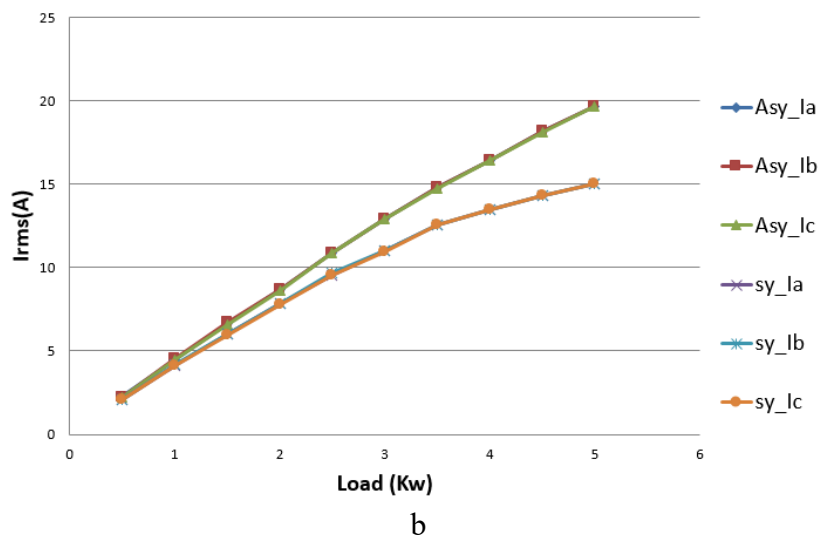
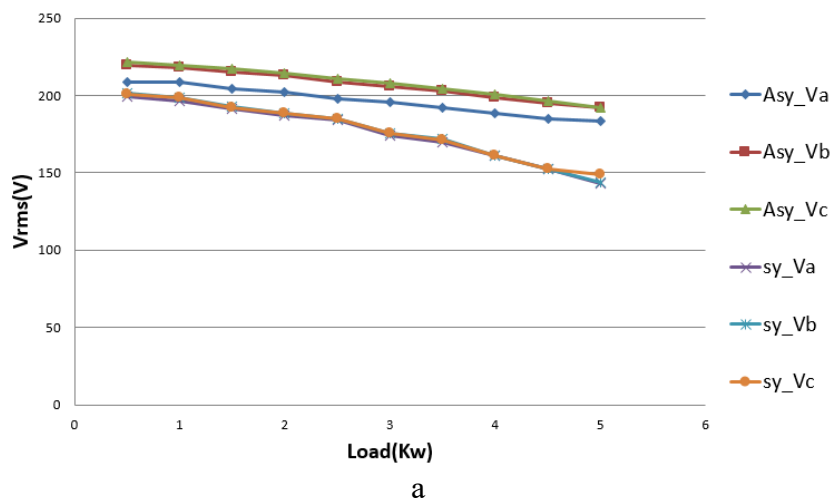
Induced EMF of the asymmetrical machine was less sensitive to the load variation

compared to the symmetrical rotor. The voltage drop is not significant in this case.

Therefore, the proposed asymmetrical design performs better in system stability under load variations.

### 3.3.5 Resistive load test

Setting to resistive load test is similar to inductive load test with the only difference being that, a resistive load is connected to the test machine. The test results in Fig.42 show the same trend as the inductive load test with the asymmetrical rotor performing better in both cases. This finding confirms the excellent performance of the proposed machine under different load conditions.



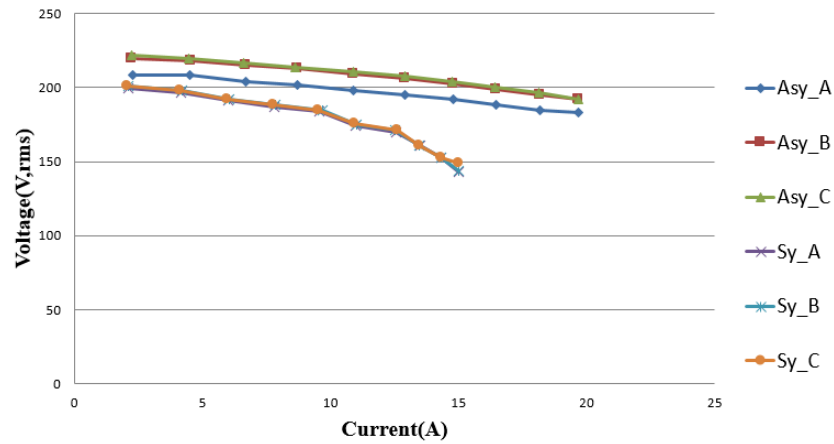


Fig. 42. Comparison of the two machines at different resistive loads.

### 3.4 Summary

This chapter presents a new rotor design of synchronous generators targeted for diesel-generating sets. The rotor pole is asymmetrical, effectively shifting the magnetic field to change the saliency of the rotor. As a result, the power output and the power factor range are affected.

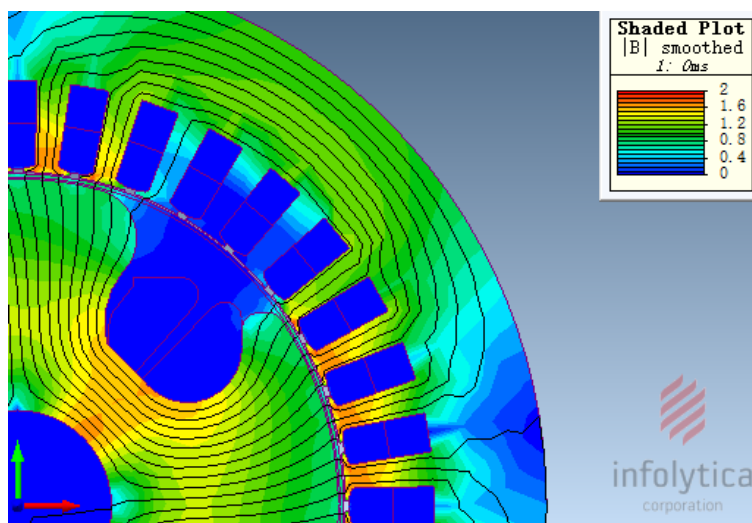
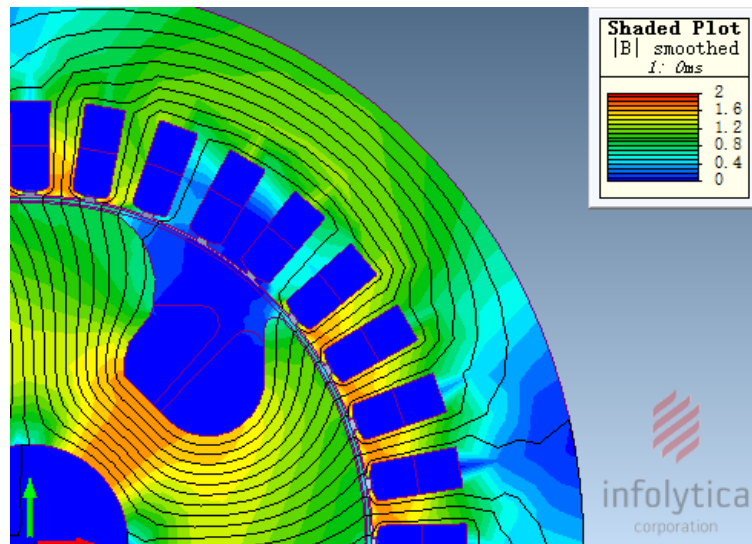
By adopting an asymmetrical rotor geometry, field windings can be easily installed on the rotor, thus simplifying machine assembly and repair procedures. Simulation results obtained from a 2DFE analysis and experimental results obtained by testing a 27.5-kVA prototype machine verify the performance of the new rotor design. Overall, the power profile and the ease with which the field windings are assembled are improved.

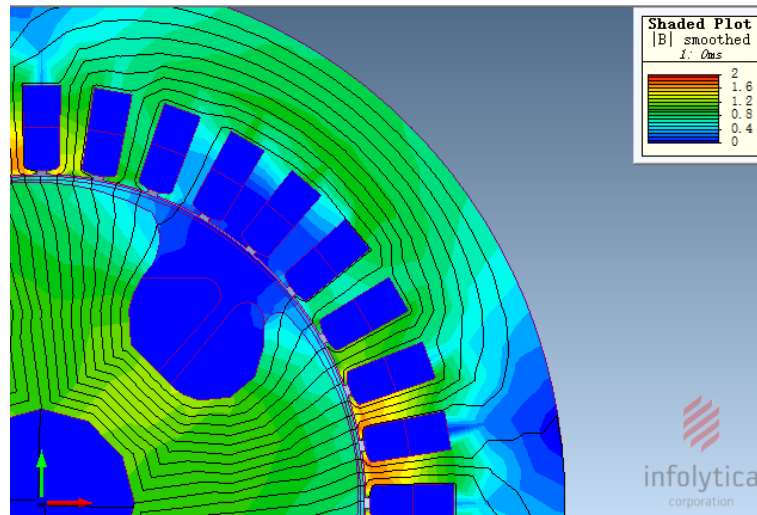
The developed technique can significantly reduce the maintenance and repair costs associated with synchronous generators, particularly for small/medium power-rated alternators and for mass production markets, such as those of diesel generator sets and wind power generators. Machine designers, manufacturers and repair personnel can benefit from this design in terms of reduced capital and maintenance costs.

# Chapter 4 Machine design investigation

As shown in chapter 3, both FEA simulation and experiment test results indicate that the saturation level is a significant problem for the asymmetrical rotor; therefore, the rotor shape is investigated geographically in this section to identify the key geometry factor of the asymmetrical rotor.

## 4.1 No-load operation



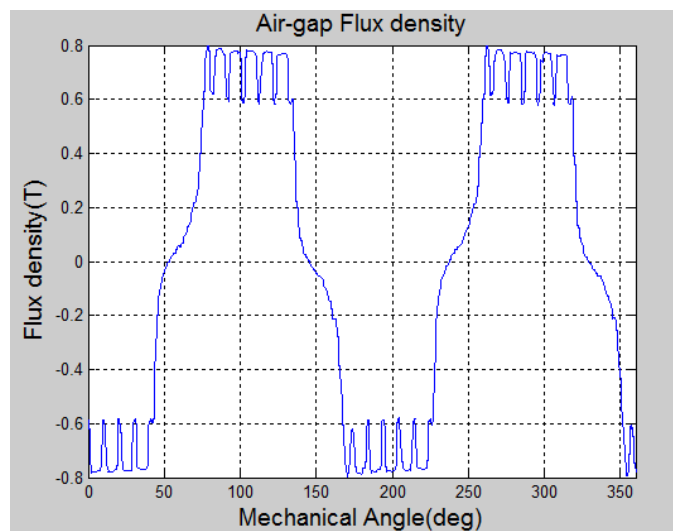


(c)

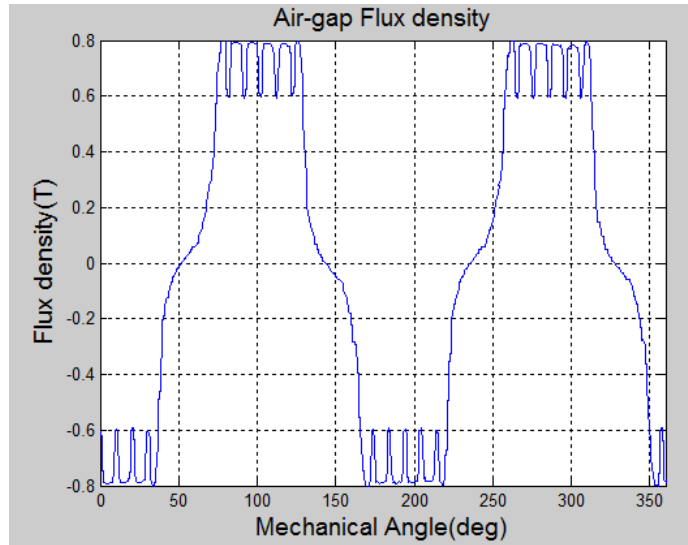
Fig. 43. Flux distribution of the 3 proposed rotor shapes.

Following the principle that flux should be directed towards the centre of the rotor, three plans have been proposed and simulated as shown in Fig.43.

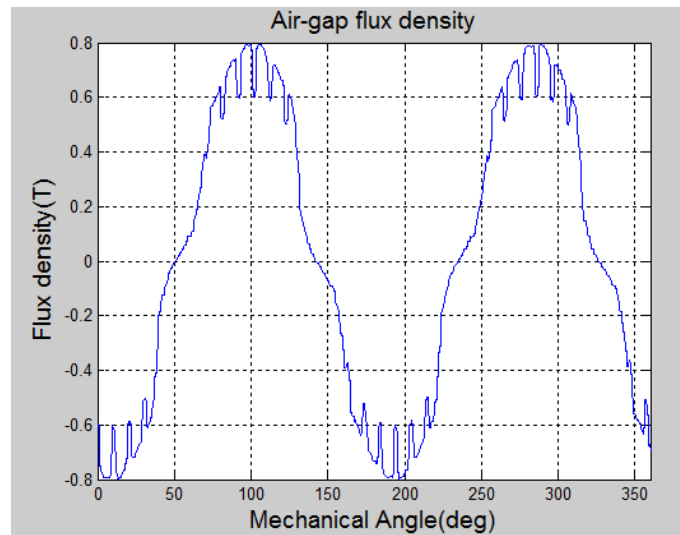
Plan 1 is an advanced design based on the original rotor shape. The vertical edge of the non-teeth side is reshaped and replaced with a smooth half-circle. This generates an extra path for the flux and guides the flux back to the non-teeth side.



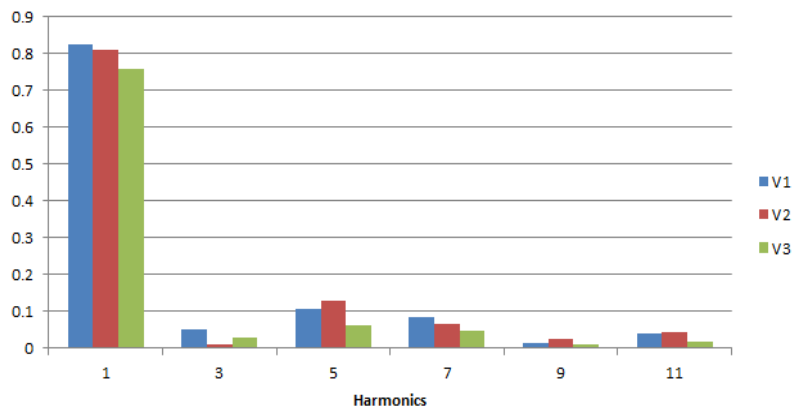
(a)



(b)



(c)



(d)

Fig. 44. No-load air-gap flux density and FFT analysis.

Plan 2 is an improvised version of plan 1, cutting the teeth of the rotor to reduce the flux on the teeth side. Flux distortion in this plan is significantly reduced. For mitigating the effects caused by the shape of edges, an off-centre arc edge is adopted on plan 3. This technology is explained in section 4.3. However, the results are shown here for comparison. As shown in Figs.44-45, plan 1 and plan 2 shares similar induced EMF, phase current and flux linkage. Slight differences can be observed on the maximum value of the air-gap flux density and their corresponding harmonic content. Plan 3 reshapes the edge of the rotor to improve the sinusoidal air-gap flux density. High order harmonics have been significantly reduced in this plan; hence, its effect is further investigated in section 4.3.

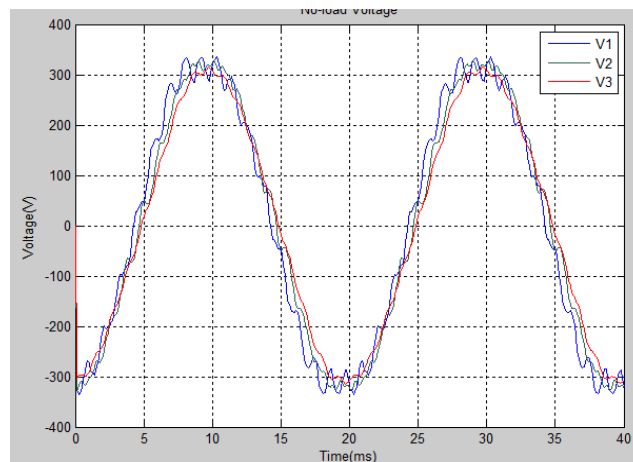


Fig. 45. No-load voltage comparison of three proposed machines.

As predicted in the flux distribution, all 3 plans enter saturation slowly than the initial asymmetrical design under the same excitation. As shown in fig.45, no-load voltage level in the first two plans is increased with a large number of harmonics. Therefore, although plan 3 does not have the best saturation level, it is still considered to be an optimal solution.

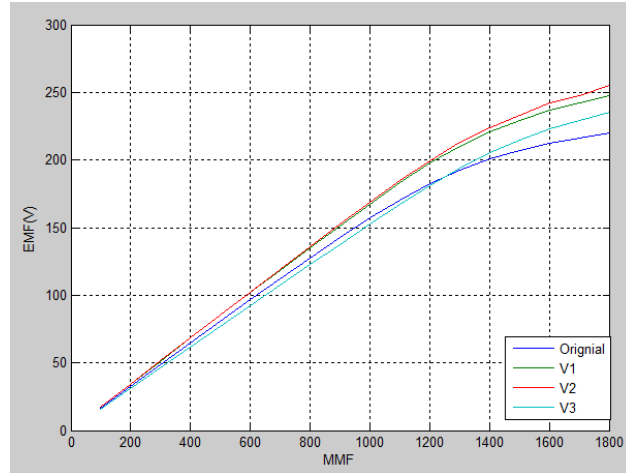


Fig. 46. No-load characteristic of the four machines.

## 4.2 Saliency calculation

Similar to section 3.2.3, the saliency of the machine is measured as follows:

The initial rotor shows that the maximum flux linkage is 0.094 Wb and the minimum flux linkage is 0.068 Wb.

$$L_d = 0.094 / 2 = 0.047 \text{ H}, X_d = \omega L_d = 7.30 \Omega$$

$$L_q = 0.068 / 2 = 0.034 \text{ H}, X_q = \omega L_q = 5.28 \Omega$$

Plan 1 shows that the maximum flux linkage is 0.083 Wb and the minimum flux linkage is 0.053 Wb.

$$L_d = 0.083 / 2 = 0.0415 \text{ H}, X_d = \omega L_d = 6.44 \Omega$$

$$L_q = 0.053 / 2 = 0.0265 \text{ H}, X_q = \omega L_q = 4.12 \Omega$$

Plan 2 shows that the maximum flux linkage is 0.084 Wb and the minimum flux linkage is 0.047 Wb.

$$L_d = 0.084 / 2 = 0.042 \text{ H}, X_d = \omega L_d = 6.52 \Omega$$

$$L_q = 0.047 / 2 = 0.0235 \text{ H}, X_q = \omega L_q = 3.65 \Omega$$

Plan 3 shows that the maximum flux linkage is 0.083 Wb and the minimum flux linkage

is 0.047 Wb.

$$L_d = 0.078 / 2 = 0.039 \text{ H}, X_d = \omega L_d = 6.06\Omega$$

$$L_q = 0.043 / 2 = 0.0215 \text{ H}, X_q = \omega L_q = 3.34\Omega$$

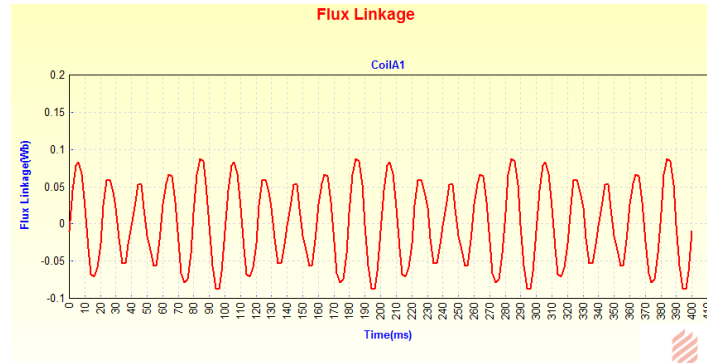


Fig. 47. Low-slip test simulation results for machines.

By checking the d-q reactance, the saliency of the machine is certainly influenced by the rotor geometry. However, the relationship between the geometry boundary and reactance is not proportional and must be analysed quantitatively.

### 4.3 Full-load operation

Similar to section 3.2.2, FEA simulation of full-load operations are conducted for all three plans with the results shown in Fig.48. Torque production of the three plans varies slightly among the machines. All three plans of asymmetrical machine provide almost same pull-up torque as the symmetrical machine. Compared to the original asymmetrical rotor, the maximum power angle of all three plans are shifted relative to the position of symmetrical rotor design. Since both maximum power value and maximum power angle are influenced by the rotor design, optimisation should be considered.

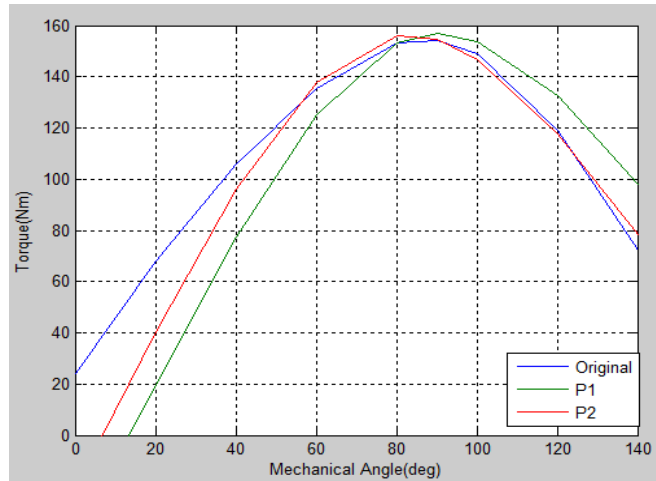


Fig. 48. Comparison of the maximum torque between the three proposed machines.

## 4.4 Stator design investigation

In addition to the change in rotor-pole shape, the winding arrangement on the stator is very important for achieving a high-quality induced EMF waveform. Therefore, plans for distributed double-layer windings are discussed in this chapter.

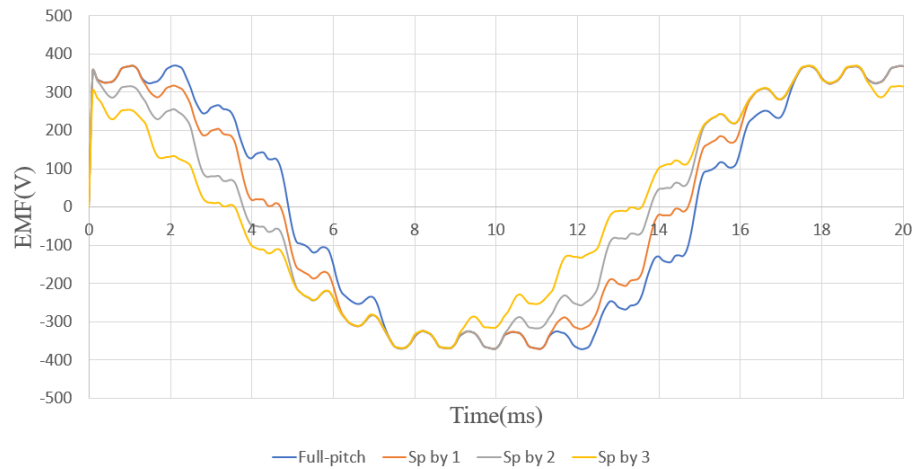


Fig. 49. Waves of induced EMFs for different winding arrangements.

For a 36-slot, 4-pole, 3-phase machine, there are 3 slots per pole per phase. Therefore, the winding arrangement can be either full-pitch or short-pitch with 1 slot, 2 slots, or 3 slots. A 2-D finite element simulation is used to testify the induced EMF with the rated excitation level. EMF waves are shown in Fig. 49, and the results of an FFT analysis are

shown in Table 5.

As indicated by the waves, the short-pitch winding arrangement shows less fluctuation caused by tooth ripple. The short-pitch arrangement introduces fewer fundamental harmonics but provides a better waveform compared with the full-pitch arrangement. Therefore, the short-pitch arrangement with 3 slots is chosen as the solution to the problem. However, it is also observed that the effect of high-order harmonics affects the waveform quality. This problem is studied in the next chapter.

Table. 5 FFT results of induced EMFs for different winding arrangements

	FP	SP1	SP2	SP3
1	398.97	392.91	374.91	345.52
3	51.26	44.39	25.62	0.02
5	2.30	1.48	0.40	1.99
7	7.03	2.41	5.38	6.10
9	12.69	0.01	12.69	0.01
11	3.63	1.25	2.78	3.15
13	0.43	0.27	0.08	0.38
15	12.54	10.86	6.28	0.01
17	31.96	31.47	30.03	27.68
19	1.29	1.27	1.21	1.12
21	1.34	1.16	0.66	0.03
THD	15.93%	14.15%	11.31%	8.28%

An asymmetrical rotor provides a rather irregular flux path, leading to poor-quality EMF waves. However, because the majority of the harmonics are 3<sup>rd</sup> harmonics, it is easy to improve the results by using a short-pitch winding arrangement. A 3-slot, the short-pitch arrangement provides the best solution for the rotor and is adopted in this machine.

## 4.5 High-order harmonic reduction

As indicated in the previous chapter, high-order harmonics strongly affect the voltage waveform quality. Common methods for reducing high-order harmonics caused by tooth

effects include the use of an inverse cosine pole shoe or a centre-offset arc pole shoe [65].

Inverse cosine pole shoes have long been applied in the design of salient wound-field synchronous machines [67-68]. This method produces an uneven air-gap distance according to a cosine function from the rotor d-axis to the q-axis. The air-gap distance is defined as follows:

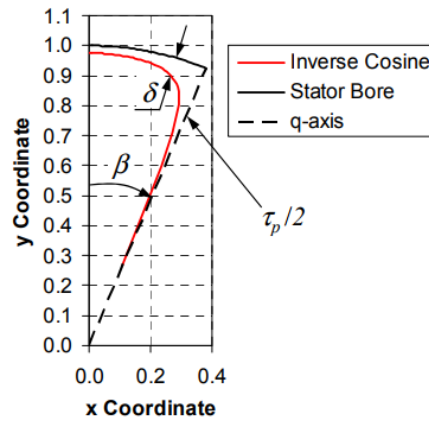


Fig. 50. Inverse cosine function pole shoe of a rotor.

$$\delta(\beta) = \frac{\delta_d}{\cos\left(\frac{\pi}{\tau_p} \beta\right)} \quad (27)$$

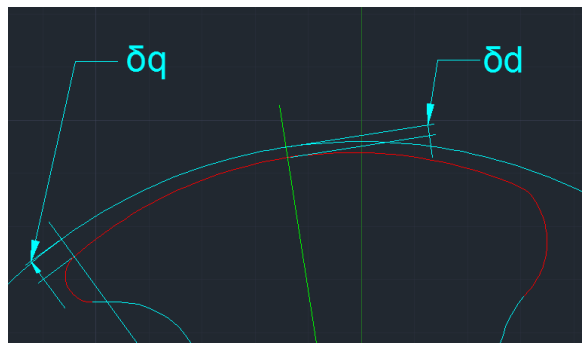


Fig. 51. Centre-offset arc pole shoe.

Investigation of this method shows that it can achieve a good sinusoidal distribution with a high peak value. However, the complexity of the curve makes the method rather expensive for industrial applications. The technique can reduce torque ripple as well as the mean torque. Therefore, it is not ideal in this design.

To simplify the manufacturing process, the centre-off arc pole shoe method is utilized in this design. As mentioned in [68], the advantage of this shape is that the complete pole shoe can be defined by a single arc with a given radius, where the centre of the radius is offset from the origin. Therefore, the design and manufacturing process can be easily executed.

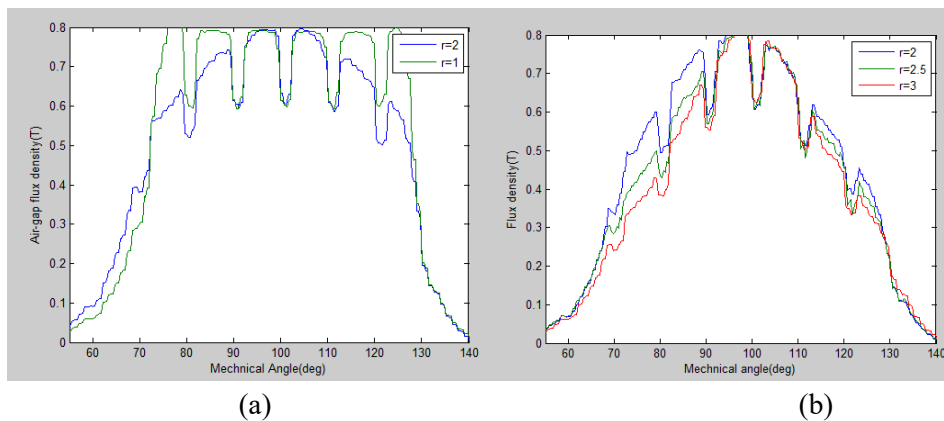


Fig. 52. Effect of ratio on air-gap flux density.

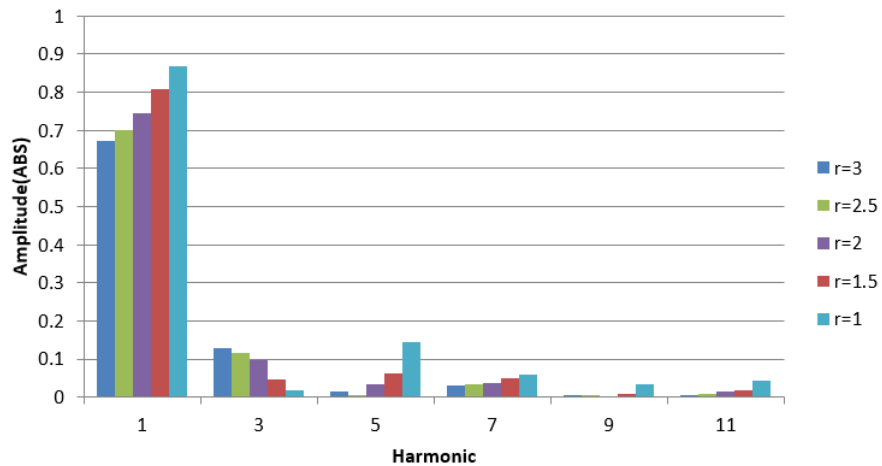


Fig. 53. FFT analysis of air-gap flux density.

Fig. 51 clearly shows that as the ratio  $r$  ( $r = \delta_q / \delta_a$ ) increases, the radius of the arc decreases and the offset of the centre of the arc from the origin increases. Fig. 52 shows the effect of the ratio  $r$  when  $\delta_a = 2$  mm, calculated based on a 2-D finite element analysis. Fig. 53 shows that the air-gap flux density (influenced by the asymmetrical pole arc) is also

asymmetrical.

The FFT analysis is shown in Fig. 53 shows that the fundamental, 5th, 7th, 9th, and 11th harmonics decreases significantly with the ratio. The 3rd harmonic can be reduced by short-pitching the stator winding. Overall, the sinusoidal air-gap flux density can be improved at the cost of relatively low amplitude. Therefore, the ratio should be kept at one appropriate value. The corresponding iron loss and fundamental amplitude of the back EMF are shown in Table 6.

Table. 6 Amplitude and loss at various ratios

Item	Iron loss (W)	Back-EMF Amplitude (V)
Initial design	384	240
Plan 1	304	236
$\delta_q/\delta_d=1$ (Plan 2)	291	230
$\delta_q/\delta_d=1.5$ (Plan 3)	260	222
$\delta_q/\delta_d=2$	232	213
$\delta_q/\delta_d=2.5$	214	206
$\delta_q/\delta_d=3$	203	201

The effect of the air-gap distance is quite clear based on the test performed; however, due to the asymmetrical pole arc, the air-gap flux density is also asymmetrical and highly distorted. However, by combining a proper stator winding arrangement and the off-centre arc method, the harmonics can be controlled to an acceptable level.

## 4.6 Simplified analytical analysis of asymmetrical rotor

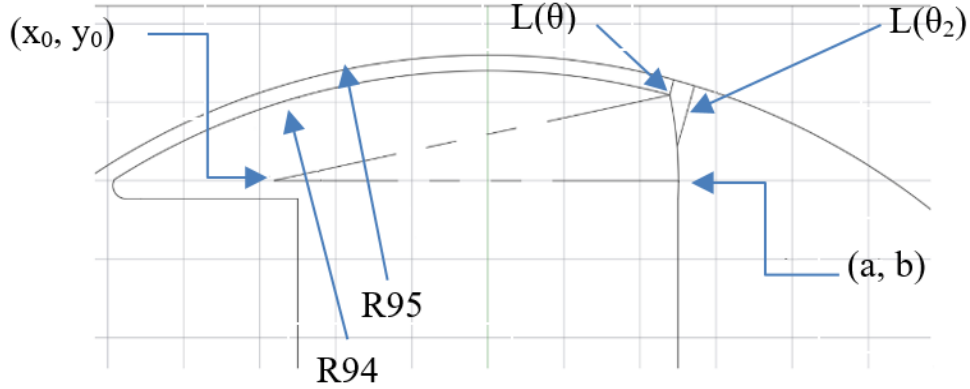


Fig. 54. The parametrisation of plan A.

Stator inner circle:  $x^2+y^2=R_s^2$

Rotor outer circle:  $x^2+y^2=R_r^2$

Arc side: For angles ranging from  $\theta$  to  $\theta_2$ ,

$$\begin{cases} (x-x_0)^2 + (y-y_0)^2 = r_3^2 \\ r_3^2 = (x_0-a)^2 + (y_0-b)^2 \end{cases} \quad (28)$$

Therefore, to estimate the average air-gap distance, these equations are converted to polar form.

For the stator and rotor,  $\rho=R_s$  and  $\rho=R_r$ .

For the arc,

$$\begin{aligned} (\rho \cos(\theta) - x_0)^2 + (\rho \sin(\theta) - y_0)^2 &= r_3^2 \\ \text{when } \theta < \rho < \theta_2 \end{aligned} \quad (29)$$

The equation can be further simplified as follows:

$$\rho^2 = a^2 + b^2 + 2x_0(\rho \cos(\theta) - a) + 2y_0(\rho \sin(\theta) - b) \quad (30)$$

$$\rho = \frac{-[2y_0 \sin(\theta) + 2x_0 \cos(\theta)] \pm \sqrt{[2y_0 \sin(\theta) + 2x_0 \cos(\theta)]^2 - 4[-a^2 - b^2 + 2ax_0 + 2by_0]}}{2}$$

It is assumed that

$$\begin{cases} C_1 = 2y_0 \sin(\theta) + 2x_0 \cos(\theta) \\ C_2 = -a^2 - b^2 + 2ax_0 + 2by_0 \end{cases} \quad (31)$$

Thus, the equation can be further simplified as follows:

$$\rho = \frac{-C_1 \pm \sqrt{C_1^2 - 4C_2}}{2} = f(\theta) \quad (32)$$

The air-gap distance can be calculated for any given point AB as follows:

$$|AB| = \sqrt{\rho_1^2 + \rho_2^2 - 2\rho_1\rho_2 \cos(\theta_1 - \theta_2)} \quad (33)$$

Because the angle is fixed, the equation can be expressed as follows:

$$l(\theta) = \begin{cases} 2 & \theta_{rs} < \theta < \theta_1 \\ \sqrt{\left(\frac{-C_1 \pm \sqrt{C_1^2 - 4C_2}}{2}\right)^2 + R_s^2} - 2\frac{-C_1 \pm \sqrt{C_1^2 - 4C_2}}{2}R_s & \theta_1 < \theta < \theta_2 \end{cases} \quad (34)$$

The average air-gap distance over one rotor pole (one of four in a four-pole rotor) is calculated as follows:

$$L_{avg} = \frac{1}{\tau_{pole}} \int_{\theta_{rs}}^{\theta_2} l(\theta) d\theta = \frac{1}{\tau_{pole}} \left[ \int_{\theta_{rs}}^{\theta_1} 2 d\theta + \int_{\theta_1}^{\theta_2} l(\theta) d\theta \right] \quad (35)$$

When saturation and flux leakage are neglected, the average flux density can be calculated as follows:

$$B_{avg} = \frac{B_r}{\frac{A_g}{A_m} + \mu_r \frac{L_{avg}}{l_m}} \quad (36)$$

The peak-to-peak open-circuit flux linkage is given by

$$\Phi_p = B_{avg} \frac{\pi DL}{2p} \quad (37)$$

The back EMF and torque can be expressed as

$$E_{avg} = K_{dpm} \frac{2N\Phi_p}{2\pi} \omega_r = 2K_{dpm} Np\Phi_p \omega_r = K_{dpm} NB_{avg} DL\omega_r \quad (38)$$

and the torque as

$$T = \frac{P}{\omega_r} = \frac{E_{avg} I}{\omega_r} = \frac{\pi}{2} K_{dpm} D^2 L B_{avg} Q \quad (39)$$

According to the calculation, the average torque depends on the average air-gap flux density, which is influenced by the corresponding constants: a, b, x0, and y0. Because the coordinates a and b are fixed based on the prototype, the two variables that affect the torque performance are x0 and y0, i.e., the coordinates of the centre.

# Chapter 5 Surrogate optimisation

---

## 5.1 Introduction

Modern electrical machines are designed to operate under certain conditions and for specific purposes. For mass-critical applications such as electric vehicles, a high-speed, high-frequency working environment is often required [69]. However, in aerospace applications, designs are tailored to operating conditions characterised by a high working temperature and fault-tolerance and minimal mass [70]. To address a range of operation requirements, an accurate machine analysis method is required.

In traditional machine analysis, analytical models based on electrical equivalent circuits are highly popular [71]- [72]. However, in specific applications, the modelling of eddy currents, saturation and hysteresis losses is difficult. However, analytical methods are performed based on average estimated values of the magnetic field in the air gap and lamination. Therefore, analytical methods offer an advantage in terms of speed but at the cost of accuracy [73].

FEA, on the other hand, is an effective numerical tool for solving magnetic fields. Use of this method can be dated back to 1970 [74]. FEA offers an advanced technique for addressing geometry variations and irregularities. Saturation and eddy current effects can be predicted with high accuracy by FEA [75]. The disadvantage of FEA is its high computational cost. A full model of a machine and its FEA analysis are time-consuming. For example, the finite element models used in the previous chapters takes 20 mins to simulate the performance for 20 ms with the minimum element restricted to 1 mm<sup>2</sup>. In the

machine design process, because every function calls for one FEA, the optimisation time increases proportionally with the number of functions required [76]- [78]. Since the number of functions cannot be estimated in advance, the computational time is unpredictable. A detail discussion of FE and analytical methods can be found in Section 2.2.4.

As mentioned in Section 2.2.4, magnetic equivalent circuit (MEC) based analysis is also a common option, used throughout the 20th century [79-81]. This method is based on physical geometry and material characteristics but incorporates natural flux behaviour. Saturation, leakage, iron losses, etc., can be modelled with moderate accuracy and moderate computational time [82]. However, due to the natural flux behaviour assumption, the effort required to predict the flux path increases with the complexity of the physical geometry.

Surrogate modelling has recently been used in machine design. This technique significantly reduces the analytical effort required by estimating the relationship between machine design input parameters and output characteristics [83]. A simplified mathematical approach is constructed based on output data obtained from high-fidelity models (called sampling points). This approach is then used in machine optimisation instead of the original physical or simulated models, hence the name “surrogate” modelling. This method provides a rapid approximation of objects and constraints. Because it is a mathematical technique, surrogate modelling can easily deploy multiple search algorithms to achieve high-speed optimisation.

Surrogate modelling has been widely accepted in industrial applications such as rotor

blade design [84], aerofoil shape optimisation [85]-[87], electromagnetic device design [88], antenna structure design [89], cooling device design [90] and injector design [91-94]. Although surrogate modelling is recommended as an effective tool for machine design optimisation, a limited number of machine designs are based on surrogate modelling [95-96].

## 5.2 Surrogate modelling

Surrogate modelling can be applied to a wide range of problems because the construction of the model does not require corresponding knowledge of the physical system. As previously mentioned, the basic concept of surrogate modelling is to build a fast and analytically tractable surrogate model by iteratively creating, optimising and updating the corresponding models. A limited number of data acquired from real models are used to create a surrogate model. Because the amount of information carried by the data is not sufficient to identify the real function, a set of estimated equations can be built based on the same data, as shown in Fig. 55.



Fig. 55. Different surrogate models may be constructed with the same data [97]. Therefore, two aspects of surrogate model construction are critical: the estimated formula used to construct based on the available data and error assessment [98]-[99]. Regarding

the former, many types of functions, such as polynomial regressions, Gaussian radical basis functions, neural networks, and Kriging models [100], can be used to predict the performance of physical models. Regarding the latter, the uncertainty caused by insufficient data is treated as a probability density function. This approach indicates that the predicted value of the equation can be located anywhere within a small area covered by the function, as shown in Fig. 56.

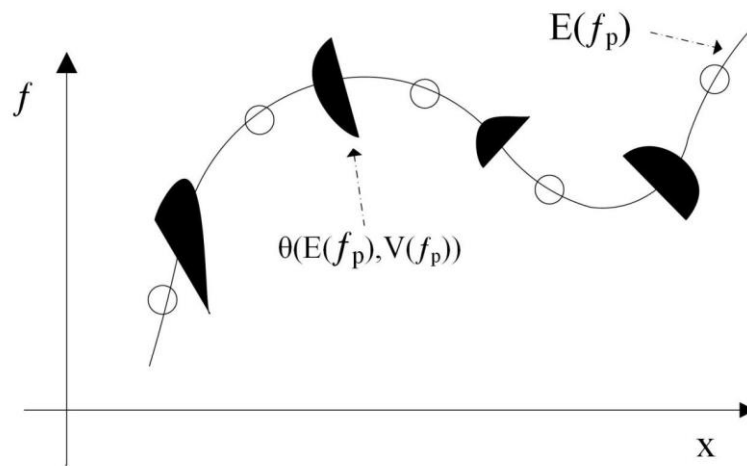


Fig. 56. Predicted uncertain area using probability density function  $\theta$  in the predicted function ( $f_p$ ) [98].

An experiment is first conducted to distribute several sampling points inside the design space. Then, surrogate models are constructed using the previously mentioned prediction approaches. The accuracy of the surrogate model is verified by calculating the convergence of the models. Iteration is performed if the model does not converge. A typical surrogate-based optimisation flow chart is shown in Fig. 57

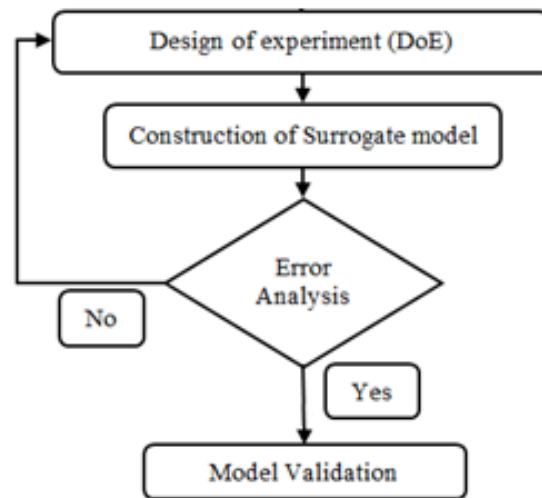


Fig. 57. The procedure of the surrogate modelling method.

## 5.2.1 Design of experiment

### Classic DOE

The first step of surrogate modelling is to locate a certain number of sampling points (specific values of input variables) in the design space. There is a clear problem between the number of sampling points and the information they carry. Generally, the sampling points should be spread as far apart as possible to gain global trends but not so far apart as local trends might be dismissed. However, inevitable random error (because the sampling points are only part of the global space) and bias error (caused by an unbalanced probability distribution in the system) are bound to occur. Therefore, the spread of the sampling points should be controlled using a mathematical method.

Design of experiment (DOE) technology was developed to solve this problem. This technology is used to maximize the amount of information gained by a limited number of

sample points [99,100,101].

Today's DOE technology can be categorized into one of two groups: classic DOE methods or modern DOE methods [102].

Classic DOE methods are obtained based on the assumption that field experiments (sometimes called laboratory experiments) are random and non-repeatable. The corresponding mathematical expression is as follows:

$$y_m(x) = y_t(x) + \varepsilon$$

where  $y_m$  is the measured response,  $y_t$  is the true response, and  $\varepsilon$  is the random error.

Because the random error is independent and assumed to be evenly distributed, the results of two measurements with the same input are still different. Classic DOE methods assume the trend of a true response  $y_t$  is previously known. Therefore, to minimize the influence of random error, classic DOE methods tend to distribute the sampling points as far apart as possible. Therefore, sampling points are often distributed at the boundaries of the design spaces to gain the maximum trends of the true model.

Classic DOE technology uses discretized design variables (often described as levels) to search large design spaces. It is easy to determine, for an  $n$ -dimensional space with  $p$  levels, the total number of sampling points  $n^p$  that should be used to study the effect of each factor on the results as well as the interactions between factors. This DOE method is called full-factorial DOE.

However, the number of sampling points increases exponentially with the number of experimental levels and design variables. To reduce computational effort, fractional DOE methods are adopted. In contrast, if more details are required inside the design space, more

sampling points should be inserted, such as in central composite design, star design, or Box-Behnken design, as shown in Fig. 58.



Fig. 58. Factorial designs for three design variables ( $n=3$ ):

(a) full factorial design, (b) fractional factorial design, (c) central composite design, (d) star design, and (e) Box-Behnken design [103].

## Modern DOE

On the other hand, modern DOE methods are determined based on computer simulation, which can be repeatable and deterministic. In this case, knowledge of general trends is no longer necessary due to the absence of random error. Therefore, sampling points are often located inside design spaces; a process often referred to as “space filling”. This interior sampling displacement is designed to minimize bias error. Popular space filling design methods include Monte Carlo simulation, Latin hypercube sampling and orthogonal array sampling.

### Monte Carlo simulation

Monte Carlo simulation (MCS) is an iterative process of generating random sampling points as input and running the corresponding model for analysis. The mean of the MCS output should converge to the real mean when the number of sampling points is large enough.

If  $g(X)$  is the function considered (where  $X = (x_1, x_2, \dots, x_n)$  is the vector of  $m$  random variables), MCS randomly draws  $m$  samples from the adjoint probability density function  $f(x)$  [104]. The mean value of MCS can be estimated as follows:

$$E[f(X)]_{MC} = \mu_{MC} = \frac{1}{n} \sum_{i=1}^n g(x_i) \quad (40)$$

and the variance is given by

$$Var[g(x)]_{MC} = \sigma_{MC}^2 = \frac{1}{n} \sum_{i=1}^n (g(x_i) - \mu_n)^2 \quad (41)$$

### Latin hypercube sampling (LHS)

Latin hypercube sampling [105] is a typical modern DOE technology widely used in the computation. Two aspects of LHS offer an advantage over other methods. First, LHS can provide a more accurate estimation of the mean value. Second, the method is not restricted by the number of sampling points. Therefore, the technique allows the user to control the complexity and computational cost of sampling.

In LHS, the design space is divided into several bins with the same probabilities. The generation of sampling points is based on two principles:

1. Each sampling point is independently and randomly selected.
2. Only one point is allowed in each bin.

The following is a simple equation for generating LHS sampling points:

$$x_j^{(i)} = \frac{\pi_j^{(i)} + U_j^{(i)}}{k} \quad (42)$$

for  $1 \leq j \leq n$  and  $1 \leq i \leq k$ , where  $k$  is the number of samples,  $n$  is the number of design variables,  $U$  is a uniform value in the range  $[1,0]$ , and  $\pi$  is an independent random permutation of

the sequence of integers  $0, 1, \dots, k-1$ . Subscript  $j$  donates the dimension number, and superscript  $i$  donates the sample number.

As an improvement over the unrestricted stratified sampling method, LHS can be applied to design variables that have an abnormal probability distribution as well as correlations among variables [106]. Therefore, LHS is adopted as the DOE technique in this work.

### **5.2.2 Construction of surrogate models**

Following the appropriate generation of sampling points, a suitable approximation approach is chosen next. Two types of approaches are generally considered: parametric and non-parametric approaches. Parametric approaches, such as the use of a polynomial regression model, assume that the global functions formed between design variables and responses are previously known [107]. Non-parametric approaches, such as the use of radical basis functions (RBFs), treat the global function as a black box and use different types of simple local models in different regions of the data. A compromise approach called the Kriging model has become popular in recent years. A Kriging model is composed of two parts, a parametric part and a non-parametric part. No specific model structure is used, and the non-parametric part is considered the realization of a random process. The following chapter introduces these approximation models.

#### **Polynomial regression model**

Although polynomial regression is the simplest and first surrogate method to be developed, it is still commonly used in engineering design [98].

Polynomial regression models (PRMs) estimate a real function as a combination of a polynomial approximation  $\hat{y}(x)$  and a random error  $\varepsilon$ , which is assumed to be normally distributed with zero mean and a variance of  $\sigma^2$ .

$$y(x) = \hat{y}(x) + \varepsilon \quad (43)$$

A first-order polynomial approximation  $\hat{y}(x)$  is defined as follows:

$$\hat{y}(x) = \beta_0 + \sum_{i=1}^n \beta_i x_i \quad (44)$$

where  $\beta_i$  is an unknown coefficient and  $x_i$  is the  $i$ th design variable.

Similarly, a second-order polynomial approximation  $\hat{y}(x)$  is defined as follows:

$$\hat{y}(x) = \beta_0 + \sum_{i=1}^n \beta_i x_i + \sum_{i=1}^n \beta_{ii} x_i^2 + \sum_{i=1}^n \sum_{j=1}^n \beta_{ij} x_i x_j \quad (45)$$

Parameters estimated using a least-squares method should be calculated as follows:

$$\hat{\beta} = (X^T X)^{-1} X^T f \quad (46)$$

One limitation of PRMs is that the order of equations should be restricted to be less than

2. A high-dimensional, nonlinear problem is difficult to simulate using the PR method.

## Radial basis function

An RBF is a generalized linear model developed for the interpolation of scattered multivariate data [108]. Similarly to PRM, the approach used to approximate the true function is defined as  $\hat{y}(x)$  and expressed as follows:

$$\hat{y}(x) = \sum_{i=1}^n \omega_i \varphi(x) + P(x) \quad (47)$$

where  $\omega_i$  is the weighted coefficient;  $\phi(x)$  is the basis function, which depends on the Euclidean distance between the observed point  $x^{(i)}$  and untried point  $x$ ; and  $P(x)$  is the global trend, which is usually considered constant.

Various basis functions can be used as an RBF, such as Gaussian functions, power functions, thin plate spline functions and Hardy's multiquadric function.

Similarly to a polynomial regression model, a radial basis function can be expressed as follows:

$$f = \omega_j \Phi + \varepsilon \quad (48)$$

The coefficient of linear combinations  $\omega$  can then be computed as follows:

$$\omega_j = (\Phi^T \Phi)^{-1} \Phi^T f \quad (49)$$

and the radial basis function  $\Phi$  is a matrix of the number of sampling points and the number of basis functions  $N_s \times NRBF$ , which is given by

$$\Phi = \begin{bmatrix} \phi(\|r^{(1)} - r_c^{(1)}\|) & \phi(\|r^{(1)} - r_c^{(2)}\|) & \dots & \phi(\|r^{(1)} - r_c^{(NRBF)}\|) \\ \phi(\|r^{(2)} - r_c^{(1)}\|) & \phi(\|r^{(2)} - r_c^{(2)}\|) & \dots & \phi(\|r^{(2)} - r_c^{(NRBF)}\|) \\ \dots & \dots & \dots & \dots \\ \phi(\|r^{(N_s)} - r_c^{(1)}\|) & \phi(\|r^{(N_s)} - r_c^{(2)}\|) & \dots & \phi(\|r^{(N_s)} - r_c^{(NRBF)}\|) \end{bmatrix} \quad (50)$$

It is clear that if  $N_{RBF}=N_s$ , the matrix is a square matrix

## Kriging model

As a technique for interpolating deterministic noise-free data, the use of a Kriging model has become the most popular method in recent decades [110-113]. The function of a Kriging model is composed of two parts: one polynomial model and one isolated symmetrical component representing either small-scale, high-frequency variations or large-scale, low-frequency variations [114].

As previously stated, the isolated symmetrical component reflects the fluctuation around real function, with the basic assumption that these fluctuations are correlated only by the distance between the locations under consideration [98]. To be more specific, a zero-mean second-order stationary process is by the following equations:

$$y(t) = \beta + z(t) \quad (51)$$

where  $\beta$  is a constant value, and fundamental function  $z(t)$  is a Gaussian distribution with an error. The residual error is considered to be independent, identically distributed or normal random variables with 0 mean and variance. Similarly to the previous model, the estimated model for  $y(t)$  can be expressed as follows:

$$\hat{y}(t) = \hat{\beta} + r^T R^{-1} (y - \hat{\beta} q) \quad (52)$$

where  $R$  is the correlation matrix,  $r$  is the correlation vector,  $y$  is the vector of  $n_s$  observed data, and  $q$  is a unit vector. The correlation matrix and vector are

$$R(t^j, t^k) = \text{Exp}\left[-\sum_{i=1}^n \theta_i |t_i^j - t_i^k|^2\right] \quad (53)$$

where  $i$  and  $j$  are independent indices ranging from 1 to  $n_s$

$$r(t) = [R(t, t^{(1)}), R(t, t^{(2)}), \dots, R(t, t^{(n_s)})]^T \quad (54)$$

The parameters  $\theta_1$  to  $\theta_n$  should be solved by applying an optimisation algorithm as follows:

$$\text{maximise} - \frac{[n_s \ln(\hat{\sigma}^2 + \ln |R|)]}{2} \quad (55)$$

A large number of studies have compared the precision of estimated models, and the Kriging method is considered to be among the most accurate in predicting nonlinear and complex real models [115,116]. Therefore, a Kriging model is employed in the surrogate modelling performed in this thesis.

### 5.3 Surrogate optimisation

As previously mentioned, a surrogate model is an approximation of an input and output relationship. Because the features of the design space are first converted to a mathematical approximation, the optimisation process, with the associated objective and constraint functions, can be completed within a relatively short amount of time. Surrogate models can address optimisation problems with non-smooth or noisy responses and reveal trends within given design spaces [94,117,118]. Moreover, multi-disciplinary and multi-objective optimisation can be performed by surrogate-based analysis and optimisation (SBAO) [119].

The flowchart is shown in Fig. 59 describes the SBAO procedure. The purpose of problem definition is to specify the variation range and constraints of the input variables and to clarify the objective of the optimisation by choosing appropriate output variables. The final step is to choose one appropriate optimisation algorithm for SBAO.

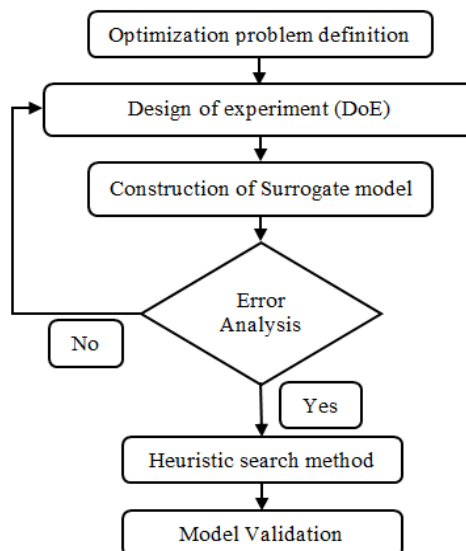


Fig. 59. The procedure of the surrogate modelling method [115].

- *Optimisation problem definition.*

Clarify the variables, the objectives affected by the variables and the corresponding constraints.

- *Design of experiment.*

Locate the sampling points for collecting the maximum amount of information in the design space under the constraint of low computational expense.

- *Construction of surrogate models.*

Select the most appropriate model that fits the characteristics of the information gathered by the sampling points and construct the model using the given sampling points.

- *Infill sampling points.*

Improve the accuracy of the model by comparing the difference between the surrogate estimation and actual models in specific locations.

- *Converge.*

Test whether the convergence of the surrogate model is achieved and decide whether to add more sampling points to train the model.

- *Heuristic search method.*

Find the best location for the problem among multi-objective optimisation problems.

- *Model validation.*

Evaluate the precision of the predicted surrogate model relative to the actual objective function.

## 5.4 Heuristic search method

The optimisation of electrical machines is always a multi-variable and multi-objective problem [120-125]. Important factors include the choices of magnetic, electric and insulation materials used in an apparatus; the magnetic performance of the apparatus; the electrical performance of the apparatus; the method for insulating the apparatus; heating and cooling arrangements; and mechanical design [126]. Analytical methods have been widely used in previous machine designs [127]-[128]. However, the use of a search algorithm combined with FEM has become popular in recent years, as the method provides a solution in a short amount of time and with low computing costs [129,130].

### 5.4.1 PSO

Particle swarm optimisation is a stochastic algorithm developed for optimizing continuous, nonlinear, constrained or non-constrained, non-differentiable multi-objective functions [131,132]. The method is widely used in various fields and applied to different optimisation problems [133-140].

The PSO method selects a number of points in n-dimensional design space to form a population (or swarm). Each particle travels individually at a certain velocity in the space, searching for the best solution. Each particle evaluates its solution based not only on its personal best (*pbest*) but also on the best value among the rest of the population (*gbest*, global best). The particles then change their position in the design space. The change in position (i.e., travelling velocity) is determined dynamically based on the trajectory of

each particle itself and the trajectories of its colleagues. The equations for the new velocity and position are as follows:

$$v_i^{t+1} = v_i^t + c_1 U_1 (pb_i^t - p_i^t) + c_2 U_2 (gb^t - p_i^t) \quad (56)$$

where  $v_i^t$  and  $p_i^t$  represent the  $i$ th particles in iteration  $t$ ,  $pb_i^t$  is the personal best result of particle  $i$  in iteration  $k$ , and  $gb^t$  is the global best of all the particles in iteration  $k$ .  $c_1$  and  $c_2$  are the weight ratios, and  $U_1$  and  $U_2$  are uniformly distributed random numbers between 0 and 1. The first term represents the inertia, which causes the particles to move in the same direction. The second and third terms ensure the particles follow the best personal and best global directions. A flowchart of the PSO process is shown in Fig. 60.

PSO and other search algorithms are compared in various studies [126,127, 139].

Results show that PSO can locate optima accurately in a relatively short amount of time.

It is also suggested that PSO can be simply implemented and can achieve higher efficiency with fewer parameters compared with other algorithms [140]. Therefore, PSO is chosen as the optimisation method in this work.

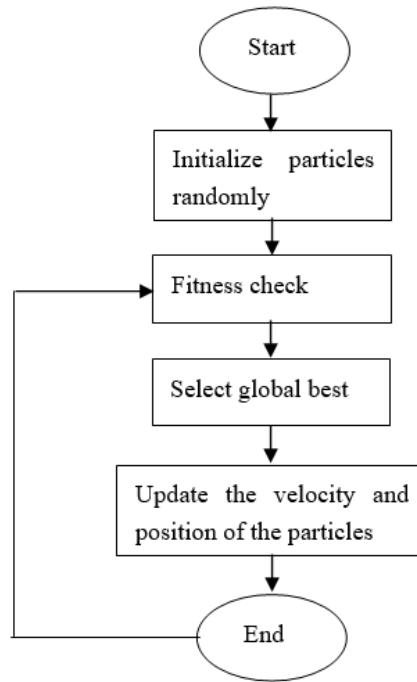


Fig. 60. The procedure of the PSO method [138].

## 5.4.2 Genetic algorithm

Genetic algorithms (GAs) are based on the natural genetic process of biological organisms, i.e., “survival of the fittest”. These methods were introduced in 1975 by Holland [141] and explained in a later series of articles [142-143]. These methods can be applied to highly complex design problems, including machine design [144-146].

The basic principles of GA are explained as follows.

- Coding

In GA, each design choice is defined as a gene. Genes are joined to form a string of values (known as a chromosome) to represent the input variables of a problem. The formation of individual chromosomes can be coded by various methods, including the use of binary strings (most popular), real numbers, permutations of elements, and lists of rules.

After coding, a set of initial chromosomes is generated randomly or based on known suitable results; these chromosomes are defined as the first population.

- Fitness evaluation

Population fitness is tested by a fitness function and selected based on different strategies (such as proportionate fitness selection, linear ranking selection or local tournament selection).

- Reproduction

Selected chromosomes (i.e., parents) are recombined to produce the next population (i.e., child). The chromosomes are recombined based on two methods: crossover and mutation. Crossover takes two chromosomes, cuts parts of the strings and reorganizes them. Mutation is applied to each individual after crossover, randomly changing genes of the chromosome with a certain probability. New populations are generated after reproduction.

- Convergence

If the GA has been performed correctly, the population will evolve towards the global optimum point after several iterations.

## **5.5 Summary**

This section gives an introduction to surrogate optimisation and its corresponding flow steps. By combining surrogate optimisation method with finite element models on geometry design, a compromise is established between a high-accuracy FE method and a low-computation cost analytical method. A detail application of surrogate optimisation is described in the following chapter.

# Chapter 6 Simulation results and analysis

---

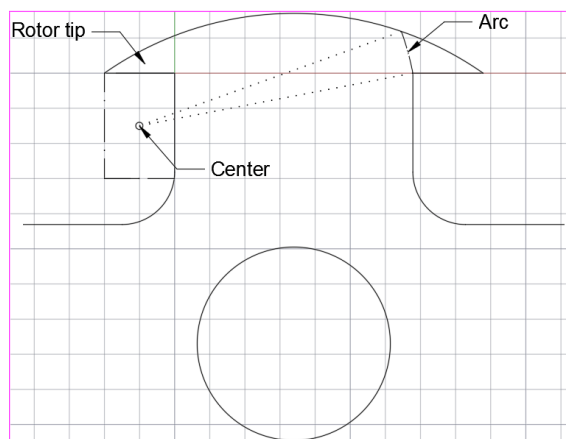
This chapter shows one surrogate optimization process for rotor geometry design in wound rotor synchronous machines.

## 6.1 Aims and objectives

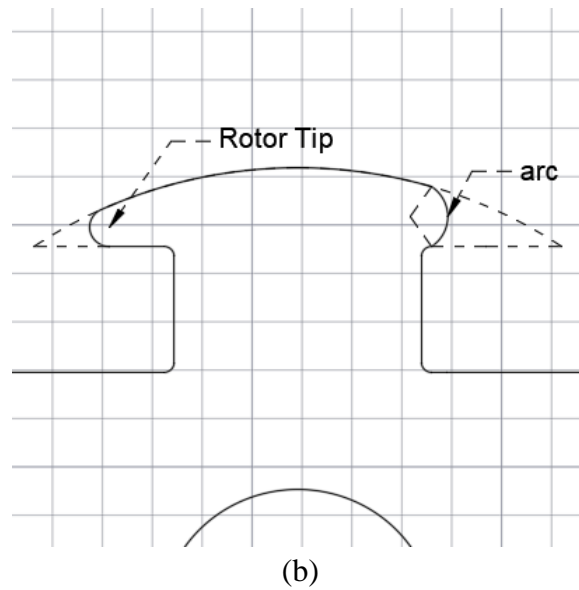
The rotor shape of the original design is created for easy insertion of excitation coils. However, as demonstrated by FEA as well as experimental tests, the majority of the flux is concentrated on the tips of the rotor due to the edge effect.

In this case, the tips of the rotor should be reshaped, to avoid the formation of rectangular edges (creating an even flux path) and to create a uniform air-gap distance along the edge of the rotor. Two plans are proposed and simulated, as shown in Fig. 61.

The aim of this project is to develop a rotor structure for easy installation of excitation windings. Therefore, one side of the rotor tip must be removed to slide the excitation windings onto the rotor pole.



(a)



(b)  
Fig. 61. Optimisation plans.

Plan 1 attempts to cut the right side of the rotor tip with an arc. This arc directly connects the rotor pole to the outside arc, which allows for a smooth path for the flux to pass. The arc separates the rotor into one side with rotor teeth (teeth side) and one side without rotor teeth (non-teeth side). The flux of the rotor can be modified by changing the direction of the arc. Therefore, the edge effect can be reduced.

Plan 2 also connects the pole body to the outer radius with an additional arc. However, the arc side of the rotor tip is not completely removed as in plan 1. In addition, the teeth side of the rotor is cut with a circle. In this case, the direction of the flux can be controlled by changing the shape of the two sides instead of one side alone.

## 6.2 Preliminary test on two rotors

### 6.2.1 Optimisation of plan A

The first step of this optimisation process is to determine the shape based on certain sets of parameters. Problem definition A of plan 1 is shown in Fig. 62. The principle of the plan is simple: Assuming the joint point between the rotor pole and rotor body (indicated

by the star in Fig. 62.) is fixed, a connecting arc can be easily defined by its arc centre  $(x,y)$  and connected at the red point to the outside arc. In this case, the optimisation is clearly a 2-variable optimisation ( $x$  and  $y$ ). The optimisation plan is defined as follows:

**Maximise: *Power output***

**Minimise: *Loss***

**Constraints:**

$$0 < x < 20$$

$$0 < y < 30$$

This optimisation is designed to identify the best performance of the machine, i.e., that which maximises torque with minimal loss.

### 6.2.2 Simulation results

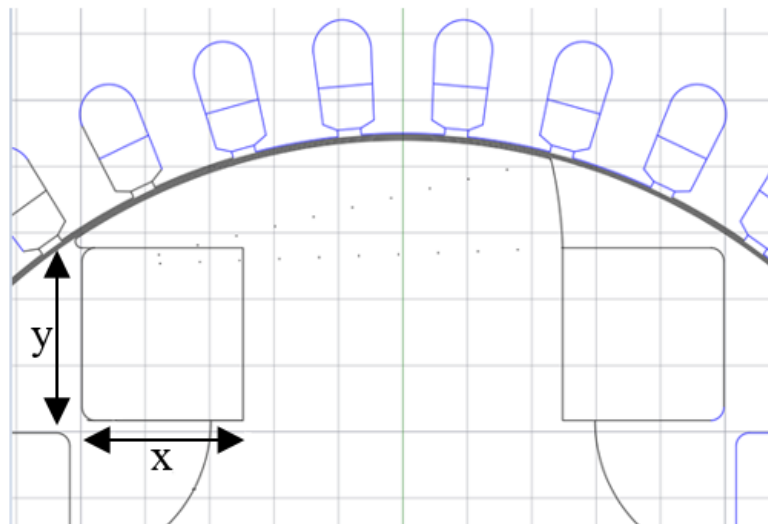
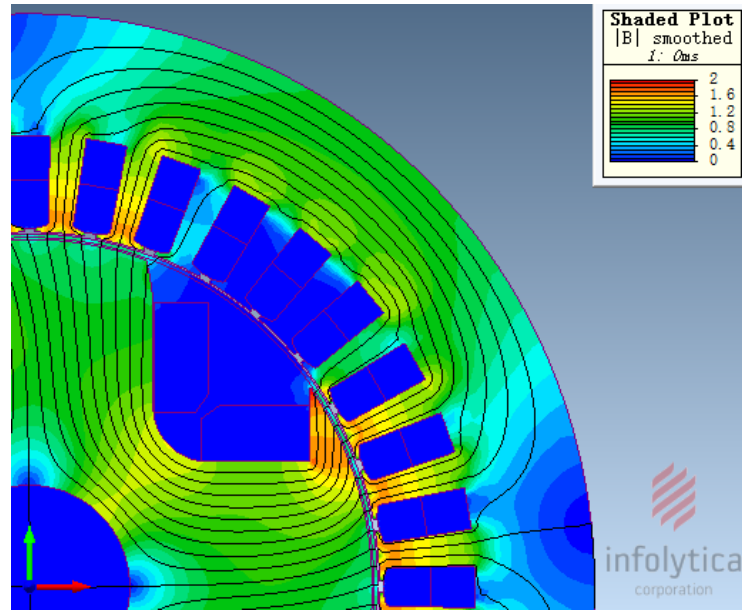


Fig. 62. Problem definition A of design plan 1.

The surrogate optimisation is adopted for this design, as discussed in the previous chapter.

FEA simulations are performed at test points to train the surrogate model. An example of these FEA simulations is shown in Fig. 63.



(a) (b)  
Fig. 63. FEA simulation: no-load flux distribution.

As indicated by the no-load flux distribution, the flux path is shifted towards the tip side of the rotor due to the lack of a flux path on the non-tip side. Changing the centre of the arc controls the flux path of the rotor. This unique flux change has a negative effect on the induced voltage. Three-phase induced voltages of the rotor are shown in Fig. 64.



Fig. 64. Three-phase induced voltages.

It is also observed that in this design, the flux has a natural angle between the geometrical centre and magnetic centre. Therefore, the maximum power angle is different from that of the conventional rotor. During the simulation, one extra angle is added to achieve

maximum power. The full-load operation is shown in Fig. 65.

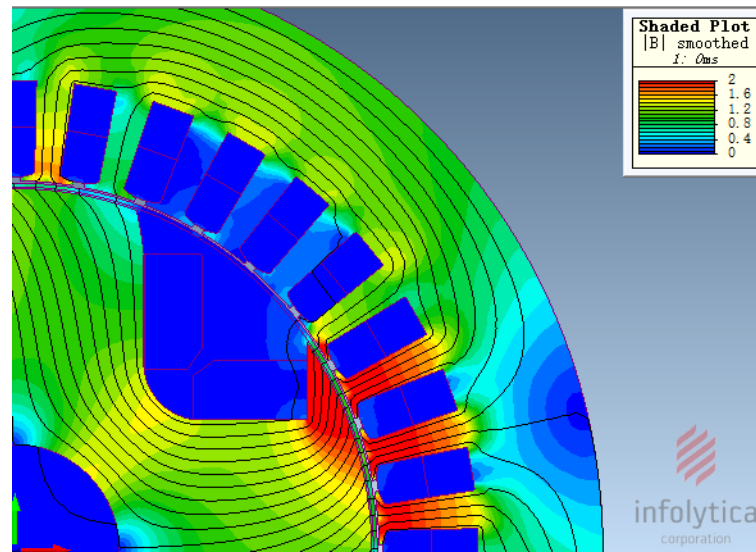


Fig. 65. FEA full-load flux distribution.

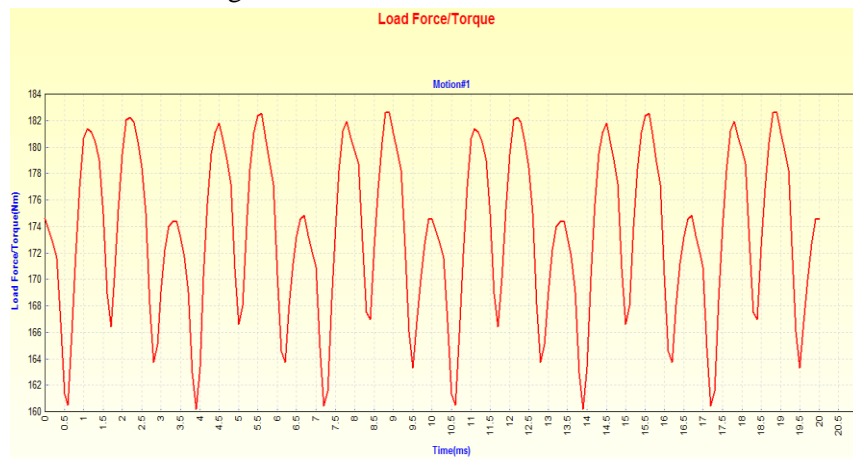


Fig. 66. Estimated torque production.

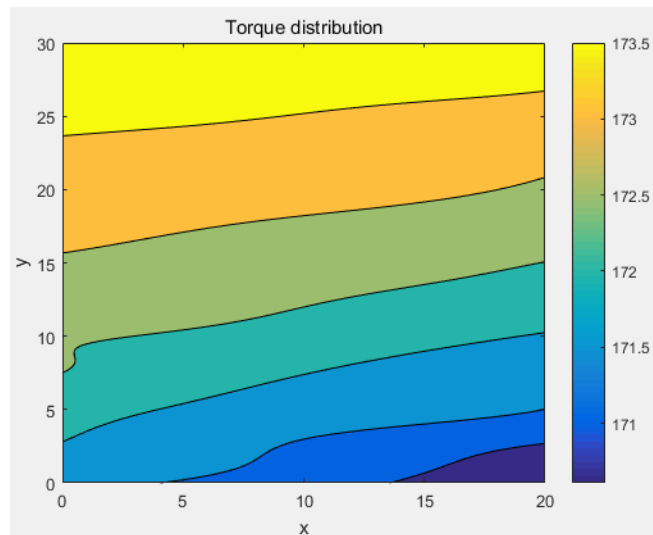
The surrogate optimisation uses 50 training points. After training, the surrogate model is as shown in Fig. 66.

As shown in Fig. 67, the surrogate model indicates that the torque is distributed linearly.

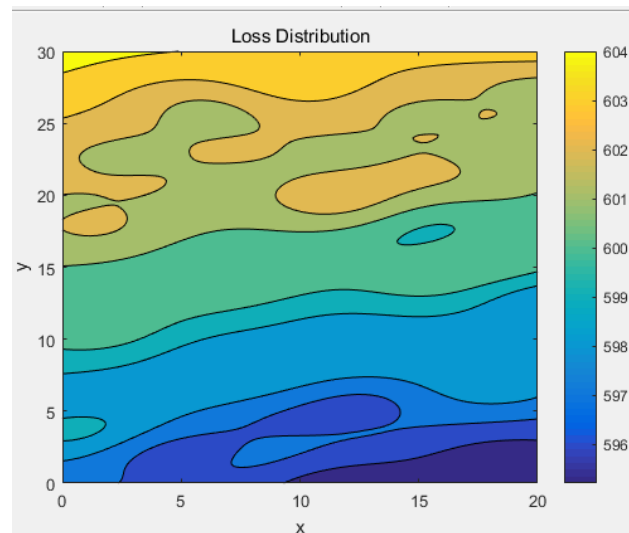
The highest torque is consistently achieved on the top right side of the design region.

However, the loss is quite nonlinear and distributed unevenly around the entire design

region. Therefore, the PSO search algorithm is adopted for optimisation.



(a)



(b)

Fig. 67. Surrogate models: (a) torque distribution and (b) loss distribution.

Using the PSO search algorithm, the surrogate optimisation provides suitable estimates.

The optimal point is set to  $[15.55, 17.94]$ , where the estimated torque is 173, and the estimated loss is 374.99. The optimized results are confirmed by FEA simulation. To verify the accuracy of the surrogate models, several test points (selected by LHS) are also simulated with the optimized points.

Table. 7 Accuracy comparison between surrogate model and FEA results

Item	x	y	Torque (FEA)	Torque (SE)	Error	Loss (FEA)	Loss (SE)	Error
Test_1	12	5	171.7	171.42	0.28	597.04	596.7	0.34
Test_2	8	23	173.37	173.36	0.01	601.97	602.04	-0.07
Test_3	6.32	28.42	173.69	173.71	-0.02	603.82	603.33	0.49
Test_4	4.21	0	171.52	171.5	0.02	587.02	596.82	-9.8
Test_5	3.16	17.37	173.06	173.05	0.01	601.94	601.8	0.14
Test_6	18.95	22.11	173.07	173.11	-0.04	600.38	601.6	-1.22
Test_7	5.26	11.05	172.54	172.56	-0.02	600.27	599.85	0.42
Test_8	9.47	14.21	172.7	172.71	-0.01	600.29	600.33	-0.04
Test_9	0	6.32	171.42	172.37	-0.95	597.02	598.57	-1.55
Optimised	15.55	17.93	172.88	172.89	-0.01	600.32	599.98	0.34

As indicated in Table 7, the accuracy of the surrogate models is confirmed by FEA simulation. The number of training points is the most important factor affecting the accuracy of the surrogate model. Therefore, another surrogate with 20 sampling points is simulated. Because new operation data are received, the machine is set to operate in different conditions under which the stator current is reduced.

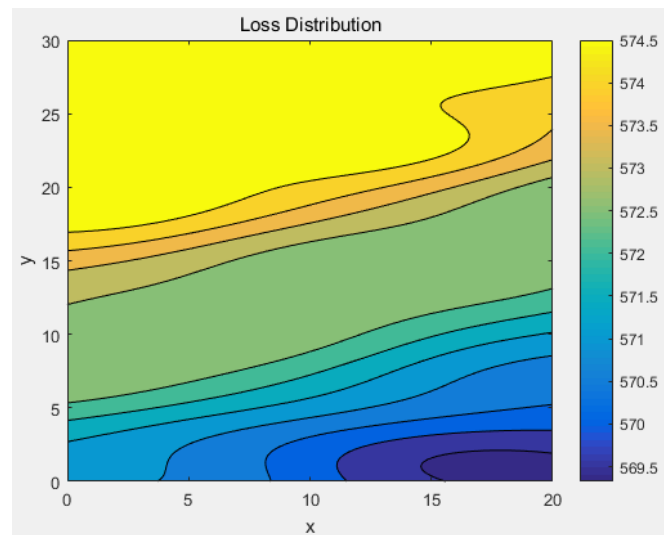
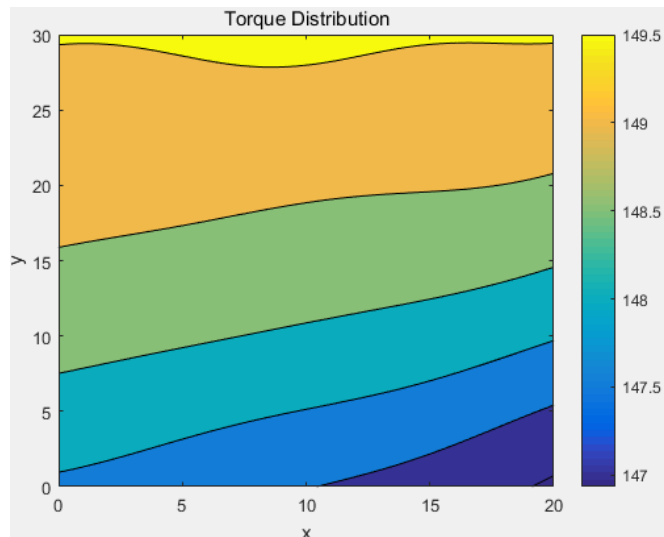


Fig. 68. Twenty sample surrogate models: (a) torque distribution and (b) loss distribution.

The results in fig.68 show a distribution similar to the previously described distribution. However, it is clear that in this surrogate model, due to the reduction in the number of training points, the accuracy of the model is reduced. The prediction on the top left side of the design area is underestimated. Therefore, the number of training points should be increased in that area.

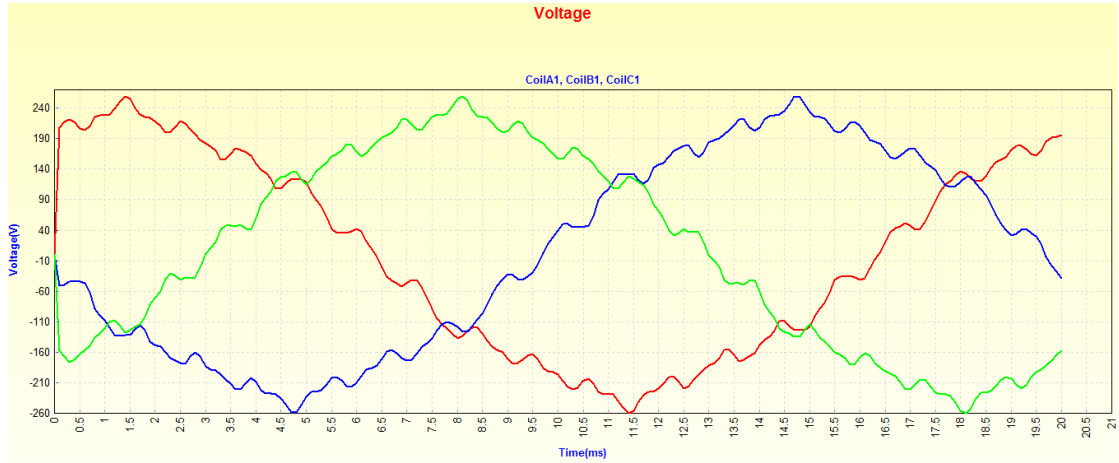


Fig. 69. Three-phase induced voltages of 2/3 short-pitch rotor.

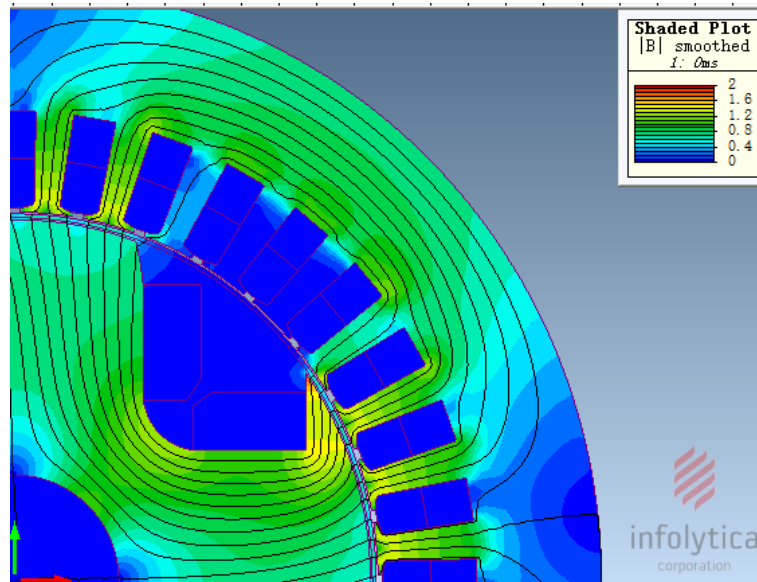
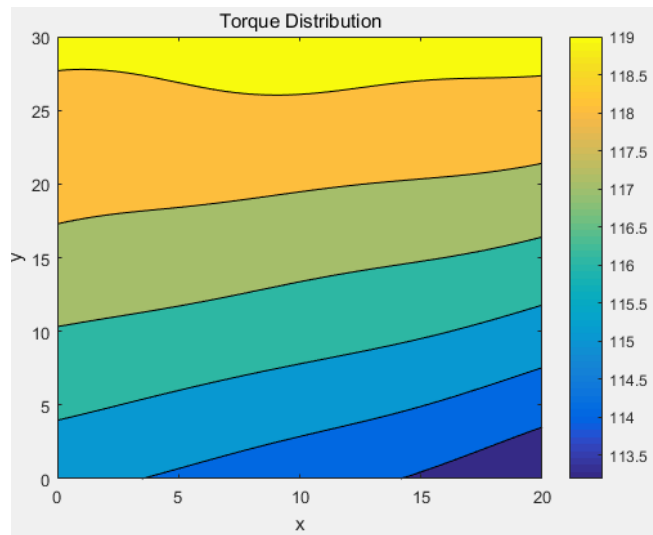


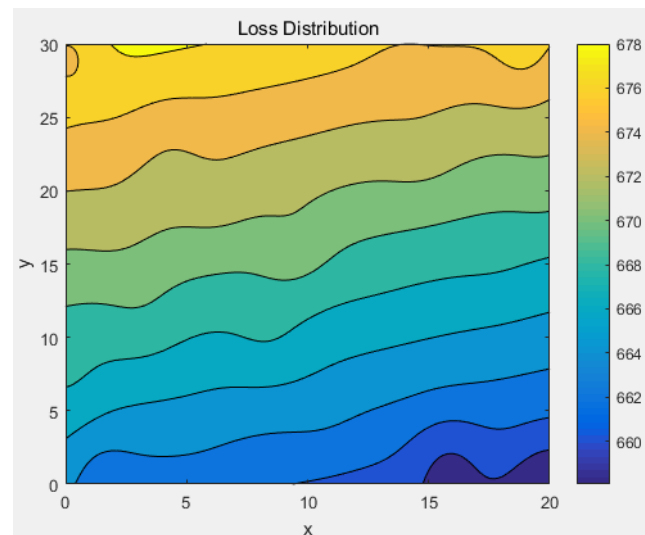
Fig. 70. Flux distribution and harmonic analysis.

By changing the winding configuration from a 1-slot, short-pitch configuration to 2/3 short-pitch configuration, the machine operates under different conditions. Because this winding configuration is the common choice of machine, the surrogate model of a 2/3 short-pitch winding configuration is simulated by figs.69-70.

Harmonic reductions were discussed in the previous chapter. However, torque reductions due to a short-pitch configuration are also apparent, as shown in Fig. 71. The loss distribution follows the same trend observed for the previous design.



(a)



(b)

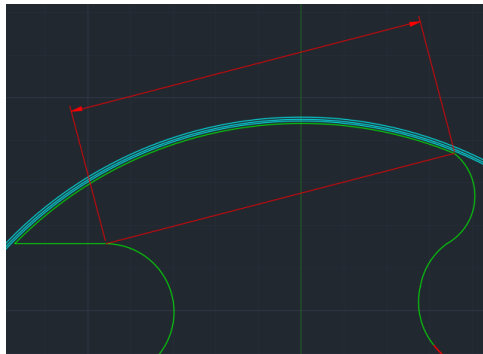
Fig. 71. Surrogate models of short-pitch configuration:  
(a) torque distribution and (b) loss distribution.

To conclude, these simulations show that by changing 2 variables, the performance will not be improved significantly. The torque improvement is less than 1%, and loss is reduced by less than 100 W. More variables should be incorporated to design a rotor shape that has a significant influence on machine performance.

### 6.2.3 Optimisation of plan B



(a)



(b)

Fig. 72. Asymmetrical rotor designs. (a) Original design. (b) Constraints.

As mentioned in section 6.1, plan B connects the pole body to the outer radius with an additional arc as shown in Fig.72. Therefore, the critical curvature (arc) of the rotor should be controlled by two variables as shown in Fig. 73.



Fig. 73. Definition of input parameters.

The low-sinusoidal induced voltage and low efficiency of asymmetrical machines should

be optimised in this design. Therefore, the efficiency is defined as one objective of the optimisation. The calculation of efficiency is carried by the following equation:

$$\eta = \frac{P_2}{P_2 + P_T} = \frac{P_2}{P_2 + P_k + P_a} \quad (57)$$

where

$P_2$  is the output power;

$P_T$  is the total power loss;

$P_a$  represents armature winding losses; and

$P_k$  represents constant losses, including friction and windage losses as well as iron losses.

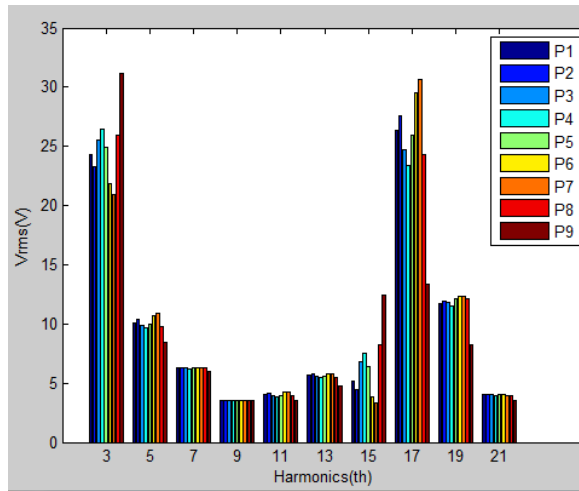


Fig. 74. Harmonic spectrum for evaluating power quality.

For inducing a sinusoidal voltage, harmonics of the voltage should be considered as another optimisation goal for the design. However, by a set of random combination (in Fig. 74), a prevalent 17<sup>th</sup> harmonic is founded in this rotor design. It is assumed to be directly linked to the parameters defined and is one of the major harmonic threat. Therefore, in addition to the commonly used THD, 17<sup>th</sup> harmonic is also chosen to be one of the optimisation goals.

## Simulation results

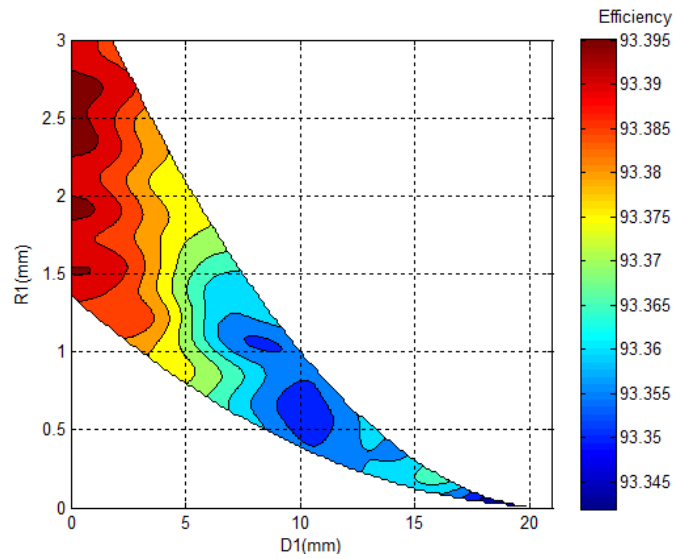


Fig. 75. Efficiency contour for D-R combination.

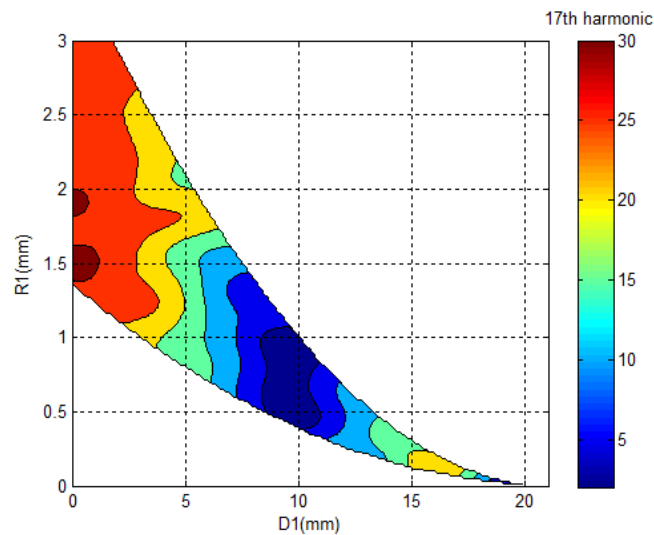


Fig. 76. Harmonic contour for D-R combination.

Fig. 75 illustrates the rotor optimisation function for efficiency with the corresponding 2-D variables (D-R combination). Fig. 76 shows the same 2-D variable optimisation function for the 17<sup>th</sup> harmonic.

These figures indicate two highly nonlinear test functions and two contradictory optimisation goals (high efficiency versus low harmonics). Therefore, it is very hard to locate one exact location of the optimised point in the design spaces manually. PSO

algorithm is conducted to make a compromise between the two objectives as shown in table.8.

Table. 8 Comparison between the original rotor and optimized rotor

	D (mm)	R (mm)	17 <sup>th</sup> Harmonic (V)	Efficiency
Original	21	0	27.85	93.374
Optimised	7.43	0.85	9.73	93.386

A sinusoidal voltage is achieved by reducing 65% major harmonic (17<sup>th</sup> harmonic) but retaining the same level (losing the only 3W for a 27.5KVA machine) of efficiency after optimisation.

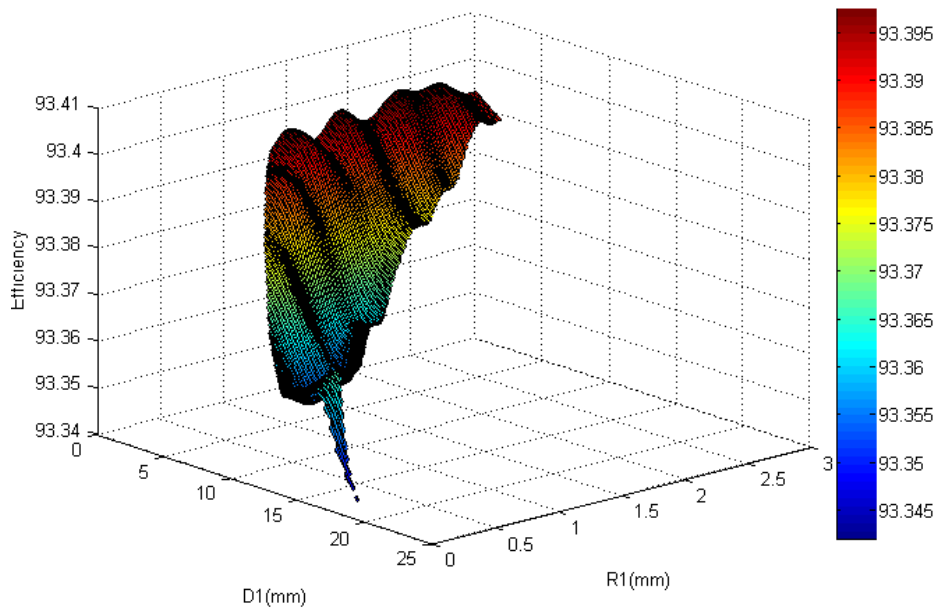


Fig. 77. Efficiency distribution for the D-R combination.

It can be easily observed that the proposed algorithm shows excellent performance in terms of speed and accuracy, as shown in Table.9.

The results of the surrogate optimisation are further confirmed by 2DFE simulation results built in Magnet software. Comparison of the rotors (before and after optimisation) is produced in Figs.78-80.

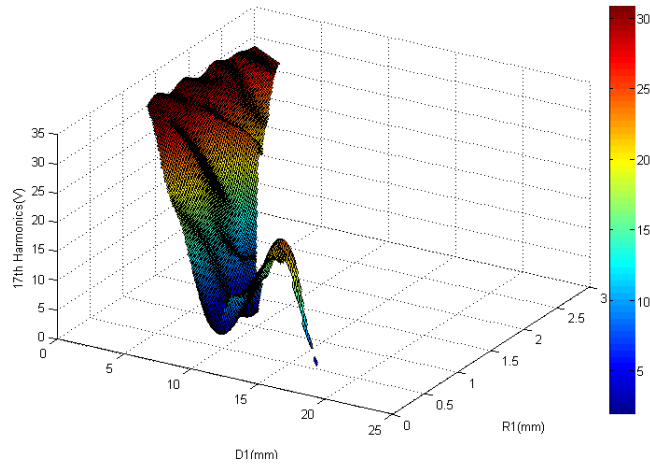


Fig. 78. Seventeenth harmonic distribution for D-R combination.

The results of FFT analysis show that the optimisation reduces the spatial harmonics, with the 17<sup>th</sup> harmonic and THD significantly reduced. The 17<sup>th</sup> harmonic is reduced by 65%, and the THD has been reduced by 10%.

Table. 9 Loss and efficiency of two synchronous generators

	17 <sup>th</sup> Harmonic (V)	Efficiency
Estimation	9.99	93.365
Numerical results	9.73	93.374
Relative error	2.6%	0.009%
Computation speed	5 mins	

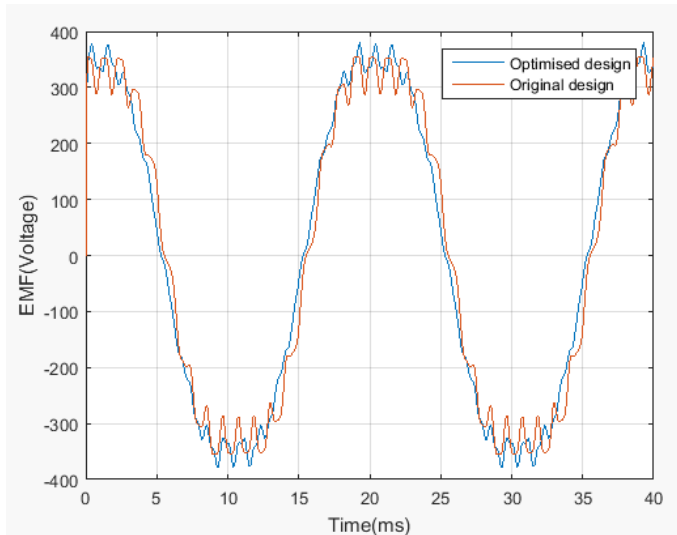


Fig. 79. Comparison of the no-load EMF voltages.

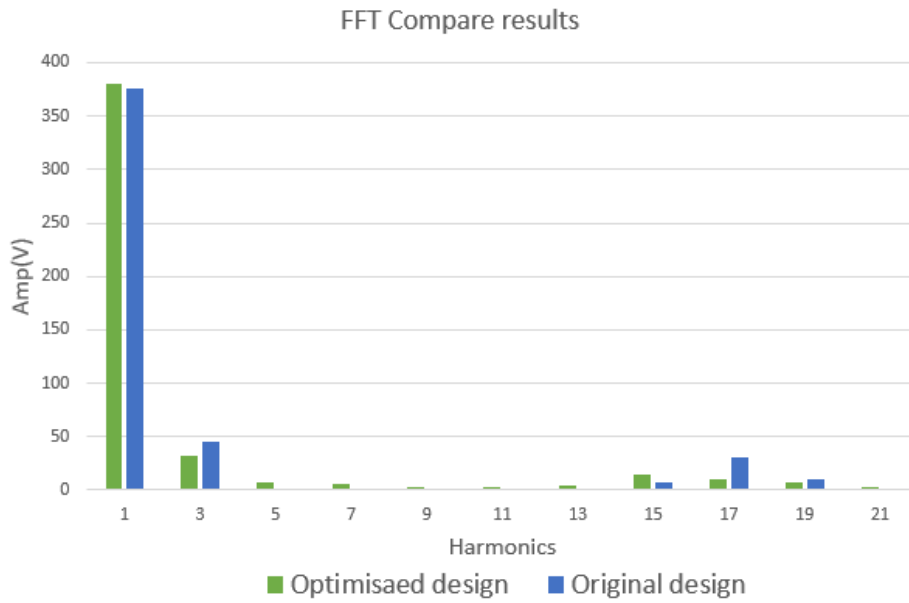


Fig. 80. Comparison of FFT results.

The flux has been guided away from the rotor teeth due to the change of rotor shape. This contributes to a low saturation level shown in Fig.81.

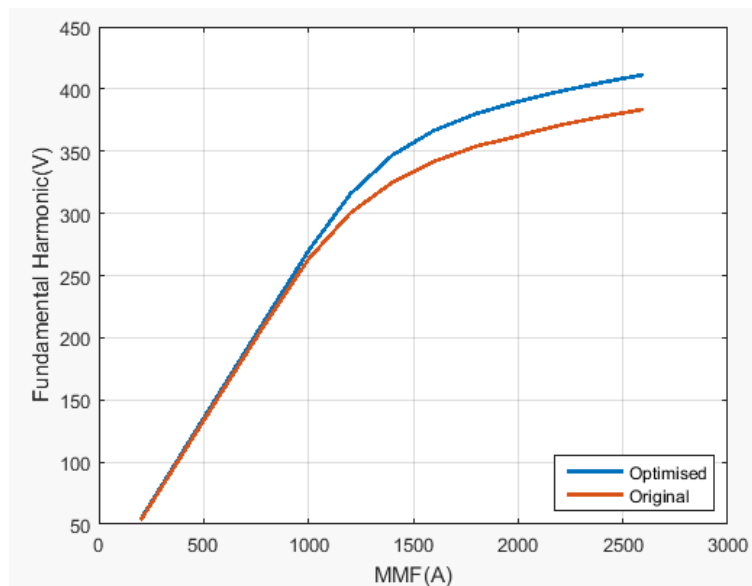


Fig. 81. No-load characteristics.

A higher torque is achieved by optimised machine, and its maximum power angle is changed which slightly changes the magnetic axis of the rotor as shown in Fig.82. However, this level of change is insignificant.

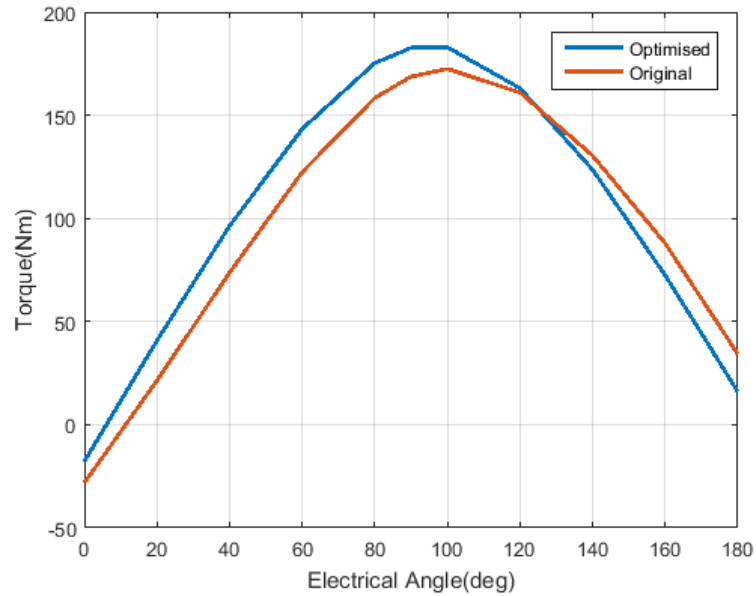


Fig. 82. Comparison of load tests.

To conclude, the optimisation plan B provide a valid surrogate optimisation for rotor geometry design. A sinusoidal induced voltage is achieved by not sacrificing too much efficiency. However, since the harmonic of the voltage can be reduced in other topology and power change is much more important in machine design, the further simulation will reconsider power output and efficiency as the goals.

### 6.3 4-D parameterization

Problem definition B of plan 1 is shown in Fig. 83. The principle of the plan is an extended version of problem definition A, which incorporates two more variables into the design space. These added variables are used to cut the tip side of the rotor to balance the flux distribution. The aim of the optimisation remains the same:

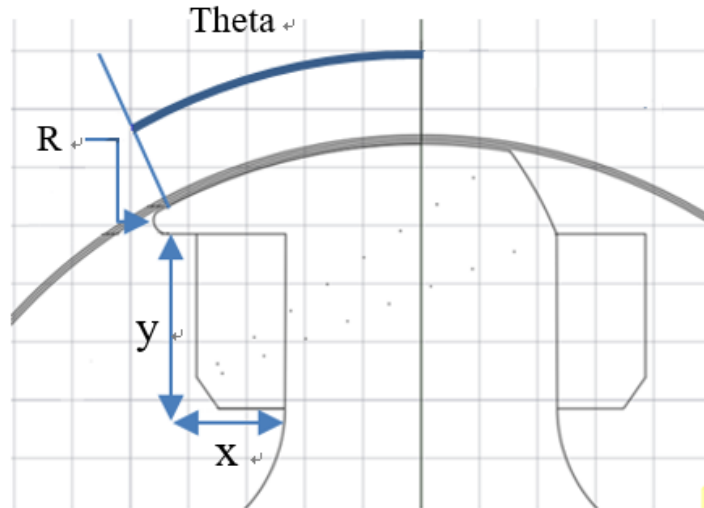


Fig. 83. Problem definition B of design plan 1.

Maximise: *Power output*

Minimise: *Loss*

Constraints:

$$0 < x < 20, 0 < y < 30, 2 < R < 10, 27 < \text{Theta} < 36$$

Problem definition C of plan 2 is shown in Fig. 84. This version is a slightly more complex than problem definition B. To balance the flux distribution, the arc side of the rotor tip is not completely removed. In addition, the left side of the rotor is cut with a circle. Two additional round circles are added to guide the flux into the rotor to avoid rectangular contact. As a result, this plan is a 4-variable optimisation plan similar to plan B. The optimisation goal is as follows:

Maximise: *Power output*

Minimise: *Loss*

Constraints:

$$0 < R1 < 6, 0 < R2 < 4, 0 < L1 < 6, 0 < R4 < 4$$

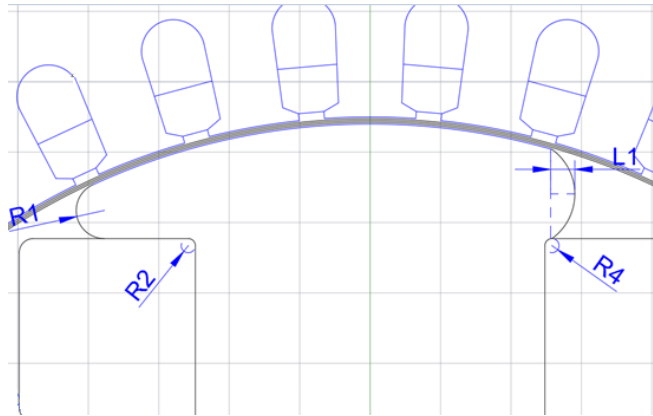
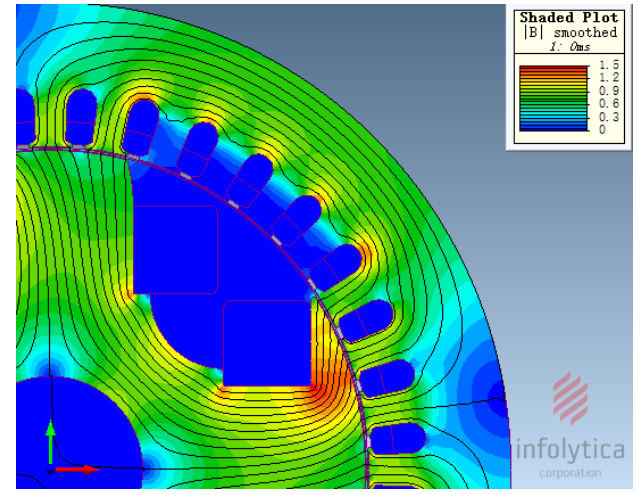
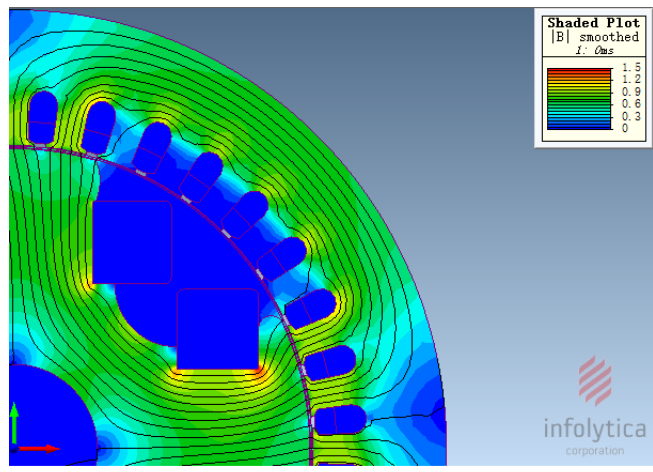


Fig. 84. Problem definition C of design plan 2.

### 6.3.1 Optimised plan simulation results



(a)



(b)

Fig. 85. Comparison of no-load flux densities of two plans.

As shown in Fig. 85, the flux paths of both designs are shifted towards the tip side of the

rotor due to the absence of a rotor tip. However, plan 2 clearly provides a better flux distribution. The flux concentration on the rotor tip is reduced by providing an extra flux path on the arc side. This extra flux path has a distinct effect on the induced EMF of the two plans. The results are shown in Fig. 86 and Table 10.

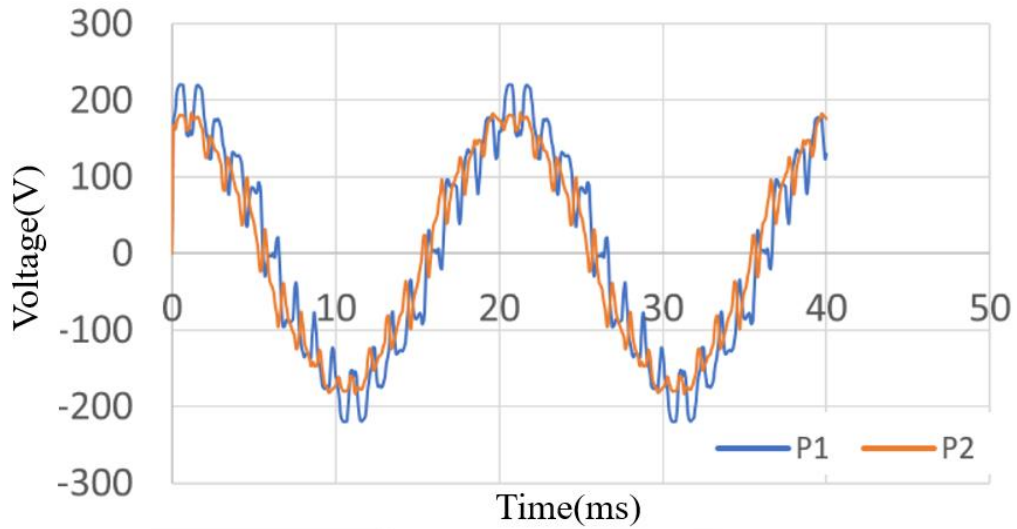


Fig. 86. Comparison of induced EMF of two plans

According to the FFT results shown in Table 10, the induced EMF is significantly distorted in plan 1, a clear reflection of the unbalanced flux path. However, in the second plan, because the flux is distributed evenly on both sides, the level of total harmonic distortion remains acceptable.

Table. 10 Harmonic analysis of two plans

Harmonics	P1 (V)	P2 (V)
1	184.61	173.29
3	0.03	0.04
5	9.26	7.08
7	1.91	4.17
9	0.12	0.18
11	0.70	2.85
13	4.26	1.87
15	0.05	0.05
17	34.78	7.92
19	0.50	16.13
THD	0.20	0.12

Another interesting aspect of the two designs is the saturation level. As indicated for the previous design, the saturation level should be carefully examined due to the high flux concentration on the rotor tip. Fig. 87 compares the 2 design plans and the original rotor plan.

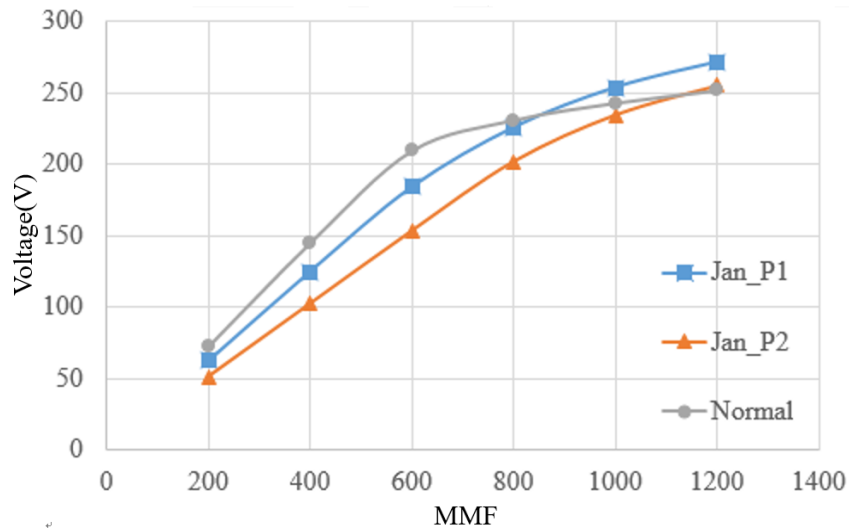


Fig. 87. Comparison of no-load characteristics.

The no-load characteristics show that neither plan 1 nor plan 2 is easy to saturate. However, the results also show that the plans would produce a relatively low voltage at a given excitation level. This feature can be attributed to the reduction in the flux paths due to the removal of the rotor tip. Interestingly, however, both plans can achieve higher voltages at the cost of a higher excitation level.

In general, the two plans operate similarly to a normal symmetrical rotor. The maximum power generated by the two plans can exceed that of the traditional symmetrical rotor. The maximum power angle shows interesting behaviour. As shown in Fig. 88, the maximum power angle is quite different between the 2 design plans, which corresponds to the unique shape of the rotor and its flux path.

As described above, the 2 design plans show different characteristics, and each presents its own merits and drawbacks. Therefore, it is very difficult to determine which one should be applied. Optimisation should be carried out to determine which of the 2 designs yields better performance.

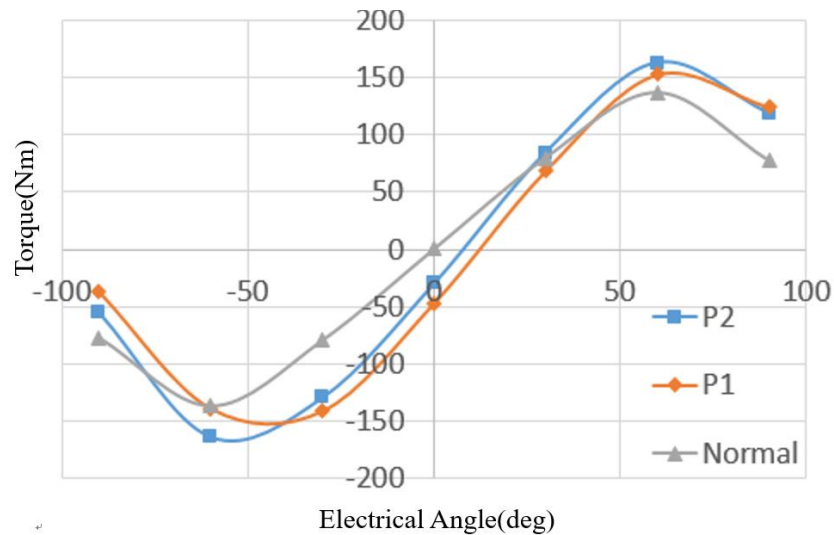


Fig. 88. Comparison of induced torque angle of two plans.

Because the advanced optimisation plans involve 4-variable optimisation, the results cannot be visualized by a 2-D figure. Following the same pattern, the details of the optimisation results are shown in Table 11 and Fig. 88.

Table. 11 Optimisation results of two plans

	Plan1	Plan2	Original design
X1	21.65	4	/
X2	24.72	1.33	
X3	2	2	
X4	27	2	
Torque (Surrogate)	154.68 Nm	163.54 Nm	162.5 Nm
Torque (FEA)	154.73 Nm	163.70 Nm	
Iron Loss (Surrogate)	424.3 W	462.5 W	544.4 W
Iron Loss (FEA)	422.9 W	462.48 W	

The accuracy of the surrogate model is confirmed by FEA simulation. According to the results, the two plans show similar iron losses. Both plans perform better in terms of loss

and torque production compared with the preliminary optimisation plan. However, compared with the original design, the torque provided by plan 1 is reduced. Therefore, plan 1 is not ideal for our optimisation goal. As a result, plan 2 is selected for experimental validation. The experimental validation of the simulation results is discussed in detail in the next chapter.

# Chapter 7 Validation of experiment

---

This chapter describes a set of experiments test for validate the FEA simulation results and compare the performance of optimised asymmetrical rotor with the conventional symmetrical rotor.

## 7.1 Test equipment

The test equipment used in these experiments are listed in Table.22 in the appendix.

## 7.2 Specifications of the original machine

The stator of the machine is a duplicate of a standard Cummins PI-144F machine.

The specifications provided by the manufacturer and photographs of the machine are provided in Fig. 97 (in the appendix) and Table 12.

Table. 12 Specifications of PI-144F

Item	Value	Item	Value
Rated Power (kVA)	27.5	Rated Speed (rpm)	1500
Rated Line Voltage (V)	380	Rated Frequency (Hz)	50
Rated Power Factor	0.8	Stack Length (mm)	200
Stator Slot Number	36	Pole Numbers	4
Stator OD (mm)	310	Stator ID (mm)	192
Rotor OD (mm)	188	Stator Winding Arrangement	Double-layer Star

## 7.3 Test procedure

The calculation of efficiency and its corresponding losses are shown as following:

Total loss = constant loss + load loss + excitation loss + additional load losses

$$P_T = P_k + P_S + P_{LL} + P_e$$

Constant loss = Friction losses + windage losses + iron losses

$$P_k = P_{fw} + P_{fe}$$

Excitation circuit losses = excitation winding losses + exciter losses + Brush losses

$$P_e = P_f + P_{Ed} + P_b$$

PS: For external, separately supplied system and for the synchronous machine only.

Exciter losses = power absorbed by the separate auxiliary winding + power absorbed by the exciter – excitation winding losses - separately supplied excitation power

Load losses = load winding losses

### 7.3.1 Test limitations

The equipment is chosen based on the following requirements based on British standards BS EN 60034-4:2008 and BS EN 60034-2-1:2007.

#### A. Voltage

Three-phase AC generators shall be suitable for supplying circuits that, when supplied by a system of balanced and sinusoidal voltages,

- a) Result in currents not exceeding a harmonic current factor (HCF) of 0.05.
- b) Result in a system of currents in which neither the negative-sequence component nor the zero-sequence component exceeds 5% of the positive-sequence component. The HCF shall be computed by using the following formula:

$$HCF = \sqrt{\sum_{n=2}^k i_n^2}$$

where

$i_n$  is the ratio of the harmonic current  $I_n$  to the rated current  $IN$ ;

$n$  is the harmonic order; and

$k = 13$ .

Should the limits of deformation and imbalance occur simultaneously in service at the rated load, this shall not lead to any harmful temperature in the generator, and it is recommended that the resulting excess temperature rise related to the limits specified in this standard should not exceed approximately 10 K.

## **B. Frequency**

The frequency shall be within 0.3% of the rated frequency during the experiment.

## **C. Resistance**

For a polyphase AC machine, resistance refers to the line-to-line resistance of the stator or armature winding. The test resistance at the end of the thermal test shall be determined as described for the extrapolation procedure, within the shortest time interval to avoid interference by thermal temperature.

## **D. Extrapolation method**

If a resistance reading cannot be done in the time interval specified in Table 12, it shall be made as soon as possible but not after more than twice the interval specified in Table 12, and additional readings shall be taken at intervals of approximately 1 min until these readings have begun a distinct decline from their maximum value.

Table. 13 Time interval after switching off

Rated output ( $P_N$ ) kW or kVA	Time interval after switching off power s
$P_N \leq 50$	30
$50 < P_N \leq 200$	90
$200 < P_N \leq 5000$	120
$5000 < P_N$	By agreement

A curve of these readings shall be plotted as a function of time and extrapolated to the appropriate time interval indicated in Table 12 for the rated output of the machine.

### 7.3.2 Direct measurement

#### A. Direct-current winding resistance measurements

The resistance is measured directly at the winding terminals with the rotor at rest at ambient temperature ( $27^\circ\text{C}$ ). Armature winding resistances are measured for each phase separately. In measuring the DC resistance of the armature or of the excitation winding by a voltmeter and ammeter, three readings are taken at various steady values of the current, as shown in Table 14.

Table. 14 Resistance measurement results

N.O.	Rotor winding (ohms)	Stator winding (line to neutral)
1	1.45	0.268
2	1.73	0.275
3	1.54	0.257
Average	1.57	0.267

#### B. Torque measurement

The torque transducer used in this experiment is a type JN-338 Series from SanJing United Technology Corporation, Beijing. This instrument has an accuracy of  $\pm 0.2\%$  at full scale (100 Nm). The torque signal generated by the torque transducer is a square-wave signal with a certain frequency, as shown in Fig. 90.

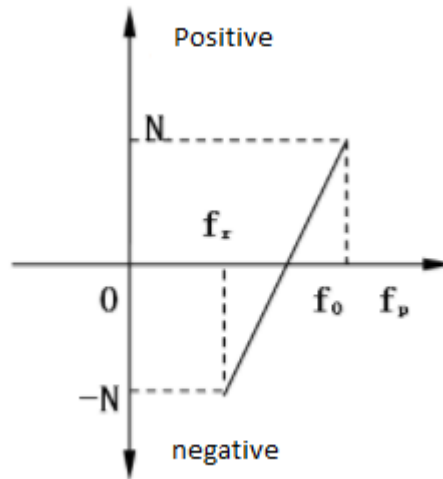


Fig. 89. Torque signal.

The amplitude of the measured torque is calculated by the following equations:

$$\begin{cases} M_p = N \frac{f - f_p}{f_p - f_0} \\ M_r = N \frac{f_r - f}{f_0 - f_r} \end{cases}$$

where  $f$  is the frequency of the torque signal,  $f_p$  is the positive torque frequency (15 kHz),  $f_0$  is the zero-point frequency (10 kHz),  $f_r$  is the negative torque frequency (5 kHz), and  $N$  is the full-scale torque amplitude (100 Nm in this case).

### C. Speed measurement

The speed signal is also a square wave similar to the torque signal. The frequency of the square-wave signal indicates the speed of the machine based on the following equation:

$$n = 60f / Z$$

where  $f$  is the frequency of the speed signal and  $Z$  is the number of teeth in the torque transducer. This number is 60 in the devices used in this study. Example of the torque and speed signals are shown in Fig. 91.

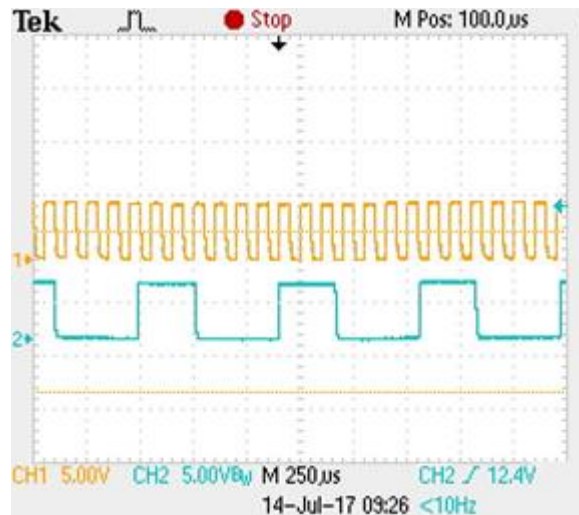


Fig. 90. Torque and speed signals measured by an oscilloscope.

### 7.3.3 Indirect measurement

Indirect measurements and their calculations are described in the following subsections.

#### A. Determination from the no-load test

A no-load saturation test is conducted while driving the test machine as a generator by a prime mover (DC motor, vector-controlled) at a rated frequency and voltage (by adjusting the excitation current) when operating as a generator and at a unity power factor (minimum current) when running as an uncoupled motor.

During the no-load test, excitation changes should be made in gradual steps from high voltage to low voltage using evenly distributed points. The voltage value should start with 1.3 times the rated voltage of the machine under test, and reduce gradually to 0.2 times the rated voltage unless the residual voltage is higher.

The following are recorded simultaneously:

- Excitation current;
- Line voltage;

– Frequency (or speed);

PS1: The resistance is measured after the voltage reading as stated in section 7.3.2.C.

PS2: For a coupled machine,  $P_0$  is determined from T and n.

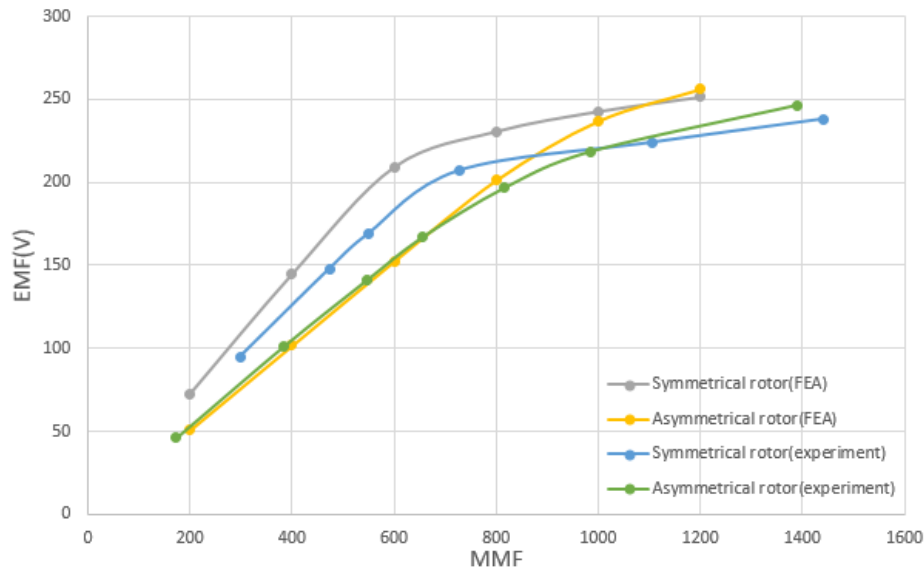


Fig. 91. Comparison of the results of the constant speed-variable excitation test.

The results of the no-load test can be founded in Table.22 in the appendix and shown in Fig.91. In comparing the results obtained for the symmetrical rotor, it is clear that the prediction of the FEA is lower than the experiment results by approximately 10%. The prediction of the asymmetrical rotor is quite close to the experimental result at a low excitation level, but the rotor reaches saturation faster than predicted. However, both no-load characteristics show that the asymmetrical rotor can perform similarly to the symmetrical rotor at the cost of a higher excitation level.

## B. Sustained three-phase short-circuit test (coupled)

A sustained three-phase short-circuit test is conducted by driving the test machine as a generator by a prime mover (DC motor, vector-controlled). A short circuit should be made as close to the machine terminals as possible, applying the excitation current after being

short-circuited. One of the readings is taken at a current close to the rated armature current to avoid interference from end-windings.

The excitation current and armature line current are recorded simultaneously. Speed variation is caused by the limit of prime-mover.

Table. 15 Sustained three-phase short-circuit test results

(a) Symmetrical rotor

Line current (A)	5	10.3	14.5	20	25.1	30
Excitation current (A)	4.4	9	12.6	17.1	21.6	26.8
Excitation voltage (V)	4.94	9.3	13.0	17.24	21.3	25.5
Speed (RPM)	1504	1489	1490	1488	1470	1400

(b) Asymmetrical rotor

Line current (A)	23.24	20.33	18.18	16.01	14.21	11.93	5.59	0.06
Excitation current (A)	19.8	17.85	16.15	14.14	12.34	10.31	5.06	0.01
Excitation voltage (V)	18.33	16.73	11.47	13.61	11.99	10.16	5.33	0
Speed (RPM)	1520	1502	1506	1511	1520	1506	1520	1515

The short-circuit current experiment shows that the optimized asymmetrical rotor provides a slightly higher short-circuit current than that of the symmetrical rotor. Apart from its effect on synchronous reactance and saliency, this high short-circuit current generally require better heat insulation when in a fault condition. However, the current is also very easy to detect, as the fault current is higher than the current of the symmetrical rotor.

### C. Zero-power factor over-excitation test

Inductive loads are the most common type of loads connected to the power system.

Therefore, a machine's response to such load changes is critical in terms of system stability.

The zero-power factor test is designed to compare the performance of the two abovementioned designs under normal generating conditions. The active power is equal to zero when the machine operates as a generator (i.e., pure inductive load).

During the test, the stator terminals are connected to a power analyser in parallel with an inductive load bank. The phase voltage and current are measured by the power analyser, and the excitation is measured by an ammeter at the output terminal of the rectifier.

Table. 16 Zero-power factor test results

(a) Symmetrical rotor

Inductance	L=44 mH	L=66 mH
Excitation current (A)	18.27	18.54
Stator voltage(V)	195	207.4
Reactive power (kVar)	2.92	2.30
Active power (W)	0.27	0.18
Power factor	0.03	0.02
Frequency	50.51	50.1
Stator current (A)	14.9	11.1

(b) Asymmetrical rotor

Inductance	L=44 mH	L=66 mH
Excitation current (A)	17.71	17.70
Stator voltage (V)	183	202.4
Reactive power (kVar)	2.53	2.09
Active power (W)	0.26	0.20
Power factor	0.04	0.07
Frequency	49.92	49.7
Stator current (A)	13.8	10.03

Due to the limitations of the excitation device, the stator voltage cannot return to its rated value when connected to an inductive load bank. The asymmetrical rotor clearly shows a larger voltage drop than the symmetrical rotor does under the same excitation. According to the active power, the rotor has a relatively lower reactive power compared with that of

the symmetrical rotor. However, these differences remain acceptable. Overall, the performance of the asymmetrical design doesn't show too much difference to that of the symmetrical design in reactive power.

#### **D. Resistive load bank test**

The resistive load test involves the same settings as the inductive load test. The resistive load test is designed to determine the active power output capability of generators. As observed for the inductive load test, the asymmetrical rotor performs similarly to the symmetrical design but still shows lower active power generation.

Table. 17 Resistive load test results  
(a) Symmetrical rotor before excitation adjustment

Load (kW)	4.33	7.45	8.7
Terminal voltage (V)	216.8	200.1	178.0
Stator current (A)	6.6	12.3	16.3
Excitation current (A)	12.32	12.12	12.07
Excitation voltage (V)	12.01	11.88	11.82

(b) Symmetrical rotor after excitation adjustment

Load (kW)	4.88	8.17	12.9
Terminal voltage (V)	220	223.7	215.4
Stator current (A)	7.2	13.8	19.8
Excitation current (A)	14.53	11.71	16.0
Excitation Voltage (V)	15.4	12.88	15.4

(c) Asymmetrical rotor

	Before	After	Before	After
Load (kW)	3.99	4.27	7.45	8.26
Terminal voltage (V)	215.5	223.2	203	220.3
Stator current (A)	6.5	6.7	12.2	12.5
Excitation current (A)	12.37	13.10	12.21	13.35
Excitation voltage (V)	12.7	13.34	12.64	13.82

However, the rotation of the asymmetrical rotor is quite unstable in the high-active-load condition. The noise and vibration of the asymmetrical rotor severely affect the performance of the machine. The reason is partly due to the inappropriate balancing technology used in the manufacture of the rotor. Because the rotor itself is asymmetrical, the balancing of the rotor should be treated carefully. Another possible reason is that the traditional plain bearing (bushing) used in this machine is heavily pressured due to the rotor's asymmetry. Therefore, a rolling ball bearing should be used in these tests.

### **E. Run down test**

A self-deceleration test is used to test the inertia of the rotor and losses. During the test, the machine is connected to a prime mover with an external excitation system. The test machine is accelerated to 110% of the rated speed before the power of the prime mover is cut off, and the test machine decelerates. The time required for the machine to decelerate from 110% of the rated speed to 90% of the rated speed is recorded under the following conditions:

- a) The stator winding is open-circuited, the excitation is cut off, and the time is recorded as  $\Delta t_1$ .

b) The stator winding is open-circuited, the rated excitation is supplied by an external source, and the time is recorded as  $\Delta t_2$ .

c) The stator winding is short-circuited, the rated excitation is supplied by an external source, and the time is recorded as  $\Delta t_3$ .

d) The stator winding is connected to a load with known losses, the rated excitation is supplied by an external source, and the time is recorded as  $\Delta t_4$ .

## **F. Low-slip test**

A rotor should be driven by a prime mover at a slip of less than 0.01, and for solid-rotor machines, the slip should be much lower than that value so that the currents induced in the damper circuits during synchronous operation will have a negligible effect on the measurements. A subnormal symmetrical three-phase voltage (0.01 to 0.2 of nominal voltage) is applied to the armature terminals of the machine under test (that the machine does not pull in must be ensured). The excitation winding shall be open-circuited during measurement.

The following values are recorded:

-Armature current and voltage; and

-Speed

The voltage and current of the source are measured by a power analyser. Simulation results are presented in Fig. 92. Experimental validation results are shown in Fig. 93.

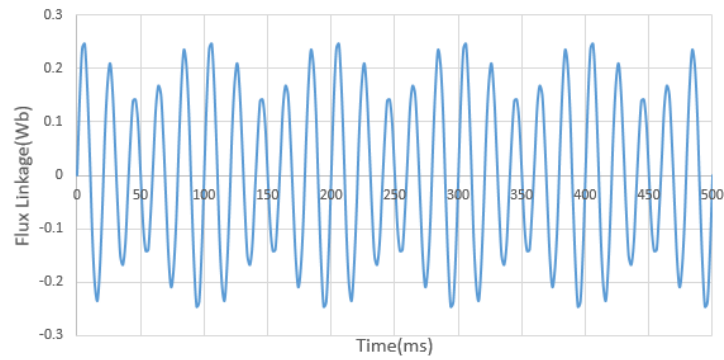
The saliency of the rotor caused by the transformation of the rotor geometry is

confirmed by experimental results. This change in saliency affects the torque output of the alternator. Based on the equations reported in [20], the output torque at any speed can be derived as follows:

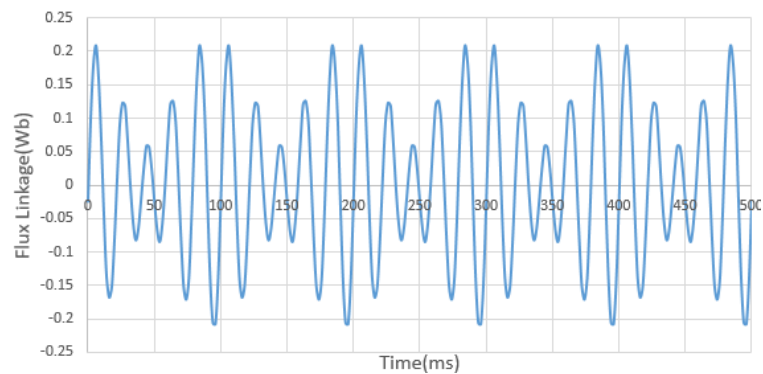
$$T = X_{ad} I_f I_s \cos \gamma - \frac{1}{2} (X_d - X_q) I_s^2 \sin 2\gamma$$

$X_d$ ,  $X_{ad}$  = per unit direct axis synchronous and magnetizing reactance at one per unit speed;

$X_q$  = per unit quadrature axis reactance at one per unit speed.



a



b

Fig. 92. Simulated low-slip test results (FEA results)  
(a) Symmetrical. (b) Asymmetrical.

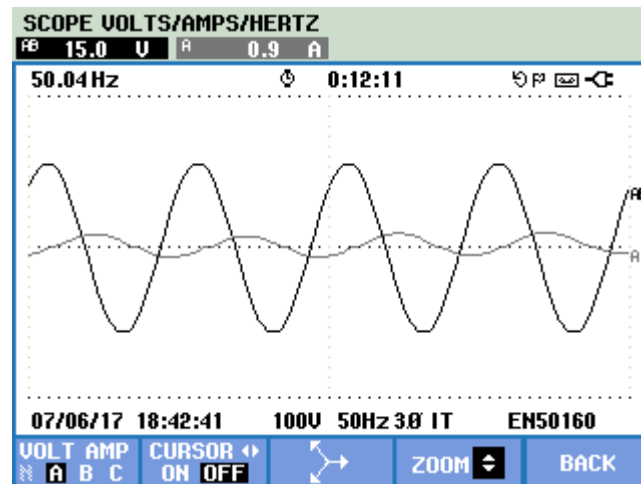


Fig. 93. Low-slip test results (experimental results).

With  $V_s$  defined as the stator voltage and  $I_s$  as the phase current, the first component of the equation can be considered the stator-rotor field interaction. The second part is the reluctance torque caused by the saliency of the rotor. This latter part is significantly increased in the asymmetrical design, leading to the higher power output shown in the optimisation results.

## 7.4 Harmonic analysis

Based on the test described in section 2.4.1.1, the voltage waveform can be easily obtained from an oscilloscope. In this analysis, FFT technology is applied to the waveform for harmonic analysis. The results are compared with FEM results for confirmation.

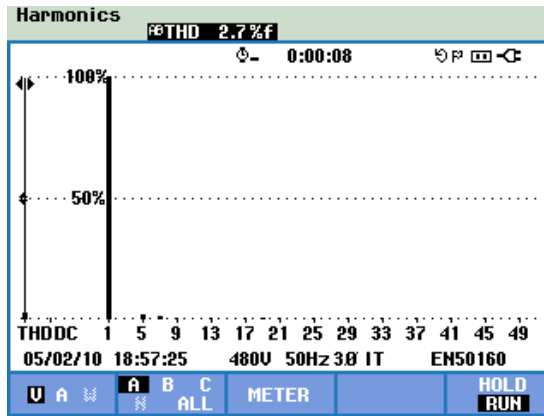


Fig. 94. FFT analysis of symmetrical rotor no-load voltage waveform calculated by power analyser.

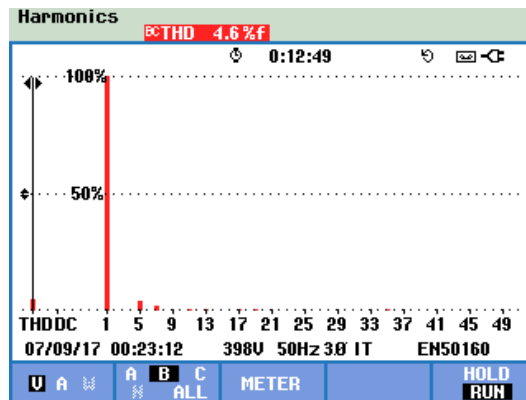


Fig. 95. FFT analysis of asymmetrical rotor no-load voltage waveform calculated by power analyser.

Table. 18 FFT results of FEM analysis and experimental validation

	Symmetrical rotor	Asymmetrical rotor
1	231.14	217.98
3	1.05	2.45
5	3.41	1.42
7	3.61	3.93
9	0.14	2.02
11	0.21	2.00
13	1.85	1.62
15	0.03	2.25
17	1.59	0.67
19	3.27	6.87
21	0.31	1.26
THD (FEA)	2.82%	4.31%
THD (EXP)	2.7%	4.6%

## 7.5 Determination of efficiency

The loss and efficiency of each rotor are calculated in this section.

### 7.5.1 Determination from direct measurement (self-deceleration test)

The time gaps of the four tests mentioned in section 7.3.4.E are shown in Table 19.

Table. 19 Self-deceleration test results

	Symmetrical	Asymmetrical
$\Delta t_1$	7.79	6.95
$\Delta t_2$	6.82	5.98
$\Delta t_3$	4.20	4.26
$\Delta t_4$	3.2	3.03

The inertia of the rotors is calculated as follows:

$$J = \frac{P}{10.97n_N \left( \frac{\Delta n}{\Delta t_4} - \frac{\Delta n}{\Delta t_2} \right)} \times 10^6$$

where P is the power of the load banks connected to the machine. In the corresponding experiment, P=4.5 KW.

Therefore, the inertias of the two rotors are calculated as

$$J_{sy} = \frac{P}{10.97n_N \left( \frac{\Delta n}{\Delta t_4} - \frac{\Delta n}{\Delta t_2} \right)} \times 10^6 = \frac{4.5kW}{10.97(1500rpm) \left( \frac{0.2*1500rpm}{\Delta t_4} - \frac{0.2*1500rpm}{\Delta t_2} \right)} = 4571.76kg \cdot m^2$$

$$J_{asy} = \frac{P}{10.97n_N \left( \frac{\Delta n}{\Delta t_4} - \frac{\Delta n}{\Delta t_2} \right)} \times 10^6 = \frac{4.5kW}{10.97(1500rpm) \left( \frac{0.2*1500rpm}{\Delta t_4} - \frac{0.2*1500rpm}{\Delta t_2} \right)} = 5648kg \cdot m^2$$

In this case, the mechanical losses, constant losses, and total losses are calculated as follows:

$$P_{fN} = 10.97Jn_N \frac{\Delta n}{\Delta t_1} \times 10^{-6}$$

$$P_0 = 10.97 J n_N \frac{\Delta n}{\Delta t_2} \times 10^{-6}$$

$$P_{total} = P_{cua} + P_d + P_{fN} = 10.97 J n_N \frac{\Delta n}{\Delta t_3} \times 10^{-6}$$

The results are shown in Table 20.

Table. 20 Iron loss results obtained by direct measurement

	Symmetrical	Asymmetrical
Mechanical losses	2898	3780
Constant losses	3309	4242
Total losses	5425	6074
Iron losses	411	462

These losses gained from the run-down test is used as a reference to the indirect measurement since the accuracy of the test is severally limited by the time measurement.

## 7.5.2 Determination from indirect measurement

Indirect measurements and their corresponding calculations are discussed in this section.

### A. Friction and windage losses $P_{fw}$

Based on the no-load test points, it is shown that no significant saturation effect occurs, and a curve of constant losses ( $P_k$ ) against voltage squared ( $U_0^2$ ) is developed. A straight line is extrapolated to zero voltage. The intercept with the zero-voltage axis represents the friction and windage losses  $P_{fw}$ .

The experimental results are slightly lower than the FEA results. This discrepancy is partly due to the fact that the material characteristics incorporated into the simulation are inaccurate relative to those of the actual material used in the experiment. However, it is still confirmed that the loss of the asymmetrical rotor can reach the same level observed for the symmetrical rotor, and the overall design performs significantly better than the

original design.

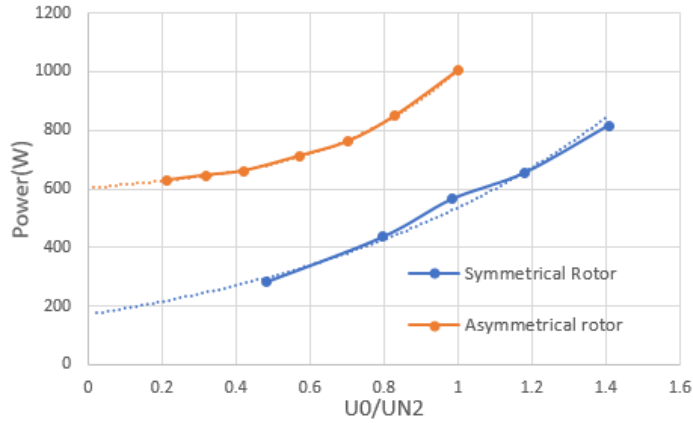


Fig. 96. Loss-voltage curve

Table. 21 Loss analysis of designs

	Symmetrical rotor	Asymmetrical rotor	Original asymmetrical design
Iron Loss (Exp)	408	407	493
Iron Loss (FEA)	470	463	544
Iron Loss (Exp-Deceleration)	411	462	/

Attention should be paid to the friction and windage losses of the asymmetrical rotor, which are greater than those of the symmetrical rotor. The unbalanced shape of the asymmetrical rotor makes for larger vibrations, increasing the mechanical loss of the machine. Therefore, the alignment of the shaft and the fixing of the frame should be specially designed.

In this case, the friction and windage losses of the symmetrical rotor ( $P_{sfw}$ ) are calculated to be 171.68 W, whereas those of the asymmetrical rotor ( $P_{asfw}$ ) is calculated to be 600.96 W.

## B. Iron losses $P_{fe}$

For each of the voltage values (see section 7.3.4.A), a curve of constant losses against voltage is plotted. The windage and friction losses are then subtracted from the curve to determine the iron losses.

$$P_{fe} = P_k - P_{fw}$$

- The iron losses for the symmetrical rotor are calculated to be  $535.94 - 171.68 = 364.26$  W.
- The iron losses for the asymmetrical rotor are calculated to be  $1006.65 - 600.96 = 399.69$  W.

The results are compared with those of the self-deceleration test (section 7.3.4.E); the results indicate that the iron losses are reasonably close. The difference of the error is caused by the lack of accuracy in the time measurement of the run-down test.

The iron loss of the asymmetrical rotor is slightly higher than that of the symmetrical rotor, but the loss does not significantly influence the performance of the machine. However, the balance of the asymmetrical rotor must be carefully addressed due to the large mechanical losses caused by vibration.

## C. Excitation circuit losses $P_e$

In the case of separately excited synchronous machines, the excitation winding losses  $P_f$  are the

the product of  $U_e, I_e$ , minus by the brush losses  $P_b$ .

## D. Brush losses $P_b$

Brush losses are determined based on the assigned voltage drop per brush for each polarity:

$$P_b = 2 \times U_b \times I_e$$

where

$I_e$  is determined according to the load test described in section 7.3.4.C

$U_b$  is the voltage drop per brush for each polarity depending on brush type as following

1.0 V for carbon (used in the test), electro-graphitic carbon or graphite and 0.3 V for metal-carbon

- Therefore, the excitation loss can be calculated as follows:

$$P_e = P_f + P_b = U_e I_e + 2U_b I_b$$

- According to the test described in section 2.4.1.1,

$$P_e = U_e I_e + 2U_b I_e = 12.56 \times 12.55 + 2 \times 1 \times 12.56 = 182.728W$$

## E. Load losses $P_s$

At each of the load points, the stator-winding losses are determined as follows:

$$P_s = 1.5 \times I^2 \times R_{ll,0}$$

where

$R_{ll}$  is determined as described in section 7.3.2.C, corrected to 25°C, the primary reference coolant temperature.

$$P_s = 1.5 \times 38^2 \times 0.27 = 584.82W$$

## F. Efficiency

The comparison of three rotors (original asymmetrical rotor, optimised asymmetrical rotor,

commercial symmetrical rotor) is shown in Table. 23.

Table. 22 Efficiency Table

	Commercial symmetrical rotor	Original asymmetrical design	Optimised Asymmetrical rotor
Friction and windage loss	200 W	600 W	600W
Iron Loss	408 W	493 W	407 W
Excitation circuit loss	183 W	183 W	183 W
Load loss	585 W	585 W	585 W
Efficiency	95%	93.24%	93.55%

The results show that the iron loss has been restored into the same level of the commercial symmetrical rotor after optimisation. However, the efficiency hasn't been improved significantly due to the friction and windage losses. The mechanical design of the rotor should be considered in the future studies.

## 7.6 Summary

The results obtained from simulation and experimental tests on both the original rotor design and the optimized design are analysed in this chapter. The experimental results verify the finite element predictions. The two rotors are compared under the same experimental conditions with the same method.

The no-load test compares the iron, friction and windage losses of the two machines. It is observed that the asymmetrical rotor achieves lower iron loss than does the symmetrical design. However, another method should be implemented to reduce the corresponding friction and windage losses caused by the asymmetrical shape of the rotor. A load test compares the performance of the two machines under different load conditions. The results indicate that the asymmetrical rotor shows similar but slightly worse performance

compared with the traditional design.

Overall, it is fair to conclude that the asymmetrical rotor shows essentially the same performance as the traditional rotor with the added feature of easy insertion of the rotor windings.

# Chapter 8 Conclusion

---

The major results of this thesis are concluded in this chapter. Studies of rotor geometry design in wound-rotor synchronous machines and the application of a surrogate optimisation method have been the focus of this thesis. This chapter also provides suggestions for future work.

## 8.1 Conclusions

This thesis is organised as follows.

Literature related to synchronous machines is reviewed in Chapter 2. The reviewed studies show that synchronous machines are still considered the most common choice for electric power generation, including in diesel/gas/steam turbines in heat power plants, large hydro-machines in hydro plants, and wind turbines in wind farms. Despite the variety of such machines, they are still irreplaceable due to their high reliability in harsh operational environments.

Although traditional wound-rotor synchronous machines have been used for many years, their design methods have been heavily modified in recent decades with the development of computer-aided analysis software and corresponding numerical optimisation methods. However, computational costs (both time and economic) also increase significantly with these technologies.

One major issue associated with the manufacture of wound-rotor synchronous machines is the rotor winding process, which is considered to be labour-intensive, as the windings

are not pre-designed and must be wrapped around the rotor pole. The advantages and disadvantages of two alternative methods are discussed. The results indicate that a new winding method would be helpful not only for new machines but also for the rewind of machines.

Chapter 3 presents a new asymmetrical rotor shape for wound-rotor synchronous machines. The rotor pole is asymmetrical, effectively shifting the magnetic field to the leading edges. As a result, the output power is increased due to the change in saliency. This design allows for the field windings to be easily installed on the rotor, thus simplifying machine assembly and repair procedures.

The results of a 2-D simulation FEA and experiment are discussed based on a 27.5-kVA prototype. Overall, the asymmetrical rotor can achieve performance similar to that of the symmetrical rotor if the shape is optimised to improve its power profile.

In Chapter 4, in addition to the analysis of the original asymmetrical rotor design, tests are carried out to examine the key factors influencing the performance of the machine. The components of both the stator and rotor are included in the studies. Simplified analytical calculations are performed to confirm the test results via FEA.

In Chapter 5, a new method for surrogate optimisation is introduced. A finite element-based surrogate optimisation method is performed to determine which rotor geometry factors are related to power output and loss. In this procedure, surrogate models are constructed based on finite element results obtained from sampling points selected by the design of the experiment. Then, optimisation is carried out on the surrogate models instead of the finite element models. Since the surrogate model is constructed based on the test

results, the time cost of the optimisation can be controlled by controlling the test results used in constructing surrogate models.

Latin hyperspace sampling is selected to minimise the computational time required and maximise the information acquired from a trade-off between the number of selected points and the amount of information. The sampling points are used to build surrogate models of the synchronous machines with the assistance of Kriging models to estimate the response of the function in an unknown design area. Errors in the estimation are measured to correct the surrogate model and improve its accuracy. Particle swarm optimisation is then applied to the surrogate models to find the best solution.

In Chapter 6, specific optimisation plans are examined and carried out with different designs. Asymmetrical rotor optimisation focuses on presenting the critical curvature of the rotor geometry by varying parameters, investigating the effect of rotor shaping methods by surrogate models and optimizing the rotor-pole shape for high-efficiency output.

Through the design of the rotor's geometry, the machine is optimised to achieve a high-efficiency power output and still maintain its easy installation feature. The effect of rotor shaping is verified by FEA simulations and experiments. FEA results indicate that the new rotor shape can achieve the same performance as that of the traditional rotor after optimisation, with the benefit of easier rotor installation.

The original and optimised rotors are manufactured and tested based on the IEEE standard under the same conditions in chapter 8. No-load tests are used to determine the iron, friction and windage losses of the machines. Loaded tests measure the asymmetrical

rotor's performance under different operating conditions. The experimental results are confirmed by FEA, validating the accuracy of the simulation.

This work demonstrates that an asymmetrical rotor can improve the rotor winding installation and repair process of a synchronous machine. This asymmetrical rotor design improves the installation process of the rotor coils by not separating the rotor poles. Therefore, the mechanical integrity of the rotor pole is maintained, and the ageing problem is solved. It also improves the maintenance cost in the power system and increases the cost efficiency.

The electromagnetic performance of the machine can be optimised to reach the same level observed for a traditional rotor. It is also proved that the combination of surrogate optimisation and finite element methods can reduce the time cost of the optimisation process and address the design of the rotor's complex geometry.

## **8.2 Future work**

Some limitations are concluded from the asymmetrical design shown as following:

- The machine is designed to operate uni-directionally, and is not very suitable for bi-directional operation conditions such as electric vehicles.
- The mechanical performance of the asymmetrical rotor is worse than that of the symmetrical rotor.

A few areas are open for further investigation and exploration in addition to the work presented in this thesis:

- Further research can address the mechanical force of the asymmetrical rotor design to reduce the relatively large friction and windage losses observed experimentally.
- The surrogate optimisation can be applied to various objectives and constraints, such as torque ripple and power density.
- Further experimental tests can be performed on the power system to confirm the stability of the asymmetrical machine due to its unique saliency.

# Reference

- [1] M. A. Lamoureux, "Electricity Production and Greenhouse Gas Emissions," in *IEEE Power Engineering Review*, vol. 22, no. 11, pp. 22-24, Nov. 2002.
- [2] Department for Business, energy& Industrial Strategy, "Energy Trends: Renewables," [https://www.gov.uk/government/uploads/system/uploads/attachment\\_data/file/604105/Renewables.pdf](https://www.gov.uk/government/uploads/system/uploads/attachment_data/file/604105/Renewables.pdf) accessed May 2017
- [3] Department for Business, energy& Industrial Strategy, "Energy Trends: electricity,". <https://www.gov.uk/government/statistics/electricity-section-5-energy-trends> accessed May 2017
- [4] K. Sedlazeck *et al.*, "Type testing a 2000 MW turbogenerator," *2009 IEEE International Electric Machines and Drives Conference*, Miami, FL, 2009, pp. 465-470. doi: 10.1109/IEMDC.2009.5075247
- [5] H. Hooshyar, M. Savaghebi and A. Vahedi, "Synchronous generator: past, present and future," *AFRICON 2007, Windhoek*, 2007, pp. 1-7.
- [6] G. Neidhofer, "The evolution of the synchronous machine," *Engineering Science and Education Journal*, pp. 239-248, October 1992.
- [7] R. Weddleton, A. Sismour, "Turbine generator rotor turn insulation-class F," *Conference Record of the IEEE International Symposium on Electrical Insulation*, June 1992.
- [8] T. Jianzhong, W. Jianhe, "Nomex paper T-411 impregnated with adhesive varnish and its application," *IEE Proc. of Int. Symposium on Electrical Insulating Materials*, September 1998.
- [9] K. W. Cowan, A. J. Main, "The development of a new range of hydrogen-cooled generators," *IEEE Trans. Electrical machines and drives*, pp. 378-384, September 1995.
- [10] S. H. Park *et al.*, "Characteristics of Rotating Armature Type High-Temperature Superconducting Generators with Dual Field Windings for the Wind Turbine," in *IEEE Transactions on Applied Superconductivity*, vol. 25, no. 3, pp. 1-5, June 2015.
- [11] T. Hoshino, I. Muta, T. Itoh, K. Hayashi and E. Mukai, "Preliminary study on a rotating armature type superconducting motor," in *IEEE Transactions on Magnetics*, vol. 30, no. 4, pp. 2026-2029, July 1994.
- [12] R. L. Stoll and A. Hennache, "Method of detecting and modelling presence of shorted turns in DC field winding of cylindrical rotor synchronous machines using two airgap search coils," in *IEEE Proceedings B - Electric Power Applications*, vol. 135, no. 6, pp. 281-294, November 1988.
- [13] K. Boughrara, R. Ibtouen and O. Touhami, "Exact analytical prediction of the magnetic field in a hybrid and wound excitation synchronous machine," *2012 XXth International Conference on Electrical Machines*, Marseille, 2012, pp. 2818-2824.
- [14] J. P. McSharry, P. S. Hamer, D. Morrison, J. Nessa and J. G. Rigsby, "Design, fabrication, back-to-back test of 14200-hp two-pole cylindrical-rotor synchronous motor for ASD application," in *IEEE Transactions on Industry Applications*, vol. 34,

no. 3, pp. 526-533, May/Jun 1998.

- [15] K. Hruska, V. Kindl, R. Pechanek and P. Svetlik, "Design possibilities of multiple-pole cylindrical rotor synchronous machine excitation winding," *IECON 2014 - 40th Annual Conference of the IEEE Industrial Electronics Society*, Dallas, TX, 2014, pp. 490-496.
- [16] K. Hruska, V. Kindl and R. Pechanek, "The issues of multiple-pole cylindrical rotor synchronous machine excitation winding," *2013 15th European Conference on Power Electronics and Applications (EPE)*, Lille, 2013, pp. 1-10.
- [17] Zhao W, Chen D, Lipo TA, Kwon B-I: 'Performance Improvement of Ferrite-Assisted Synchronous Reluctance Machines Using Asymmetrical Rotor Configurations', *IEEE Transactions on Magnetics.*, 2015, 51, (11), pp. 1–4
- [18] Vartanian R, Toliyat HA.: 'Design and comparison of an optimized permanent magnet-assisted synchronous reluctance motor (PMA-SynRM) with an induction motor with identical NEMA Frame stators'. in 2009 IEEE Electric Ship Technologies Symposium, 2009, pp. 107–112.
- [19] Prieto D, Dagusé B, Dessante P, Vidal P, Vannier J-C.: 'Effect of magnets on average torque and power factor of synchronous reluctance motors ', *Electrical Machines (ICEM), 2012 XXth International Conference on*; 2012: IEEE.
- [20] Liu W, Lipo TA.: 'On saliency enhancement of salient pole wound field synchronous machines', *Energy Conversion Congress and Exposition (ECCE), 2016 IEEE*; 2016: IEEE.
- [21] Zhu Z, Zhou Y, Chen J, Green JE.: 'Investigation of Nonoverlapping Stator Wound-Field Synchronous Machines', *IEEE Transactions on Energy Conversion.*, 2015, 30, (4), pp. 1420–7
- [22] Liu H-C, Jeong G, Ham S-h, Lee J.: 'Optimal rotor structure design of claw-pole alternator for performance improving using static 3D FEM coupled-circuit model', *Electromagnetic Field Computation (CEFC), 2016 IEEE Conference on*; 2016: IEEE.
- [23] Li G, Ojeda J, Hlioui S, Hoang E, Lecrivain M, Gabsi M.: 'Modification in rotor pole geometry of mutually coupled switched reluctance machine for torque ripple mitigating', *IEEE Transactions on Magnetics.*, 2012, 48, (6), pp. 2025–34
- [24] Harianto CA, Sudhoff SD.: 'A rotationally asymmetric reluctance machine with improved torque density', *IEEE Transactions on Energy Conversion.*, 2013, 28, (1), pp. 62–75
- [25] Zhao W, Lipo TA, Kwon B-I.: 'Optimal design of a novel asymmetrical rotor structure to obtain torque and efficiency improvement in surface inset PM motors', *IEEE Transactions on Magnetics.*, 2015, 51, (3), pp. 1–4
- [26] Chitroju R, Sadarangani C.: 'Phase shift method for radial magnetic force analysis in induction motors with non-skewed asymmetrical rotor slots', *Electric Machines and Drives Conference, 2009 IEMDC'09 IEEE International*; 2009: IEEE.
- [27] H. Aspden, UK Patent GB2303255A, "magnetic reluctance motor," 1997.
- [28] R. Garg, *Analytical and computational methods in electromagnetics / Ramesh Garg*. Norwood, Mass. :: Artech House, 2008.
- [29] C. C. Chan and K. T. Chau, "Computer graphics-aided design for an advanced

- electrical motor,” *Comput. Aid. Eng. Journal*, vol. 7, pp. 72- 74, Jun. 1990.
- [30] T. W. Preston and J. P. Sturgess, “Implementation of the finite-element method into machine design procedures,” in *Proc. Intl. Conf. Electric Machines and Drives*, 1993, pp. 312-317.
- [31] V. Ostović, *Dynamics of Saturated Electric Machines*. New York:Springer-Verlag, 1989.
- [32] P. Sewell, K. J. Bradley, J. C. Clare, P. W. Wheeler, A. Ferrah, and R. Magill, “Efficient dynamic models for induction machines,” *Intl. J. Numer. Model.*, vol. 12, pp. 449-464, 1999.
- [33] J. Perho, “Reluctance network for analysing induction machines,” *Acta Polytechnica Scandinavica, Electrical Engineering Series*, vol. 110, pp. 1-147, Dec. 2002.
- [34] S. D. Sudhoff, B. T. Kuhn, K. A. Corzine and B. T. Branecky, “Magnetic Equivalent Circuit Modeling of Induction Motors,” in *IEEE Transactions on Energy Conversion*, vol. 22, no. 2, pp. 259-270, June 2007.
- [35] H. Meshgin-Kelk, J. Milimonfared, and H. A. Toliyat, “A comprehensive method for the calculation of inductance coefficients of cage induction machines,” *IEEE Trans. Energy Conversion*, vol. 18, pp. 187-193, Jun. 2003.
- [36] J. D. Law, T. J. Busch, and T. A. Lipo, “Magnetic circuit modelling of the field regulated reluctance machine. Part I: model development,” *IEEE Trans. Energy Conversion*, vol. 11, pp. 49-55, Mar. 1996.
- [37] M. Amrhein and P. T. Krein, “Magnetic Equivalent Circuit Simulations of Electrical Machines for Design Purposes,” *2007 IEEE Electric Ship Technologies Symposium*, Arlington, VA, 2007, pp. 254-260.
- [38] A. Spargo, S. Ilie and J. Chan, “Salient-pole rotor optimisations for synchronous generators using FEA software,” *2017 IEEE Workshop on Electrical Machines Design, Control and Diagnosis (WEMDCD)*, Nottingham, 2017, pp. 158-162.
- [39] Smith, T., Jones, M.: 'Modeling of salient-pole wound-rotor synchronous machines for population-based design', *IEEE Transactions on Energy Conversion.*, 2011, 26, (2), pp. 381–92
- [40] O. Laldin, S. D. Sudhoff and S. Pekarek, “An Analytical Design Model for Wound Rotor Synchronous Machines,” in *IEEE Transactions on Energy Conversion*, vol. 30, no. 4, pp. 1299-1309, Dec. 2015.
- [41] A. Rambetius, S. Luthardt, B. Piepenbreier, “Modeling of wound rotor synchronous machines considering harmonics geometric saliencies and saturation induced saliencies”, *Proc. IEEE Int. Power Elect. Conf.*, pp. 3029-3036, 2014.
- [42] M. M. Rahimian, K. Butler-Purry, “Modeling of synchronous machines with damper windings for condition monitoring”, *Proc. IEEE Int. Elect. Mach. Drives Conf.*, pp. 577-584, May 2009.
- [43] F. Kieferndorf, H. Burzanowska, S. Kanerva, P. Sario, “Modeling of rotor based harmonics in dual-star wound field synchronous machines”, *Proc. IEEE Int. Conf. Elect. Mach.*, pp. 1-6, Sep. 2008.

- [44] M. J. Soleimani Keshayeh and S. Asghar Gholamian, "Optimum Design of a Three-Phase Permanent Magnet Synchronous Motor for industrial applications," *International Journal of Applied Operational Research - An Open Access Journal*, vol. 3, no. 1, pp. 0–0, Jan. 2013.
- [45] N. Bianchi and M. Dai Pre, "Use of the star of slots in designing fractional-slot single-layer synchronous motors," in *IEE Proceedings - Electric Power Applications*, vol. 153, no. 3, pp. 459-466, 1 May 2006.
- [46] A. S. Abdel-Khalik, S. Ahmed and A. Massoud, "A new permanent-magnet vernier machine using a single layer winding layout for electric vehicles," *2014 IEEE 23rd International Symposium on Industrial Electronics (ISIE)*, Istanbul, 2014, pp. 703-708.
- [47] C. J. Ifedi, "A high torque density, direct drive in-wheel motor for electric vehicles," Ph.D., School of Electrical and Electronic Engineering, Newcastle University, 2013.
- [48] Jha, Rajesh & Dulikravich, George & Colaco, Marcelo & Fan, Min & , J.Shawartz & Koch, C.C, " Magnetic Alloys Design Using Multi-Objective Optimisation," *ACEX2015-9th International Conference on Advanced Computational Engineering and Experimenting*, Munich, 2015
- [49] Javier, M.; Jaime, G.; Ernesto, S., " Non-Destructive Techniques Based on Eddy Current Testing. Sensors " , *Sensors*, 2011,vol 11, pp. 2525-2565.
- [50] A. Krings, S. Nategh, A. Stening, H. Grop, O. Wallmark, and J. Soulard, "Measurement and modelling of iron losses in electrical machines," in *5th International Conference Magnetism and Metallurgy WMM'12, June 20th to 22nd, 2012, Ghent, Belgium*, 2012, pp. 101-119.
- [51] I. Magnet. "Iron Loss Calculations in Laminated Structures". Available: [www.infolytica.com/en/applications/ex0166/](http://www.infolytica.com/en/applications/ex0166/)
- [52] Advaced MotorTech, LLC, " Short course on the design of interior permanent magnet and brushless DC machines — Taking theory to practice", May 2010.
- [53] Pyrhonen, J., T. Jokien, and V. Hrabovcova, " Design of Rotating Electrical Machines", John Wiely & Sons, Ltd., 2008.
- [54] Emadi, A., *Energy-efficient Electric Motors*, 3rd Edition, Marcel Dekker, Inc., New York, 2005.
- [55] Proxi. *SLIP RINGS*. Available: <https://powerbyproxi.com/slip-ring/>
- [56] Suzhou Firstall Electrical machine&technology.co.LTD. *Alternator Brushless Generator Head 10kw*. Available: <http://www.fadianjidl.com/soqux/hq805.html>
- [57] Sang Bin Lee, Gerald Kliman, Manoj Shah, Dongwook Kim, Tony Mall, Kutty Nair, and Mark Lusted. " Experimental study of inter-laminar core fault detection techniques based on low flux core excitation ". *In Proc. IEEE SDEMPED '05* pages 163–171, Vienna, Austria, Sep 2005.
- [58] Peter J. Tavner and James Penman. " Condition Monitoring of Electrical Machines. " , *Research Studies Press Ltd, John Wiley & Sons Inc.*, Chichester, West Sussex, England, 1987.
- [59] Daley JM, Siciliano RL.: 'Application of emergency and standby generation for distributed generation. I. Concepts and hypotheses', *IEEE Transactions on Industry*

- Applications, 2003, 39, (4), pp. 1214–25
- [60] Hassan I, Weronick R, Bucci R, Busch W.: 'Evaluating the transient performance of standby diesel-generator units by simulation', *IEEE Transactions on Energy Conversion.*, 1992, 7, (3), pp. 470–7
- [61] J, Tindall C, Morrow DJ.: 'Synchronous machine parameter determination using the sudden short-circuit axis currents', *IEEE Transactions on Energy Conversion.*, 1999, 14, (3), pp. 454–9
- [62] Stone GC, Culbert I, Boulter EA, Dhirani H.: 'Salient Pole Rotor Winding Failure Mechanisms and Repair. Electrical Insulation for Rotating Machines: Design, Evaluation, Aging, Testing, and Repair', 253-63
- [63] IEEE Std 1068-2015 (Revision of IEEE Std 1068-2009): 'IEEE Standard for the Repair and Rewinding of AC Electric Motors in the Petroleum, Chemical, and Process Industries', 2006
- [64] Rotating electrical machines - Part 4: Methods for determining synchronous machine quantities from tests, *BSI British Standards BS EN 60034-4*: 2008.
- [65] Liu W, Lipo TA.: 'On saliency enhancement of salient pole wound field synchronous machines', *Energy Conversion Congress and Exposition (ECCE)*, 2016 IEEE; 2016: IEEE.
- [66] S. A. Evans, "Salient pole shoe shapes of interior permanent magnet synchronous machines," *The XIX International Conference on Electrical Machines - ICEM 2010*, Rome, 2010, pp. 1-6.
- [67] J. Pyrhönen, T. Jokinen and V. Hrabovcova, *Design of Rotating Electrical Machines*, John Wiley & Sons, Ltd., Chichester, 2008, p. 165.
- [68] I. Boldea, Synchronous Generators, *The Electric Generators Handbook*, CRC Press, Taylor & Francis, Boca Raton, 2006, p. 7–28.
- [69] K. T. Chau, C. C. Chan, and C. Liu, "Overview of Permanent-Magnet Brushless Drives for Electric and Hybrid Electric Vehicles," *IEEE Transactions on Industrial Electronics*, vol. 55, no. 6, pp. 2246–2257, Jun. 2008.
- [70] S. R. MacMinn and W. D. Jones, "A very high-speed switched-reluctance starter-generator for aircraft engine applications," in *Proceedings of the IEEE National Aerospace and Electronics Conference*, 1989, pp. 1758–1764 vol.4.
- [71] E.S. Hamdi, "*Design of Small Electrical Machines*," Chichester, John Wiley & Sons, 1998.
- [72] G.Veinott, "*Theory and Design of Small Induction Motors*," New York: McGraw-Hill, 1959.
- [73] M. Yilmaz and P. T. Krein, "Capabilities of finite element analysis and magnetic equivalent circuits for electrical machine analysis and design," in *2008 IEEE Power Electronics Specialists Conference*, 2008, pp. 4027–4033.
- [74] P. Silvester and M. V. K. Chari, "Finite Element Solution of Saturable Magnetic Field Problems," *IEEE Transactions on Power Apparatus and Systems*, vol. PAS-89, no. 7, pp. 1642–1651, Sep. 1970.

- [75] T. W. Preston and J. P. Sturgess, "Implementation of the finite-element method into machine design procedures," in *1993 Sixth International Conference on Electrical Machines and Drives (Conf. Publ. No. 376)*, 1993, pp. 312–317.
- [76] D. Lim, Y. Jin, Y.-S. Ong, and B. Sendhoff, "Generalizing surrogate-assisted evolutionary computation," *IEEE Trans. Evol. Comput.*, vol. 14, no. 3, pp. 329–355, Jun. 2010.
- [77] L.-K. Lim, D.-K. Woo, I.-W. Kim, J.-S. Ro, and H.-K. Jung, "Cogging torque minimization of a dual-type axial-flux permanent magnet motor using a novel optimisation algorithm," *IEEE Trans. Magn.*, vol. 49, no. 9, pp. 5106–5111, Sep. 2013.
- [78] I. W. Kim *et al.*, "Minimization of a cogging torque for an interior permanent magnet synchronous machine using a novel hybrid optimisation algorithm," *J. Elect. Eng. Technol.*, vol. 8, no. 3, pp. 742–748, May 2014.
- [79] E. R. Lwithwaite, "Magnetic equivalent circuits for electrical machines," *Proceedings of the Institution of Electrical Engineers*, vol. 114, no. 11, pp. 1805–1809, Nov. 1967.
- [80] C. J. Carpenter, "Magnetic equivalent circuits," *Proceedings of the Institution of Electrical Engineers*, vol. 115, no. 10, pp. 1503–1511, Oct. 1968.
- [81] V. OSTOVIĆ, "Magnetic Equivalent Circuit Presentation of Electric Machines," *Electric Machines & Power Systems*, vol. 12, no. 6, pp. 407–432, Jan. 1987.
- [82] M. Yilmaz and P. T. Krein, "Capabilities of finite element analysis and magnetic equivalent circuits for electrical machine analysis and design," in *2008 IEEE Power Electronics Specialists Conference*, 2008, pp. 4027–4033.
- [83] Y. Duan and D. M. Ionel, "A Review of Recent Developments in Electrical Machine Design Optimisation Methods With a Permanent-Magnet Synchronous Motor Benchmark Study," *IEEE Transactions on Industry Applications*, vol. 49, no. 3, pp. 1268–1275, May 2013.
- [84] A. J. Booker, J. E. Dennis Jr, P. D. Frank, D. B. Serafini, and V. Torczon, "Optimisation using surrogate objectives on a helicopter test example," in *Computational Methods for Optimal Design and Control*, ed: Springer, 1998, pp. 49-58.
- [85] M. M. Rai and N. K. Madavan, "Aerodynamic design using neural networks," *AIAA Journal*, vol. 38, pp. 173-182, 2000.
- [86] M. M. Rai, N. K. Madavan, and F. W. Huber, "Improving the unsteady aerodynamic performance of transonic turbines using neural networks," 2000.
- [87] N. K. Madavan, M. M. Rai, and F. W. Huber, *Neural net-based redesign of transonic turbines for improved unsteady aerodynamic performance*: National Aeronautics and Space Administration, Ames Research Center, 1998.
- [88] B. Xia, Z. Ren, K. Choi, and C. S. Koh, "A Novel Subregion-Based Multidimensional Optimisation of Electromagnetic Devices Assisted by Kriging Surrogate Model," *IEEE Transactions on Magnetics*, vol. 53, no. 6, pp. 1–4, Jun. 2017.

- [89] S. Koziel and S. Ogurtsov, "Design optimisation of microstrip antenna arrays using surrogate-based methodology," in *2013 IEEE Antennas and Propagation Society International Symposium (APSURSI)*, 2013, pp. 1228–1229.
- [90] X. Song *et al.*, "Surrogate-Based Analysis and Optimisation for the Design of Heat Sinks With Jet Impingement," *IEEE Transactions on Components, Packaging and Manufacturing Technology*, vol. 4, no. 3, pp. 429–437, Mar. 2014.
- [91] W. Shyy, N. Papila, P. K. Tucker, R. Vaidyanathan, and L. Griffin, "Global Optimisation for Fluid Machinery Applications," in *Proceedings of the second international symposium on fluid machinery and fluid engineering (ISFMFE)*, Beijing, China, 2000.
- [92] W. Shyy, N. Papila, R. Vaidyanathan, and K. Tucker, "Global design optimisation for aerodynamics and rocket propulsion components," *Progress in Aerospace Sciences*, vol. 37, pp. 59-118, 2001.
- [93] R. Vaidyanathan, P. K. Tucker, N. Papila, and W. Shyy, "Computational-fluid-dynamics-based design optimisation for single-element rocket injector," *Journal of propulsion and power*, vol. 20, pp. 705-717, 2004.
- [94] R. Vaidyanathan, T. Goel, W. Shyy, R. T. Haftka, N. V. Queipo, and P. K. Tucker, "Global sensitivity and trade-off analyses for multi-objective liquid rocket injector design," in *Proceedings of the 40th AIAA/ASME/SAE/ASEE joint propulsion conference and exhibit*, Fort Lauderdale, FL, 2004.
- [95] Z. Tan, X. Song, W. Cao, Z. Liu, and Y. Tong, "DFIG Machine Design for Maximizing Power Output Based on Surrogate Optimisation Algorithm," *IEEE Transactions on Energy Conversion*, vol. 30, no. 3, pp. 1154–1162, Sep. 2015.
- [96] Yoon, Keunyoung, and B. Kwon. "Efficiency Improvement for Concentrated Flux IPM Motors for Washing Machines." *Journal of Electrical Engineering & Technology* 9.4(2014):1277-1282.
- [97] Zheng Tan, "Improved Winding Design of a Doubly Fed Induction Generator (DFIG) Wind Turbine using Surrogate Optimisation Algorithm," PhD dissertation, School of Electrical and Electronic Engineering., Newcastle University, Newcastle, UK, 2015.
- [98] N. V. Queipo, R. T. Haftka, W. Shyy, T. Goel, R. Vaidyanathan, and P. Kevin Tucker, "Surrogate-based analysis and optimisation," *Progress in Aerospace Sciences*, vol. 41, pp. 1-28, 1// 2005.
- [99] Giunta, A.A., Wojtkiewicz, S.F., Eldred, M.S.: Overview of modern design of experiments methods for computational simulations. American Institute of Aeronautics and Astronautics, paper AIAA 2003–0649 (2003)
- [100] Santner, T.J., Williams, B., Notz, W.: The Design and Analysis of Computer Experiments. Springer, Heidelberg (2003)
- [101] Koehler, J.R., Owen, A.B.: Computer Experiments. In: Ghosh, S., Rao, C.R. (eds.) Handbook of Statistics, vol. 13, pp. 261–308. Elsevier Science B.V., Amsterdam (1996)
- [102] Z.-H. Han and K.-S. Zhang. Surrogate-Based Optimisation. Technical report, School of Aeronautics, Northwestern Polytechnical University, Xian, P.R. China, 2012

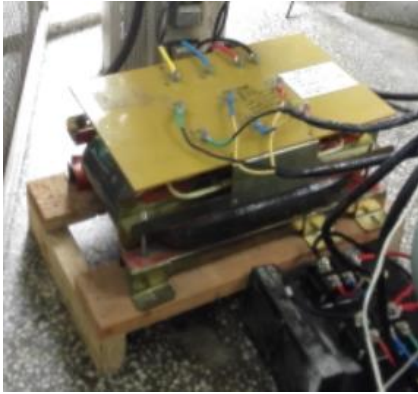
- [103] S. Koziel and X.-S. Yang, *Computational optimisation, methods and algorithms* vol. 356: Springer Science & Business Media, 2011.
- [104] Baalousha H. Using orthogonal array sampling to cope with uncertainty in groundwater problems[J]. *Groundwater*, 2009, 47(5): 709-713.
- [105] McKay, M. D., Beckman, R. J., and Conover, W. J., A Comparison of Three Methods for Selecting Values of Input Variables in the Analysis of Output from a Computer Code, *Technometrics*, Vol. 21, No. 2, 1979, pp. 239-245.
- [106] M. Stein, "Large sample properties of simulations using Latin hypercube sampling," *Technometrics*, vol. 29, pp. 143-151, 1987.
- [107] Alexander I.J. Forrester, Andy J. Keane, Recent advances in surrogate-based optimisation, *Progress in Aerospace Sciences*, vol. 45, pp. 50-79, June. 2010.
- [108] S. M. Wild, R. G. Regis, and C. A. Shoemaker, "ORBIT: Optimisation by radial basis function interpolation in trust-regions," *SIAM Journal on Scientific Computing*, vol. 30, pp. 3197-3219, 2008.
- [109] T. W. Simpson, J. D. Poplinski, P. N. Koch, and J. K. Allen, "Metamodels for computer-based engineering design: survey and recommendations," *Engineering with Computers*, vol. 17, pp. 129-150, 2001.
- [110] J. P. C. Kleijnen, "Kriging metamodeling in simulation: A review," *European Journal of Operational Research*, vol. 192, pp. 707-716, 2009.
- [111] A. G. Journé and C. J. Huijbregts, *Mining Geostatistics*: Blackburn Press, 2003.
- [112] A. O'Hagan and J. F. C. Kingman, "Curve fitting and optimal design for prediction," *Journal of the Royal Statistical Society. Series B (Methodological)*, pp. 1-42, 1978.
- [113] M. J. Sasena, "Flexibility and efficiency enhancements for constrained global design optimisation with kriging approximations," General Motors, 2002.
- [114] Z. Tan, X. Song, W. Cao, Z. Liu, and Y. Tong, "DFIG machine design for maximizing power output based on surrogate optimisation algorithm," *IEEE Trans. Energy Conversion*, Vol. 30, No. 3, pp. 1154-1162, Sep. 2015.
- [115] J. P. Costa, L. Pronzato, and E. Thierry, "A comparison between Kriging and radial basis function networks for nonlinear prediction," in *NSIP*, 1999, pp. 726-730.
- [116] P. Chandrashekarappa and R. DuVigneau, "Radial basis functions and kriging metamodels for aerodynamic optimisation," 2007.
- [117] T. Goel, R. Vaidyanathan, R. T. Haftka, W. Shyy, N. V. Queipo, and K. Tucker, "Response surface approximation of Pareto optimal front in multi-objective optimisation," *Computer methods in applied mechanics and engineering*, vol. 196, pp. 879-893, 2007.
- [118] Y. Mack, T. Goel, W. Shyy, R. T. Haftka, and N. V. Queipo, "Multiple surrogates for the shape optimisation of bluff body-facilitated mixing," in *Proceedings of the 43rd AIAA aerospace sciences meeting and exhibit*, Reno, NV, 2005, pp. 2005-0333.
- [119] T. Goel, Y. Mack, R. T. Haftka, W. Shyy, and N. V. Queipo, "Interaction between grid and design space refinement for bluff body-facilitated mixing," in *Proceedings of the 43rd AIAA aerospace sciences meeting and exhibit*, Reno, NV, 2005, pp. 2005-0125.

- [120] Z. Bayraktar, J. Bossard, X. Wang, and D. H. Werner, "A real-valued parallel clonal selection algorithm and its application to the design optimisation of multi-layered frequency selective surfaces," *Antennas and Propagation, IEEE Transactions on*, vol. 60, pp. 1831-1843, 2012.
- [121] J. Yao, N. Kharma, and P. Grogono, "Bi-objective multipopulation genetic algorithm for multimodal function optimisation," *Evolutionary Computation, IEEE Transactions on*, vol. 14, pp. 80-102, 2010.
- [122] X. Li and X. Yao, "Cooperatively coevolving particle swarms for large scale optimisation," *Evolutionary Computation, IEEE Transactions on*, vol. 16, pp. 210-224, 2012.
- [123] B.-Y. Qu, P. N. Suganthan, and J.-J. Liang, "Differential evolution with neighborhood mutation for multimodal optimisation," *Evolutionary Computation, IEEE Transactions on*, vol. 16, pp. 601-614, 2012.
- [124] C. Stoean, M. Preuss, R. Stoean, and D. Dumitrescu, "Multimodal optimisation by means of a topological species conservation algorithm," *Evolutionary Computation, IEEE Transactions on*, vol. 14, pp. 842-864, 2010.
- [125] X. Li, "Niching without niching parameters: particle swarm optimisation using a ring topology," *Evolutionary Computation, IEEE Transactions on*, vol. 14, pp. 150-169, 2010.
- [126] Y. Duan and R. G. Harley, "A Novel Method for Multiobjective Design and Optimisation of Three-Phase Induction Machines," *IEEE Transactions on Industry Applications*, vol. 47, no. 4, pp. 1707-1715, Jul. 2011.
- [127] N. Bianchi and S. Bolognani, "Design optimisation of electric motors by genetic algorithms," *IEE Proceedings-Electric Power Applications*, vol. 145, pp. 475-483, 1998.
- [128] Y. Duan, R. G. Harley, and T. G. Habetler, "A useful multi-objective optimisation design method for PM motors considering nonlinear material properties," in *Energy Conversion Congress and Exposition, 2009. ECCE 2009. IEEE*, 2009, pp. 187-193.
- [129] G. Pellegrino and F. Cupertino, "FEA-based multi-objective optimisation of IPM motor design including rotor losses," in *Energy Conversion Congress and Exposition (ECCE), 2010 IEEE*, 2010, pp. 3659-3666.
- [130] R. Wrobel and P. H. Mellor, "Particle swarm optimisation for the design of brushless permanent magnet machines," in *Industry Applications Conference, 2006. 41st IAS Annual Meeting. Conference Record of the 2006 IEEE*, 2006, pp. 1891-1897.
- [131] R. Poli, J. Kennedy, and T. Blackwell, "Particle swarm optimisation," *Swarm Intelligence*, vol. 1, no. 1, pp. 33-57, Jun. 2007.
- [132] K. Salah, "A generic model order reduction technique based on Particle Swarm Optimisation (PSO) algorithm," *IEEE EUROCON 2017 -17th International Conference on Smart Technologies*, Ohrid, Macedonia, 2017, pp. 193-196.
- [133] T. Mesbahi, N. Rizoug, P. Bartholomeüs, R. Sadoun, F. Khenfri and P. Le Moigne, "Optimal Energy Management for a Li-Ion Battery/Supercapacitor Hybrid Energy Storage System Based on a Particle Swarm Optimisation Incorporating Nelder-

- Mead Simplex Approach,” in *IEEE Transactions on Intelligent Vehicles*, vol. 2, no. 2, pp. 99-110, June 2017.
- [134] N. Mizuno and C. H. Nguyen, “Parameters identification of robot manipulator based on particle swarm optimisation,” *2017 13th IEEE International Conference on Control & Automation (ICCA)*, Ohrid, Macedonia, 2017, pp. 307-312.
- [135] B. Wang; X. Zheng; S. Zhou; C. Zhou; X. Wei; Q. Zhang; Z. Wei, “Constructing DNA Barcode Sets based on Particle Swarm Optimisation,” in *IEEE/ACM Transactions on Computational Biology and Bioinformatics*, vol. PP, no.99, pp.1-1
- [136] A. Sahu, K. Kiran and S. Das, “Particle Swarm Optimisation based tuning of brushless doubly-fed reluctance machine drive for speed control applications,” *2016 IEEE 1st International Conference on Power Electronics, Intelligent Control and Energy Systems (ICPEICES)*, Delhi, 2016, pp. 1-6.
- [137] J. Song, F. Dong, J. Zhao, S. Lu, S. Dou and H. Wang, “Optimal design of permanent magnet linear synchronous motors based on Taguchi method,” in *IET Electric Power Applications*, vol. 11, no. 1, pp. 41-48, 1 2017.
- [138] S.-Y. Lee, J.-H. Seo, S.-Y. Kwak, C.-G. Lee, S.-Y. Jung, and H.-K. Jung, “Optimal design of outer rotor permanent magnet machine using improved particle swarm optimisation,” in *Proceedings of the 11th International Conference on Electrical Machines and Systems Volume 6*, 2008.
- [139] C. A. C. Coello, G. T. Pulido, and M. S. Lechuga, “Handling multiple objectives with particle swarm optimisation,” *Evolutionary Computation, IEEE Transactions on*, vol. 8, pp. 256-279, 2004.
- [140] J. Kennedy, “Particle swarm optimisation,” in *Encyclopedia of Machine Learning*, ed: Springer, 2010, pp. 760-766.
- [141] J. H. Holland, “Adaptation in Natural and Artificial Systems,” MIT Press, 1975
- [142] L. Davis, “Genetic algorithms and Simulated Annealing” Pitman, 1987
- [143] J.J.Grefenstette, “Optimisation of control parameters for genetic algorithms”, *IEEE Transactions SMC*, vol. 16, pp. 122-128, 1986.
- [144] C. Lai, G. Feng, K. L. V. Iyer, K. Mukherjee and N. C. Kar, “Genetic Algorithm-Based Current Optimisation for Torque Ripple Reduction of Interior PMSMs,” in *IEEE Transactions on Industry Applications*, vol. 53, no. 5, pp. 4493-4503, Sept.-Oct. 2017.
- [145] J. Chen, S. Wang, W. Wang, Y. Tan, Y. Zheng and Z. Ren, “Genetic-algorithm-based control allocation for multi-surface aircraft,” *2017 36th Chinese Control Conference (CCC)*, Dalian, China, 2017, pp. 7333-7338.
- [146] L. Pengfei, W. Guangsen, Z. Xiangming and M. Mingzhong, “Optimal design of a high-power friction brake based on improved genetic algorithm,” *2017 36th Chinese Control Conference (CCC)*, Dalian, China, 2017, pp. 2105-2110.

# Appendices

Table. 23 Test equipment

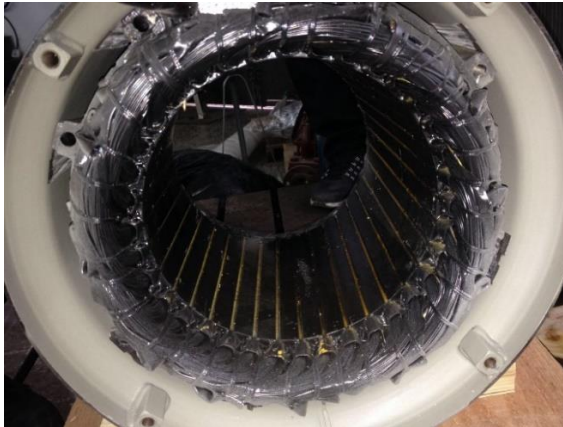
Equipment	Items	PICs
Multi-meters	0.2% accuracy for voltage and current measurement	
Instrument transformer	Instrument transformers have an accuracy according to Standard IEC 60044-1 such that the errors of the instrument transformers are not greater than 0.5% for general testing.	
Torque measurement	The instrumentation used to measure the torque have an accuracy of $\pm 0.2\%$ of full scale	
Speed and frequency measurement	Accuracy is less than 1 rev/min	Included in torque transducer

Temperature measurement	1°C	
Oscilloscope	/	
Prime mover	DC machine with speed control	
Resistive load bank	Adjustable resistive load bank controlled by switches	

Inductive load	Adjustable inductance by changing air-gap distance inside the load	
Three-phase power analyser	For power measurement as well as harmonic analysis	
Symmetrical rotor for test	Two rotors are constructed of the same material by the same manufacturer. Both are designed based on a commercial Cummins PI-144F machine. Two	
Asymmetrical rotor for test	rotors are placed in the original stator for the test.	



a



b



Fig. 97. Photographs of the Cummins PI-144F.

Table. 24 No-load test results

## (a) Symmetrical rotor (high-low)

Line voltage (V)	261	239.1	218.2	196.1	152.6	96.8	50.1	0.68
Excitation current (A)	26.82	17.9	12.55	9.42	6.48	3.9	1.96	0
Excitation voltage (V)	24.9	17.39	12.56	9.67	6.93	4.52	2.49	0
Speed (rpm)	1498	1490	1499	1485	1500	1495	1502	1500
Torque reading (Hz)	10.24	10.16	10.16	10.14	10.09	10.09	10.04	10.04

## (b) Symmetrical rotor (low-high)

Line voltage (V)	50	101	160	186	220	239	257	
Excitation current (A)	1.89	4.12	6.78	8.82	11.11	17.20	28.23	
Excitation voltage (V)	4.54	7.71	10.55	12.27	14.80	22.20	38.6	
Speed (rpm)	1470	1472	1471	1471	1550	1550	1500	
Torque reading	10.11	10.50	10.05	10.06	10.07	10.10	10.10	

## (c) Asymmetrical rotor (high-low)

Line voltage (V)	246.4	218.4	196.5	167	140.9	101.2	46.2	0.52
Excitation current (A)	18.3	12.96	10.73	8.63	7.18	5.05	2.28	0
Excitation voltage (V)	17.05	12.7	10.75	8.86	7.58	5.63	3.06	0
Speed (rpm)	1500	1495	1497	1499	1497	1502	1506	1510
Torque reading (Hz)	10.22	10.32	10.31	10.19	10.15	10.11	10.09	10.07

## (d) Asymmetrical rotor (low-high)

Line voltage	124.5	142.8	166.5	184.4	200.4	220.2	240.3	246.0
Excitation current	6.2	7.18	8.55	9.66	10.85	13	16.08	17.50
Excitation voltage	6.72	7.52	8.74	9.75	10.81	12.69	15.61	16.8
Speed (rpm)	1506	1504	1508	1504	1504	1502	1510	1508
Torque reading (Hz)	10.21	10.21	10.21	10.22	10.27	10.32	10.31	10.32

Table. 25 List of symbols

Item	Expression
S	Apparent power
$V_{ph}$	Rated phase voltage
$I_{ph}$	Rated phase current
$N_{ph}$	Number of turns per phase
$\Phi$	Main Flux
$K_w$	Winding factor
$B_{av}/B_p$	Average air-gap/pole flux density
D	The outer diameter of the rotor
L	The axial length of the rotor
p	Pole number
$\tau$	Pole pitch
$w_p$	Width of pole
$A_p$	The surface area of the pole
$L_p/l_{core}$	Length of stator pole/stator core
$A_f$	Excitation MMF
$K_{teeth}/K_{core}$	The empirical coefficient of iron loss in rotor teeth/stator core
$\alpha_p$	Pole-arc ratio
$p_{bm}$	Rotor iron loss coefficient
$R_a(x)$	Stator copper resistance based on insulation level
$R_{f(x)}$	Rotor copper resistance based on insulation level
v	The rated line speed of the machine